Full-Scale CFD Analysis and Growth Dynamics Modelling of Soft Biofouling Effects on Ship Resistance

MSc Thesis Report

Davide Centorrino

TU Delft

MARIN

(This page is intentionally left blank)

Thesis for the degree of MSc in Marine Technology in the specialization of Ship Hydromechanics

Full-Scale CFD Analysis and Growth Dynamics Modelling of Soft Biofouling Effects on Ship Resistance

MSc Thesis Report

By

Davide Centorrino

Performed at

Maritime Research Institute Netherlands (MARIN)

This thesis (MT.24/45.006.M) is classified as confidential in accordance with the general conditions for projects performed by the TUDelft.

October 2, 2024

Company supervisor:	
Responsible supervisor:	Prof. dr. ir. T. van Terwisga
Daily supervisors:	Ir. H.J. Kamphof, Ir. M. Kerkvliet
Thesis exam committee:	Prof. dr. ir. T. van Terwisga
Chair/Responsible Professor:	Dr. A. Coraddu
Staff Member:	Dr. D. Fiscaletti
Staff Member:	Dr. A. Laskari
Staff Member:	Ir. H.J. Kamphof
Company Member:	
Author Details:	Davide Centorrino
Studynumber:	5851629

TU Delft Delft University of Technology

MARIN

Preface

This project constitutes my final work to obtain the Master in Marine Technology at Delft University of Technology. The research was performed in collaboration with Maritime Research Institute Netherlands (MARIN), under the supervision of Tom van Terwsiga (TU Delft), Harm Jan Kamphof (MARIN) and Maarten Kerkvliet (MARIN).

My interest in biofouling stems from the passion of improving the hydrodynamic performance of ships, which I discovered during my bachelor's studies at Università di Genova. While studying naval architecture, I became particularly fascinated by how various factors can affect a ship's efficiency. The possibility of researching a topic that could help reducing the global emissions, if better understood, seemed really interesting.

I would like to thank Harm Jam Kamphof for the invaluable help, patience and insights he provided throughout my internship. My gratitude extends to Tom van Terwisga for the guidance, and for giving me the chance to carry out my thesis at MARIN, and to Maarten Kervliet who helped me navigating the turbulent waters of CFD. I would also like to acknowledge the help of Bente Schalk-Meijerink and all other MARIN employees for the suggestions and help during the setup of the numerical simulations.

Finally, I am incredibly grateful to my family and friends for the support throughout these six years of my academic career. I want to thank my parents in particular, that supported me in any decision I ever made, and were really excited for my choice to move to The Netherlands to pursue my interests. The "Italians" and all the friends I met in Delft, that made it really easy for me to adjust to the new country and made these two years unforgettable. My friends from Genova, who have been a fundamental part of my life since childhood, and that in part made me who I am today. Thanks also to the MARIN students that managed to distract me through these months of high highs and low lows.

Davide Centorrino
Delft, September 2024

Abstract

The development of biofouling on ship hulls is known to be deeply damaging for the overall performance of the vessel. The real effects of soft fouling, especially due to biofilms and diatoms, are however not yet understood and precisely defined. The current work numerically assesses the influence of an increase in surface roughness due to soft biofouling over the hydrodynamic performance of a containership. The simulations are carried out through MARIN's in-house software ReFRESCO. Unsteady free-surface computations are used to evaluate both the resulting frictional drag, and the wave profile modification for different input surface roughness values. The results show that frictional resistance at 14 knots is increased of up to 45% for a limit equivalent sand-grain roughness height $k_s = 300\ \mu m$, correspondent to biofilms. Residuary resistance at the same speed suffers decreases of maximum 2.5% in the same range. These consist in hull pressure variations in the aft and transom areas of the vessel, and in small height differences in the wave pattern. A dataset obtained from monitoring of the containership for five years is used to study the added frictional resistance evolution due to roughness. Holtrop & Mennen procedure integrated with environmental variables show a maximum increase of $\Delta C_F = 1.4 \cdot 10^{-3}$. The methodology proves useful to identify potential drydocking periods, and to provide an overview of the added resistance trend. It should however be implemented with Machine Learning models to improve accuracy, in case the precise influence needs to be assessed. A novel comprehensive soft fouling growth model is created to assess the surface roughness k_s and ΔC_F time evolution. This constitutes one of the few attempts in the literature to create a model that simultaneously considers the effect of multiple environmental and operational variables based on the GPS position. Light intensity, sea surface temperature, draft and concentration of nutrients. Increases of up to $100\ kN$ in resistance and of $\Delta C_F = 0.001$ are observed if only diatoms are considered are integrated. Temperature and nutrients result to be more relevant for growth, in comparison to light intensity and draft. A sensitivity study is also carried out to prove the small dependence on the choice of the analytical approach. A comparison of the growth model + CFD results with data processing show that the analytical procedure provides a good indication on the growth trend, while added resistance intensity is underestimated in the order of $\Delta C_F = 4.65 \cdot 10^{-4}$.

Contents

List of Figures

List of Tables

Nomenclature

Abbreviations

Abbreviation	Definition
AC	Acoustic Correlation
CFD	Computational Fluid Dynamics
CFL	Courant-Friedrichs-Lewy
CFU	Colony Forming Unit
DNS	Direct Numerical Simulation
DoF	Degree of Freedom
ECA	Emission Control Area
GHG	Greenhouse Gas
GPS	Global Positioning System
IMO	International Maritime Organization
IQR	Interquartile Range
ITTC	International Towing Tank Convention
KCLCC2	Keel Laid Cargo Carrying Capacity (2nd generation)
KCS	Kriso Container Ship
LES	Large Eddy Simulation
MARPOL	Maritime Pollution
MGO	Marine Gas Oil
RANS	Reynolds-Averaged Navier-Stokes
ReFRESCO	Reliable & Fast Rans Equations Ship Construction Offshore
SPC	Self-Polishing Copolymer
TBT	Tributyltin
URANS	Unsteady Reynolds-Averaged Navier-Stokes

Symbols

Symbol	Definition	Unit
a	Maximum rating (regression upper limit)	-
A	Empirical Grigson constant	-
A_i	Area covered by fouling category	m^2
AHR	Average Hull Roughness	μm
B	Breadth	m
B_i	Smooth log-law intercept	-
c_l	Light intensity superposition constant	-
c_n	Phosphorous superposition constant	-
c_t	Temperature superposition constant	-
C	Surface colour	-
C_A	Correlation allowance	-
C_{AA}	Air resistance	-
C_B	Block coefficient	-
C_{bulb}	Bulb resistance coefficient	-
C_c	Container capacity	TEU
$C_{current}$	Current resistance coefficient	-
C_f	Skin friction coefficient	-
$C_{f,ratio}$	Skin friction ratio	-
$C_{f,ref}$	Flat plate reference skin friction	-
C_p	Dynamic pressure coefficient	-
C_F	Frictional resistance coefficient	-
C_R	Residuary resistance coefficient	-
C_T	Total resistance coefficient	-
$C_{transom}$	Transom resistance coefficient	-
C_{VP}	Viscous pressure resistance coefficient	-
C_W	Wave-making resistance coefficient	-
C_{waves}	Waves resistance coefficient	-
C_{wind}	Wind resistance coefficient	-
D	Propeller diameter	m
D_l	Daylength	h
DWT	Deadweight	t
D_t, D_w	Non-dimensional propeller diameter coefficients	-
e_a^{21}, e_{ext}^{21}	Relative mesh errors	-
F_{waves}	Wave force	kN
Fr	Froude number	-
FR	Fouling Rating	-
g	Gravitational acceleration	m/s^2
GCI	Grid Convergence Index	-
H	Hour angle	$^\circ$
H_c	Ship heading	$^\circ$
H_{waves}	Wave height	m
I	Light intensity	lux
I_{day}	Day light intensity	lux
I_{diffr}	Diffracted light intensity	lux
I_{night}	Night light intensity	lux
I_{opt}	Optimum light intensity	lux
I_0	Light intensity entering water perpendicularly	lux
J	Advance ratio	-
J_d	Day o the year	-
k	Form factor	-
k_{att}	Attenuation rate	-

Symbol	Definition	Unit
$k_{coating}$	Coating roughness	μm
k_s	Equivalent sand-grain roughness height	μm
k^+	Roughness Reynolds number	-
K	Kurtosis	-
K_S	Substrate saturation model constant	$\mu g/L$
K_i	Substrate inhibition model constant	$\mu g/L$
L	Ship length	m
LCB	Longitudinal coordinate of the center of buoyancy	m
L_{oa}	Length overall	m
L_{pp}	Length between perpendiculars	m
L_{wl}	Waterline length	m
$L°$	Latitude	$^\circ$
n	shaft rotational speed	rps
N	Dataset size	-
$NSTM$	Naval ship's technical manual	-
N_{total}	Filtered daily speed measurements	-
$N_{V<1kn}$	Measurements with speed lower than 1 knot	-
p	Daylength coefficient	-
p_a	Order of convergence	-
p_{wind}	Wind pressure	Pa
P	Phosphorous concentration	μM
P_B	Brake power	kW
P_d	Dynamic pressure	Pa
P_E	Effective power	kW
P_{hs}	Hydrostatic pressure	Pa
psu	Salinity	g/kg
q	Corrected order of accuracy	-
Q	Shaft torque	kNm
r^p	Error reduction factor	-
Re	Reynolds number	-
Re_x	Longitudinal coordinate Reynolds number	-
R_F	Frictional force	kN
R_{press}	Pressure force	kN
R_T	Total ship resistance	kN
R_{t50}	Peak-to-trough measure along 50 mm of surface	μm
r_{21}, r_{32}	Grid refinement ratio	-
S	Wetted hull surface	m^2
S_n	Nutrient concentration	$\mu g/L$
SC	Surface Coverage	%
SFC	Specific Fuel Consumption	g/kWh
Sk	Skewness	-
SST	Mean Sea Water Surface Temperature	$°C$
t	Time	s
t_0	Time for rating to reach maximum point	s
T	Draft	m
T_{aft}	Aft draft	m
T_{fore}	Fore draft	m
T_{opt}	Optimum temperature	$°C$
T_{max}	Maximum temperature	$°C$
T_{min}	Minimum temperature	$°C$
T_{waves}	Wave period	s
u	Axial velocity	m/s
U^+	Non-dimensional boundary layer velocity	-
U_τ	Friction velocity	m/s

Symbol	Definition	Unit
U_0	Free-stream velocity	m/s
V	Ship speed	m/s
V_{wind}	Wind speed	m/s
w	wake fraction	-
y	Distance from the wall	m
y^+	Non-dimensional distance from the wall	-
z	Depth	m
α	Roughness correlation constant	-
β	Diffraction angle	$\circ$
δ	Thickness of the boundary layer	m
δt	Timestep	s
Δ	Differential operator	-
ΔC_F	Added frictional resistance coefficient	-
Δm	Added fuel mass	t
ΔR_F	Added frictional resistance	kN
ΔU^+	Roughness function	-
η_c	Antifouling coating performance parameter	-
η_G	Gear efficiency	-
η_H	Hull efficiency	-
η_O	Open water efficiency	-
η_R	Relative rotative efficiency	-
η_S	Shaft efficiency	-
η_{tot}	Total efficiency	-
θ	Sun revolution angle	$\circ$
θ_{ship}	Ship course	$\circ$
θ_{wind}	Wind angle	$\circ$
θ_z	Solar zenith angle	$\circ$
κ	Von Karman coefficient	-
λ	Light wavelength	Å
μ	Growth rate	$1/day$
μ_{nutr}	Growth rate due to phosphorous concentration	$1/day$
μ_{light}	Growth rate due to light intensity	$1/day$
μ_{temp}	Growth rate due to sea surface temperature	$1/day$
μ_{max}	Maximum specific growth rate	$1/day$
μ_w	Water dynamic viscosity	kg/ms
μ_{m1}	Maximum growth rate	-
μ_{m2}	Inhibited growth rate	-
μ_{m3}	No-phosphorous growth rate	-
ν	Seawater kinematic viscosity	m^2/s
ν_a	Air kinematic viscosity	m^2/s
ρ	Seawater density	kg/m^3
ρ_a	Air density	kg/m^3
ρ_a	Air density	kg/m^3
σ	Surface energy	mN/m
τ	Half-width of the bell curve	s
τ_w	Wall shear stress	MPa
ϕ	Sun declination angle	$\circ$
ϕ_{ext}	Extrapolated value	varying
ϕ_i	Simulation result for i-th mesh	varying
Φ	Cumulative density function	-
∇	Wetted ship volume	m^3
ω	Specific dissipation rate	$1/s$

1 Introduction

Maritime transport represents a vital component of society, serving as one of the main ways of displacing both goods and people. Currently, around 90% of all commodities in the world are delivered to their destination by ship. This shows the relevance of optimizing the transportation process in terms of finding the best route to enhance profit, reduce emissions, and improve energy efficiency.

One of the main elements that hinders an optimal ship performance is biofouling. This term refers to the attachment and growth of acquatic species such as diatoms, algae and hard foulers (i.e. barnacles) on marine structures, especially ship hulls. The physical consequence of fouling is a higher hull surface roughness. This has a detrimental effect on the resistance profile of the ship through a modification of the boundary layer. The needed power and greenhouse gas emissions are increased as a result. The amount of variables influencing the growth of acquatic organisms is however challenging to define with certainty. As a result, there is no unified and clear approach in the literature to address the issue. The relevance of a deeper understanding of the rate at which soft foulers grow, and their effect on hull efficiency, may be motivated considering the rise in importance of the environmental standpoint. This has produced a worldwide array of regulations, given in the maritime field by the Maritime Pollution (MARPOL) Convention, issued by the International Maritime Organization (IMO). International shipping still accounts for approximately 3% of the world's greenhouse emissions [1]. That is despite being the least environmentally damaging mode of transport, if considering the value of carried goods.

Another issue connected to biofouling on ships is the transport of species endemic to one area of the world to another, possibly generating environmental unbalances. Such phenomenon may be downsized by implementing a suitable antifouling strategy for the areas where the ship will navigate. This partially aligns with the objectives set by the Ballast Water Management Convention issued by IMO [2]. Cleaning of the hull, at drydock or during loading/unloading operations, is also good practice to ensure a higher performance of the ship.

1.1. Goal & Scope

The aim of the research develops from the current state-of-the-art knowledge gaps regarding soft biofouling growth modelling, and surface roughness influence on resistance evaluated through numerical simulations. A few growth models able to consider a single environmental variable at the time have been created, but they focus especially on hard fouling. The project aims at developing a physics-based growth model for soft fouling accounting for the influence of multiple environmental factors. The resultant roughness is then used as input for a full-scale CFD analysis, where its influence on residuary and frictional resistance can be evaluated. The effective time evolution of the added frictional resistance is also investigated and associated with a roughness value. This allows to understand what is the influence of the operational variables on a real ship.

Some limitations were imposed on the scope of the project to allow its feasibility in the available timeline. This is particularly the case for the analytical growth model. Since there is no comprehensive method in the literature, a simplified approach that uses a linear superposition of the environmental variables is chosen. The biofilm is considered to be generated only by diatoms, and the combined growth of soft and hard fouling is not included. Furthermore, the non-geometric characteristics of the biofilm (porosity and flexibility) are not accounted for. As far as data processing is concerned, the provided dataset is incomplete for some signals over certain periods of time. The missing values are thus assumed accordingly. Lastly, the main assumption of the CFD simulations is considering the hull as completely covered by a biofilm of same roughness.

1.2. Relevance

The research has several associated implications. These can be subdivided into the engineering, scientific and societal perspectives. From an engineering point of view, the outputs are meant to provide a new framework that can be used to schedule drydocking periods, and give insights on the development of more effective antifouling strategies. As far as the scientific standpoint is concerned, the development of a new predictive analytical growth model stem from the results. A better understanding of which environmental variables should be taken into account in such approach can also be achieved. The interdisciplinary nature can also foster collaboration between different sciences. Finally, this project aims at developing a better understanding of biofouling growth and its influence on ship efficiency. This ultimately leads to a reduction of the overall CO_2 and greenhouse gas emissions, providing a relevant tool against global warming. The saved fuel costs would also imply a lowering of the global shipping costs, and consequently of the goods and services as well.

1.3. Research question & Structure of the report

The main research question that will be answered in the report is:

Can ship added resistance due to biofouling be predicted using growth modeling and CFD simulations? And how can it be validated?

This leads to the more detailed sub-research questions:

1. What is the added resistance increase rate throughout the operative life of a ship, given the relevant data?
2. Which are the environmental variables that influence biofouling and slime layers growth the most, and how is it possible to predict it?
3. Does ship speed have any influence over both growth and detachment of foulants?
4. To which degree is residuary resistance influenced by surface roughness?

To answer these questions, several steps are taken. First, a general overview addressing biofouling biology and effect on ships, as well as roughness fluid dynamics, will be covered in Section 2.1. State-of-the-art methodologies for the evaluation of biofouling modelling, and consequences on the shipping industry will then be presented in Section 2.2. This includes the most relevant analytical growth models from literature, and Computational Fluid Dynamics (CFD) techniques (Section 2.2.2). Chapter 3 provides a description of the dataset used throughout the project (Section 3.1), and of the procedures followed for the development of both the added frictional resistance trend (Section 3.2) and of the growth model in Section 3.3. A description of the geometry, boundary conditions and simulations setup is given for flat plate (Section 3.4.1) and full-scale containership (Section 3.4.2). The verification approaches are described in Chapter 4, while Chapter 5 contains the results for resistance trend, growth model and CFD simulations. Section 5.4 contains the combined results of the three parts, and Chapter 6 the discussion. Finally, the conclusions are drawn in Chapter 7, and recommendations for future work are reported in Chapter 8.

2

Literature Review

2.1. General Overview

2.1.1. Problem definition

Biofouling is the accumulation of micro and macro organisms on immersed surfaces, which leads to economic, environmental and safety-related negative effects [3]. More than 4000 marine biofouling species have been identified in the world, most of which live mainly along the coast or in harbours. Here the concentration of nutrients is higher, and their growth is thus facilitated [4]. Examples of species that may gather on a ship hull are illustrated in Figure 2.1.

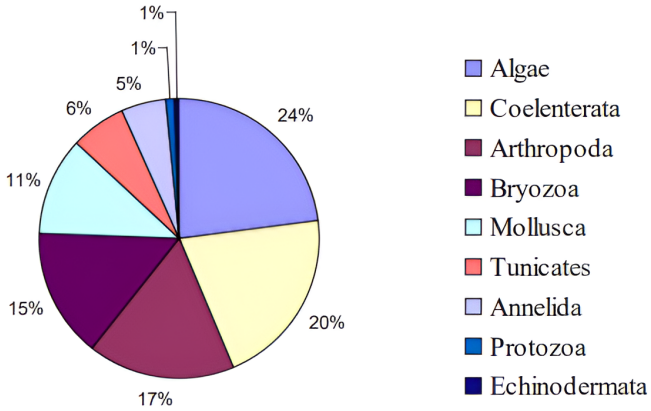

Figure 2.1: Total species on ships [5]

Ship foulers can be classified in two main categories: microfouling and macrofouling. To the former belong organisms such as bacteria, diatoms and protozoa, responsible for the creation of slime layers. Despite the small dimensions, their accumulation in clusters have a profound influence on frictional resistance: within minutes from immersing an object in water, a conditioning biofilm develops, attaching irreversibly and forming a multiple species layer [6]. This causes additional surface roughness and turbulence, which increases frictional resistance and thus fuel consumption [7]. Macrofouling includes soft foulers (algae, coelenterata, tunicates) and hard foulers (barnacles, bryozoans, bryozoans, annelida, mollusca, echinodermata). For these, the hull efficiency penalty is generally higher because of the greater roughness resulting from their settlement. Furthermore, the establishment of macro-foulants may be influenced by the already formed biofilm. It was shown that the diatoms concentration on the hull may either induce maturation of barnacle larvae, or repel it because of competition for nutrients and light [8]. The presence of some species in comparison to others, and the general composition of the biofouling layer, are heavily influenced by the seasonality.

Attachment mechanism

The organisms responsible of hull fouling generally prefer to attach to a surface instead of free-floating for a number of reasons [9]. For example, the submerged moving object may supply additional nutrients for the organisms to grow. This is thanks to a continuous fresh flow of water, or fouled substances already present in the troughs of the inherent roughness of the surface [9]. Aeration and waste removal by the flow provide ideal conditions for biofouling growth as well [8].

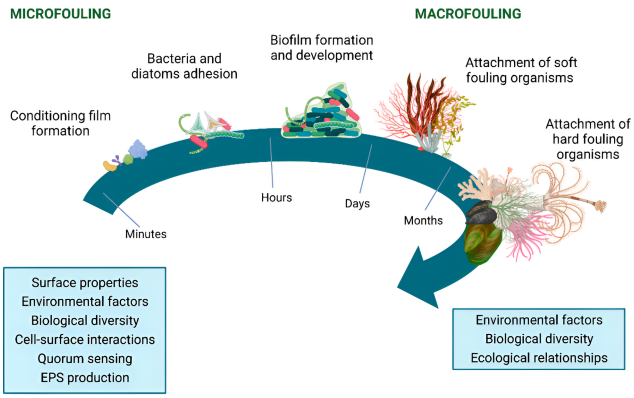

Figure 2.2: Marine fouling process [10]

In the publications by Melo et al. [9] and Abarzua et al. [11], a step-by-step explanation of how the biofilm links to the surface is provided, also reported visually in Figure 2.2. After an initial transfer of macromolecules to the surface and the formation of an adsorbed layer in the first minutes, organisms adhere in clusters to the surface [8, 11]. The time delay between the nutrients layer formation and the accumulation of organisms composes the ”Conditioning” phase. The bond between surface and organisms is at this stage not strong yet, which means that the cells may detach. Then, nutrients flowing through the biofilm encourage the production of new cells, increasing the thickness and the extension of the foulants (Development phase). This growth is not perennial: the biofilm thickness stabilizes about a mean value because of removal forces of the fluid shear [9] (Figure 2.3). This ideal trend is however influenced by multiple factors. Namely, experiments conducted on fouled rotating cylinders demonstrated that colonies exposed to spin had lower growth rate and a greater reduction in size [12].

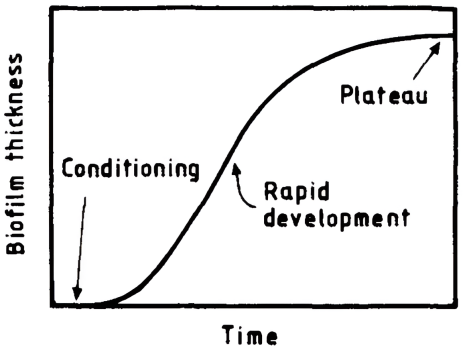

Figure 2.3: Biofilm thickness development curve [9]

Antifouling techniques

Antifouling technologies provide a front line defense against biofouling. These include both hull cleaning procedures and the application of dedicated coatings. The former, consisting in mechanical cleansing, are outside the scope of the project and will not be investigated. Antifouling coatings are employed to reduce the arise of slime layers and attachment of other types of organisms. The wide array of shipping paths implies that antifouling performance should be tested for multiple organisms. A strategy that could work against organisms living in temperate waters may be ineffective in tropical areas, and vice-versa [6]. Coatings can be mainly classified in biocidal and non-biocidal [13]. To the first category belong Tributyltin Self-Polishing Copolymers (TBT-SPC). These were able to limit fouling on ships for 5 years through a steady release of TBT, able to form a water soluble product [14]. Since 2008 IMO has completely banned their application because of unacceptable environmental impact, as a result of

the *International Convention on the Control of Harmful Anti-fouling Systems on Ships* [15].

Currently, one of the biocidal coating options which has proven to be equivalent in terms of performance to TBT, is Tin free SPC [14]. This generates a continuous release of silyl or zinc compounds when the ship is stationary and most likely to foul [14]. They have a good initial hydrodynamic performance thanks to the smooth surface, and are preferred for vessels with longer drydock intervals [13]. Performance wise, the best non-biocidal paints are Foul-Release coatings. These act as a physical defense against fouling, preventing the attachment of organisms thanks to their surface properties [13]. They show optimal performance at speeds higher than 12 knots, as they rely on the shear force that develops on the hull, causing fouling detachment [13].

Effect on ships

The significance of optimizing ship efficiency stems from the role shipping has in the global market. Ensuring an energy effective vessel provides benefits not only economically, but also an environmentally friendly strategy. As it is shown in Figure 2.4, there are many factors depleting the optimal exploitation of the natural resources used to generate power. Biofouling of both hull and propeller(s) constitute only a portion of all the elements that can be studied to improve the overall performance. Nonetheless, their relevance is highlighted in the literature by a general effort of the authors to achieve a deeper understanding of the phenomena.

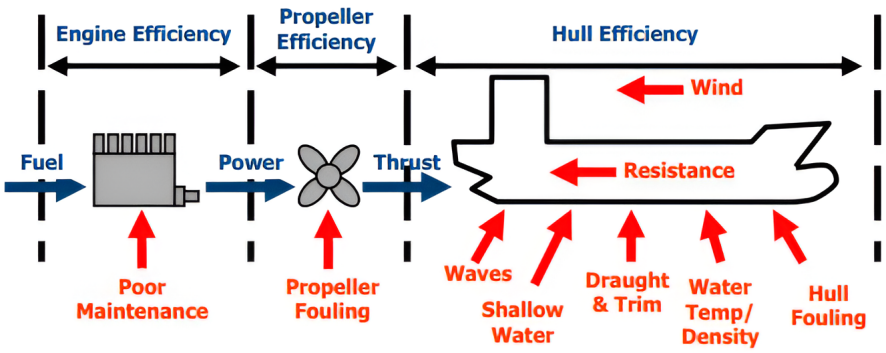

Figure 2.4: Variables influencing propulsion performance [16]

One of the main repercussions of hull and propeller fouling is indeed an increase in fuel consumption. Multiple other factors affected by biofouling have financial and operational implications. Specifically:

- Antifouling paints need to be applied periodically to guarantee a continuous protection [6];
- Drydocking must be carried out multiple times throughout the operational life of the ship for hull cleaning;
- Increased required engine power for a certain speed causes the engines to run at higher loads, thus enhancing their wear and requiring more maintenance.

Figure 2.5 shows the costs time evolution for a US Navy ship as a consequence of biofouling, with different coatings and fouling ratings FR (Table 2.1, from Schultz [17]). It is evident how a highly fouled hull entails greater capital expenses in comparison to smoother surfaces, mainly due to fuel consumption. This leads for the mentioned ship to a final $\$43.8M$ over a period of 15 years [17], equivalent to around $\$2.3M$ per year. The trend related to Case 2 (ablative coating, no fouling) also highlights the inherent roughness of the paint that causes a 1.4% fuel consumption and $\$3.33M$ costs increment [17]. A similar situation is visualized in Figure 2.6, where the annual costs per ship are plotted against the increasing fouling ratings.

Table 2.1: Hull roughness and fouling scenarios for the Arleigh Burke class-destroyer [17]

Scenario	Coating description	Fouling level	Interim cleaning frequency (year$^{-}1$)	Full cleaning frequency (year$^{-}1$)
Case 1	Hypothetical hydraulically-smooth ablative copper AF	FR-0	0	0
Case 2	Ablative copper AF, as typically applied ($Rt_{50} = 150\mu m$)	FR-0	0	0
Case 3	Ablative copper AF, as typically applied ($Rt_{50} = 150\mu m$)	FR-30	2.4	0.21
Case 4	Ablative copper AF, as typically applied ($Rt_{50} = 150\mu m$)	FR-60	2.4	0.21

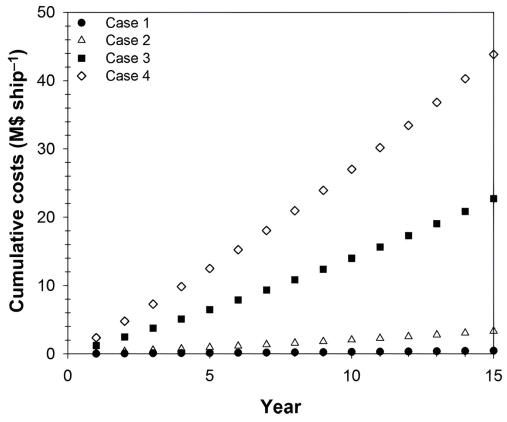

Figure 2.5: Cumulative costs for ships of coating and fouling level from Table 2.1 [17]

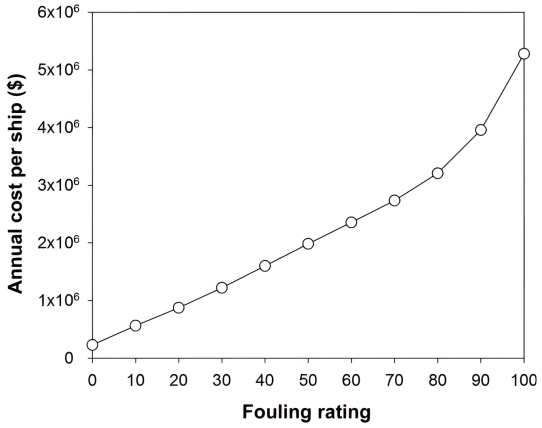

Figure 2.6: Annual costs per ship for a range of hull fouling levels (FR) [17]

As already mentioned, another consequence of biofouling is increased emissions (Figure 2.7). Minimizing the production of greenhouse gases, such as sulphur oxide (SO_x) and nitrogen oxide (NO_x), is crucial for the world and the maritime industry alike. A study carried out by IMO has in fact pointed out that around 2.6% of global emissions are produced by the maritime industry. Of these, $9 \div 12$% are due to propeller and hull conditions deterioration [18]. This means that, even if to relatively little extent, a discharge reduction of SO_x and NO_x can help satisfy the goals set by the Paris Agreement in 2016. This treaty set out a global framework to avoid dangerous climate change by limiting the global average temperature rise below $2°C$, while pursuing to limit it to $1.5°C$ [19].

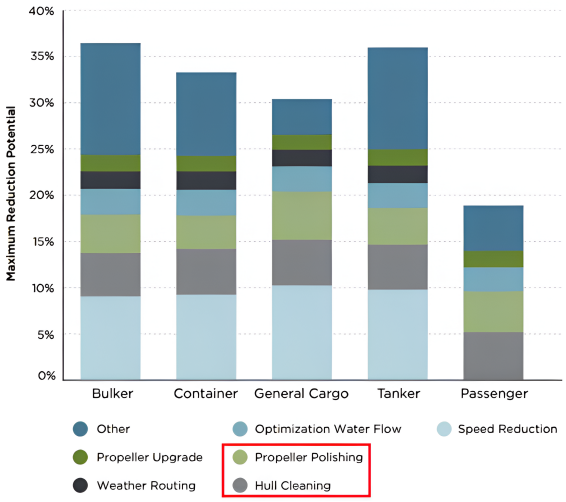

Figure 2.7: CO_2 reductions of technical and operational measures by ship types [20]

Each ship with flag of an IMO State member, or that operates within its jurisdiction, is required to respect MARPOL regulations [21]. Its Annex VI sets limits on greenhouse gas and ozone depleting substances emissions [22]. The relevance for biofouling is given by the Emission Control Areas (ECA), locations of the world where the airborne emissions are under stricter control and should be minimized. This implies not only using greener fuel alternatives such as Liquified Natural Gas or installing scrubbers, but also improving the overall efficiency of the vessel.

2.1.2. Scientific investigation

Roughness fluid dynamics

Any surface moving through water with a certain speed creates a boundary layer in its immediate vicinity. This consists in a thin layer where the average speed of the water increases from zero at the wall, to its full free-stream value [23], thus creating a velocity gradient. This phenomenon is due to the fluid adhering to the wall (no-slip condition), while the frictional forces delay its motion in the layer [23]. The resulting shear stress τ_w is caused by water viscosity and defined by Newton's law:

$$\tau_w(y) = \mu_w \frac{\partial u}{\partial y} \tag{2.1}$$

where μ_w is water dynamic viscosity, u is the axial velocity component and y is the distance from the wall. The boundary layer extends up to the distance from the wall, defined by δ, in which the axial velocity reaches a value of 0.99 times the free-stream velocity U_0 [24]. The thickness of a turbulent boundary layer for a smooth flat plate can be calculated with the formulation proposed by Schlichting [25]:

$$\delta(x) = 0.37 x Re_x^{-0.2} \tag{2.2}$$

Re_x is the Reynolds number associated to the longitudinal coordinate x, reported in Equation 2.3 together with its standard formulation. This variable determines the different types of flow occurring throughout the surface. In particular, at the leading edge the flow is laminar, characterized by no turbulent stresses and modest shear because of small gradients in the axial velocity [24]. Further away from the leading edge, instabilities begin to appear, creating three-dimensional vortices and turbulent spots in the so-called transition region. Finally, the turbulent region is distinguished by a fully developed turbulent layer. The steep gradients of streamwise velocity and the added turbulent stresses result here in a frictional resistance increase, if compared to the laminar flow [24]. Figure 2.8 shows the development of a turbulent boundary layer on a flat surface, as well as the most significant characteristics above explained.

$$Re = \frac{UL}{\nu} \qquad Re_x = \frac{Ux}{\nu} \tag{2.3}$$

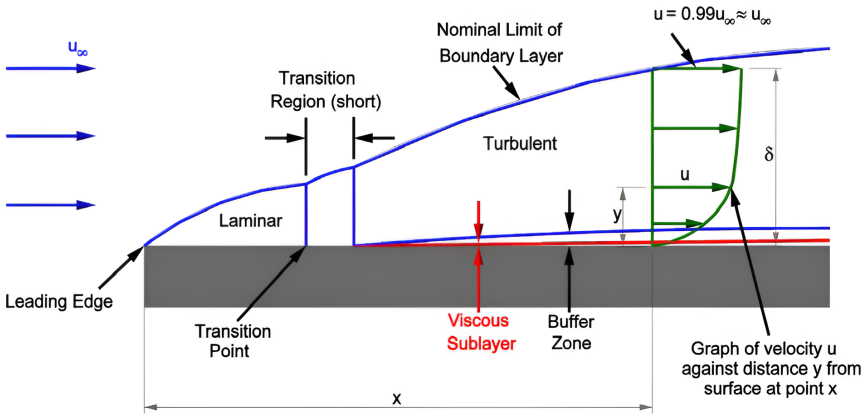

Figure 2.8: Development of turbulent boundary layer over a flat surface[1] [26]

[1] The free-stream velocity is here indicated as u_∞ instead of U_0

Surface roughness effect on boundary layer

In fluid mechanics, surface roughness is judged not by the microns, but instead by the flow occurring next to it [27]. A surface subjected to turbulent flow cannot be considered smooth if its topographical features are large enough to disrupt the eddies near the wall. This causes an alteration of the momentum, heat and mass transfer. The main consequence of increased surface roughness consists in a boundary layer modification: Clauser [28] demonstrated that roughness produces a downward shift of the velocity profile in the log-law region U^+. The generalized velocity profile is then:

$$U^+ = \frac{1}{\kappa}\, logy^+ + B_i - \Delta U^+ \qquad y^+ = \frac{yU_\tau}{\nu} \tag{2.4}$$

y^+ represents the non-dimensional normal distance from the wall, κ the Von Karman coefficient, and B_i the smooth log-wall intercept. It can be noticed that Equation 2.4 is valid for smooth surfaces as well, since in such case $\Delta U^+ = 0$. The roughness function is dependent on the roughness Reynolds number k^+ (Equation 2.5), function of viscosity ν, roughness height (equivalent sand-grain roughness height k_s), and friction velocity U_τ. The latter is defined by Candries et al. [29] through Equation 2.6, as a function of wall shear stress τ_w and water density ρ.

$$k^+ = \frac{k_s U_\tau}{\nu} \tag{2.5}$$

$$U_\tau = \sqrt{\frac{\tau_w}{\rho}} \tag{2.6}$$

The roughness Reynolds number k^+ defines the separation between the flow regimes previously introduced. For example, Nikuradse criterion establishes that $k^+ < 5$ corresponds to smooth regime, $5 < k^+ < 70$ to transitional and $k^+ > 70$ to completely rough flow. The predictive models are based on the assumption that smooth and rough wall turbulence behaves similarly away from the wall [27]. This implies that friction-scaled turbulent relative motions in the outer layer ($\delta \geq y$) are independent of surface condition at sufficiently high Reynolds number.

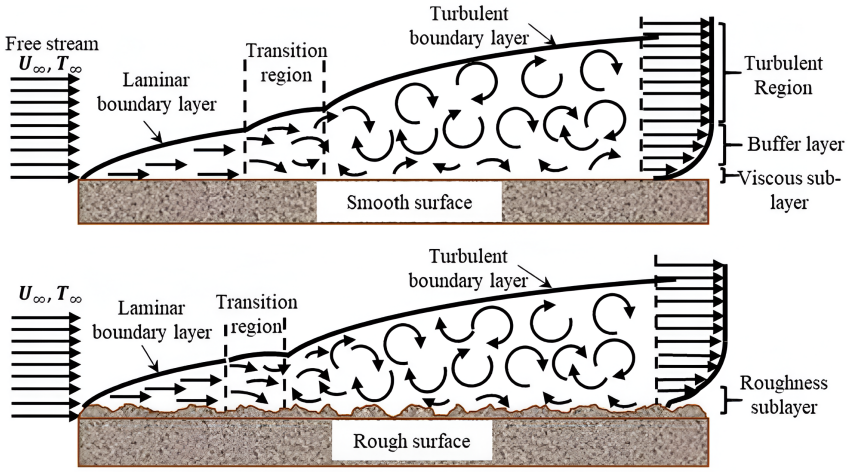

Figure 2.9: Boundary layer comparison over a smooth (top) and rough (bottom) surface [2][30]

Figure 2.9 shows how surface roughness modifies the boundary layer for a smooth and rough flat plates of same dimensions. Specifically, the rough surface generates more turbulence. This causes a reduction in the distance from the leading edge where the transition region is reached, also implying an earlier fully tubulent boundary layer.

[2]The free-stream velocity is here indicated as U_∞ instead of U_0

Roughness characterisation

Few variables able to describe the status of the hull surface have been developed throughout the years. Table 2.2 shows fouling characterisation variables, while Figure 2.10 provides a representation of how water surrounding a rough wall behaves at microscopic level.

Table 2.2: Typical values of fouling rating, equivalent sand roughness height and peak-to-trough height for various surface conditions, based on Schultz [31]

Surface condition	NSTM	k_s $[\mu m]$	R_{t50} $[\mu m]$	FR
Smooth	0	0	0	0
AF coating applied	0	30	150	0
Deteriorated coating / light slime	10 ÷ 20	100	300	0 ÷ 20
Heavy slime	30	300	600	20
Small calcareous fouling or weed	40 ÷ 60	1000	1000	20 ÷ 70
Medium calcareous fouling	70 ÷ 80	3000	3000	-
Heavy calcareous fouling	90 ÷ 100	10000	10000	-

The equivalent sand-grain roughness height k_s was introduced by Schlichting [25]. It defines the size of uniform, close-packed sand grains on a hypothetical surface that would cause the same drag as that created by the real non-uniform wall roughness. Despite being a length scale, k_s does not measure a physical distance, but instead a hydraulic scale for a specific surface roughness. It can also be used as input parameter for numerical simulations, as it will be discussed in Section 2.2.2. The main problem connected to this modelling parameter is the assumption of considering rigid roughness [27], which is not accurate for light fouling such as slime layers. Other surface characteristics should therefore be considered to obtain a more precise prediction of the behaviour of such kinds of fouling.

R_{t50} represents the distance between maximum peak and lowest trough in any given length of 50 mm along the submerged hull [32]. From Table 2.2 it can be noticed that this variable is equivalent to k_s for calcareous fouling. This is because the local median of R_{t50} is used to obtain the Average Hull Roughness AHR, assumed to be correspondent to k_s in most of the literature [33]. The Naval Ships' Technical Manual NSTM is a rating system developed by the US Navy. It is used by divers to evaluate the fouling condition of the hull [31]. As it does not represent a physical variable, it should not be used inside complete models for surface roughness characterization.

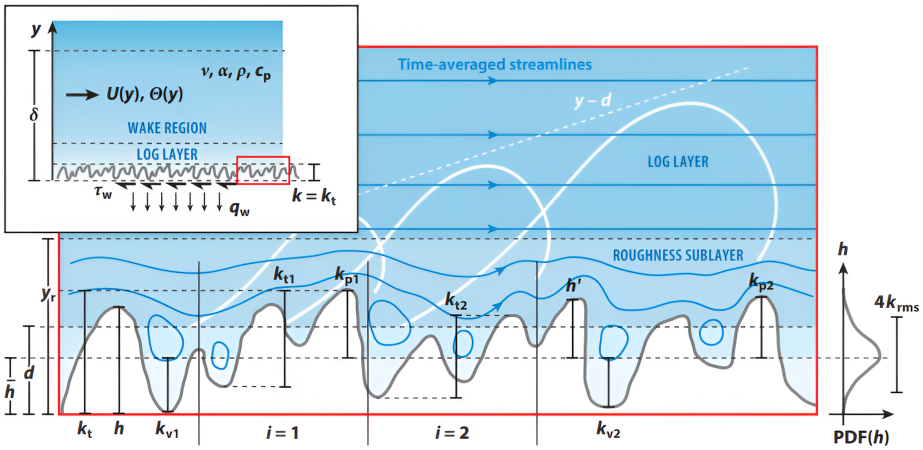

Figure 2.10: The setup of the roughness problem [27]

Resistance evaluation

The modification of the boundary layer due to biofouling creates an increase in total resistance of the ship R_T. This characteristic is usually considered through its non-dimensional variant C_T in Equation 2.7, dependent on wetted surface area S, water density ρ and ship speed V.

$$C_T = \frac{R_T}{\frac{1}{2}\rho S V^2} \tag{2.7}$$

The total resistance coefficient consists of the residuary resistance coefficient C_R, function of Froude number Fr, and of the frictional resistance coefficient C_F,dependent on Reynolds number Re [34].

$$Fr = \frac{V}{\sqrt{gL}} \tag{2.8}$$

The two components can be further divided as reported in Equation 2.9. Here, the residuary resistance is split into viscous pressure resistance C_{VP} and wave-making resistance C_W. The former is dependent on the pressure field that develops around the hull, and can be rewritten as a function of the form factor k, $C_{VP} = kC_F$.

$$C_T = C_R(Fr) + C_F(Re) = C_F + C_{VP} + C_W = (1+k)C_F + C_W \tag{2.9}$$

The total resistance is therefore mainly made up of three components: wave-making C_W, form friction kC_F and skin friction C_F. Figure 2.11 highlights the contribution of each component over a range of Froude numbers (therefore ship speed) towards the total resistance. At low to moderate velocities ($Fr < 0.25$) the skin friction is the largest component, while at higher velocities the form and wave-making drag become dominant [35]. This implies that the increase in frictional resistance due to biofouling growth is of great relevance for slow steaming displacement vessels, while fast boats are generally more influenced by wave-making. Equation 2.9 is meant to represent only the most relevant contributes of the total resistance, and shows only one of many characterisations of C_T. Both the correlation allowance C_A and the air resistance C_{AA} coefficients are neglected. The increase in resistance due to surface roughness is included inside the frictional resistance, and here considered to only influence such component.

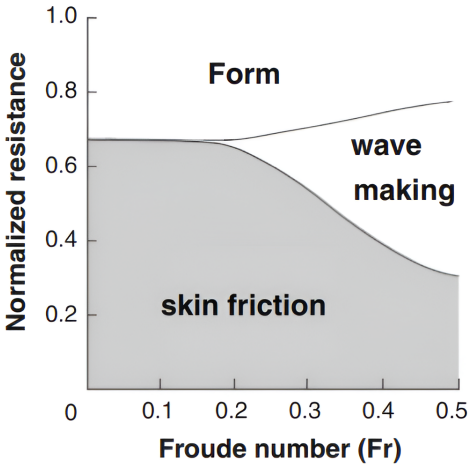

Figure 2.11: Normalized resistance of a ship hull as a function of Froude number [36]

From the available literature, it is evident that the most widely used variable to model surface roughness is k_s. However, the way this is implemented in the total resistance coefficient C_T is not equivalent

for all authors. Namely, Holtrop and Mennen [37] take into account the additional resistance due to biofouling through the correlation allowance C_A as in Equation 2.10, by considering a standard value of $k_s = 150\ \mu m$.

$$C_A = \frac{0.105\sqrt[3]{k_s} - 0.005579}{\sqrt[3]{L}} \tag{2.10}$$

Townsin [33] and Bowden et al. [38] consider k_s as an effective increase in frictional resistance with respect to the smooth hull condition. Their formulation are presented respectively in Equation 2.11 and 2.12. Such variable is originally implemented as an Average Hull Roughness AHR, since no information on the real roughness distribution can be gathered.

$$\Delta C_F = 0.044\ \sqrt[3]{\frac{k_s}{L}} - 10Re^{-1/3} + 0.000125 \tag{2.11}$$

$$\Delta C_F = \left[105\ \sqrt[3]{\frac{k_s}{L_{WL}}} - 0.64\right] \cdot 10^{-3} \tag{2.12}$$

The lack of knowledge on surface roughness modelling is highlighted by the fact that even the most prominent authors (i.e. ITTC) do not propose an analytical equation that takes into account more than a single surface characteristic and ship length.

Experiments carried out by Schultz et al. [39] on flat plates show that fouling causes a C_F increase from 33 to 68%, for a biofilm thickness of $160\ \mu m$ and $350\ \mu m$ respectively. It is however important to highlight that a larger mean roughness does not necessarily imply greater C_F. Results from Candries et al [14] indicate that FR coatings have slightly less frictional resistance than others, despite having a larger mean roughness. Furthermore, results from Swain et al. [40] demonstrate that the choice of one paint over another is capable of generating important differences in the resistance coefficient over time. Foul release coatings (FR-1, FR-2) in Figure 2.12 exhibit the lowest drag coefficients early in the experiment, and the highest in static conditions after 60 days. Their 15 days dynamic performance is however the best thanks to their properties to self-clean. The two copper-based systems (Cu-SPC, Cu-Abl) show better behaviour in static conditions.

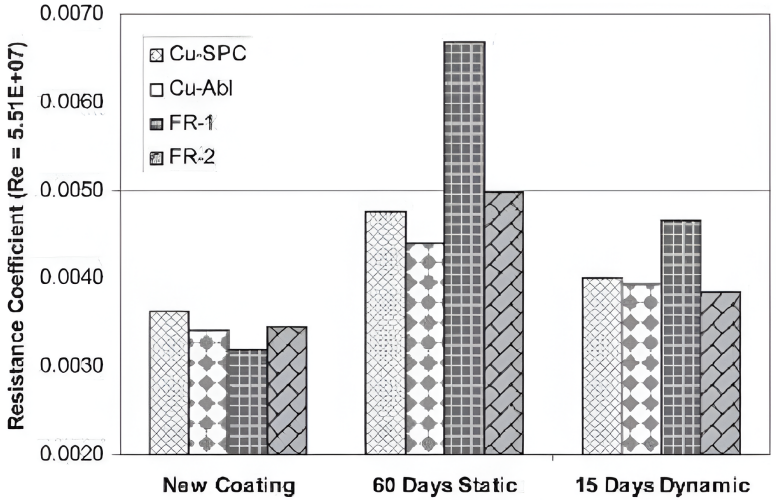

Figure 2.12: Frictional resistance coefficient for 25 knots of speed and $Re = 5.5 \times 10^7$ [40]

2.2. State of The Art

2.2.1. Analytical growth models

A growth model takes into account the effect of multiple process parameters to predict growth rate under outdoor conditions [41]. This section will cover first an overview of the variables that influence biofouling growth and attachment the most. Then, a presentation will be given on the main methods where such parameters are implemented to obtain a surface description. Most of the literature available focuses on hard fouling. Nonetheless, it is still possible to have an overview of the main variables that influence the growth of soft foulers.

Seawater surface temperature

Seawater surface temperature (SST) is often indicated in the literature as the most important factor to biofouling growth. That is up to the extent of considering only such variable in the development of certain models, like the one proposed by Uzun et al. [42]. In this, SST is correlated to the latitude of the area of the world in which the ship is navigating. Temperature changes due to longitude are completely neglected, as resultant differences are relatively small if compared to latitude ones [43].

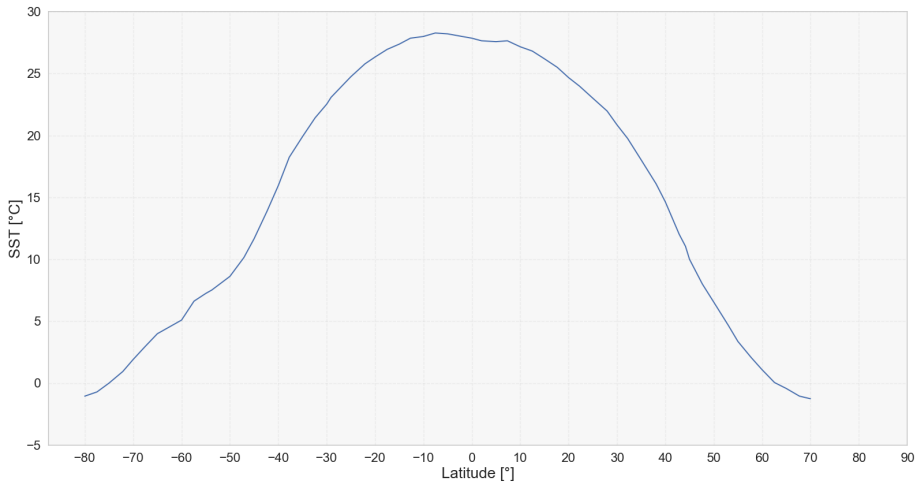

Figure 2.13: Sea Surface Temperature distribution based on latitude

Sea surface temperature is related to biofouling growth through relations involving the optimum, maximum and minimum temperatures, respectively T_{opt}, T_{max} and T_{min}. Despite not being applied to the specific case of ships, such equations can still be used and adapted to the study. For example, Bernard et al. [44] developed a model (Equation 2.13) to predict the change in photosynthetic rate of micro-algae by temperature, from modification of already existing equations.

$$\mu_T = \frac{(T - T_{max})\,(T - T_{min})^2}{(T_{opt} - T_{min})\,[(T_{opt} - T_{min})\,(T - T_{opt}) - (T_{opt} - T_{max})\,(T_{opt} + T_{min} - 2T)]} \tag{2.13}$$

Light intensity I and depth z

Microalgal organisms use light as a source of energy for their photosynthesis. This means that the availability of sunlight and its intensity will influence their growth rate. The main variable connected to light intensity is the depth of the soon-to-be fouled hull element. Both micro and macro photosynthetic species are common in the range between 0 and 40 meters of depth [42], meaning that ship hulls fall into such range. The relation between light intensity and z is provided by Beer-Lambert law in Equation 2.14. This states that I decreases exponentially with depth because of absorption by the water particles.

$$I = I_0 e^{-k_{att} z} \tag{2.14}$$

I_0 is the light intensity entering the media perpendicular to the surface, and k_{att} the attenuation rate. The latter is related to either biomass or chlorophyll concentration [41]. Most of the equations that link light intensity to microfouling growth rate μ are obtained from experimental setups to test specific species of algae. This implies that a model specific to the most expected organism should be used to obtain meaningful results. For example, Steele [45] proposes an approach that takes into account the photo-inhibition (Equation 2.15) of phytoplankton. This phenomenon consists in a reduction of the photosynthetic abilities of the organisms because of an extreme light intensity, which results detrimental. When the intensity reaches the optimal value I_{opt}, the growth rate is maximum and any further increase results in a decrease instead [41].

$$\mu = \mu_{max} \cdot \frac{I}{I_{opt} e^{1 - \frac{I}{I_{opt}}}} \tag{2.15}$$

The presented model only consider light intensity contribution towards biofilm growth. When multiple factors and marine species are included, it is not always possible to separate the elements with accuracy. This is why authors such as Uzun et al. [42] in their project assume light intensity to be equal throughout the water column, ultimately neglecting its effect on growth. Biofilm development is expected to be slower during rough weather, at least as far as photosynthetic capabilities are concerned. This aspect is however troublesome to integrate in a model, as climate conditions are fickle and ever-changing.

Presence of nutrients

Nutrients abundance is of critical importance for all fouling organisms: from bacteria responsible for biofilm formation, to barnacles. Among the main elements necessary for growth, nitrogen and phosphorous compounds, cobalt and iron are the most relevant [41]. The presence of such substances is connected to the distance of the ship from shore, since coastal waters are generally richer than open waters because of human produced discharges [42]. Several analytical models of nutrients influence on growth rate μ exist in the literature. Martinez et al. [46] proposed an equation that reproduces the behaviour analysed in previous experiments. It also considers the growth after consumption of all nutrients (Equation 2.16).

$$\mu = \frac{\mu_{m1} K_i S_n + \mu_{m2} S_n^2 + \mu_{m3} K_S K_i}{K_S K_i + K_i S + S_n^2} \tag{2.16}$$

K_S represents the substrate saturation model constant, and K_i the substrate inhibition model constant. S_n is the concentration of limiting nutrients. The ratios $\mu_{m1}, \mu_{m2}, \mu_{m3}$ represent respectively the maximum, inhibited and no-phosphorous growth rates of the considered species.

Surface colour

Surface colour influence on growth is studied through experiments on submerged panels painted with differently coloured coatings of same roughness. The immersion site is the same for all samples to reduce the influence of non-relevant variables (salinity, nutrients, sunlight).

Dobretsov et al. [47] conclude that light-colour paints are generally less subjected to fouling, with macrofouling density being higher on the black substratum up to 30 days of testing. The impact of colour on the formation of biofouling communities is instead progressively reduced over time [47]. This means that paint's colour on ships is not relevant after the establishment of the first biofilm layer. The study by Dobretsov et al. is the first to demonstrate the effect of colour on microfouling, as it proves the higher accumulation of chlorophyll on the surface [47] (Figure 2.14). Similar discoveries are reported by Swain et al. [48], reporting that the acrylic paint overlying the black background was, after the experiment, more heavily fouled than the white background. Figure 2.15 shows the result for submerged plates obtained by Salam et al. [49], who studied the influence of colour on growth for a wide array of coating colours.

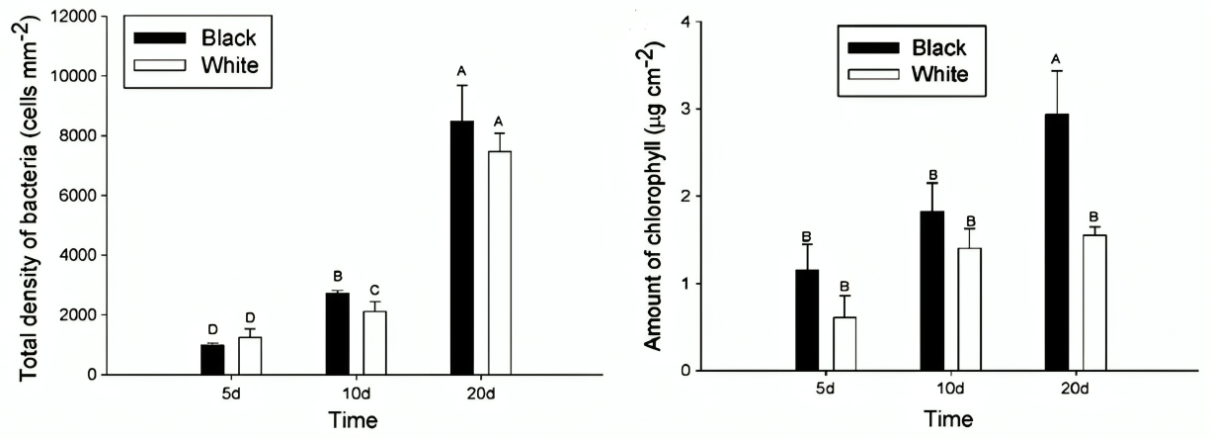

Figure 2.14: Bacteria density and amount of chlorophyll time trend for coating colours [47]

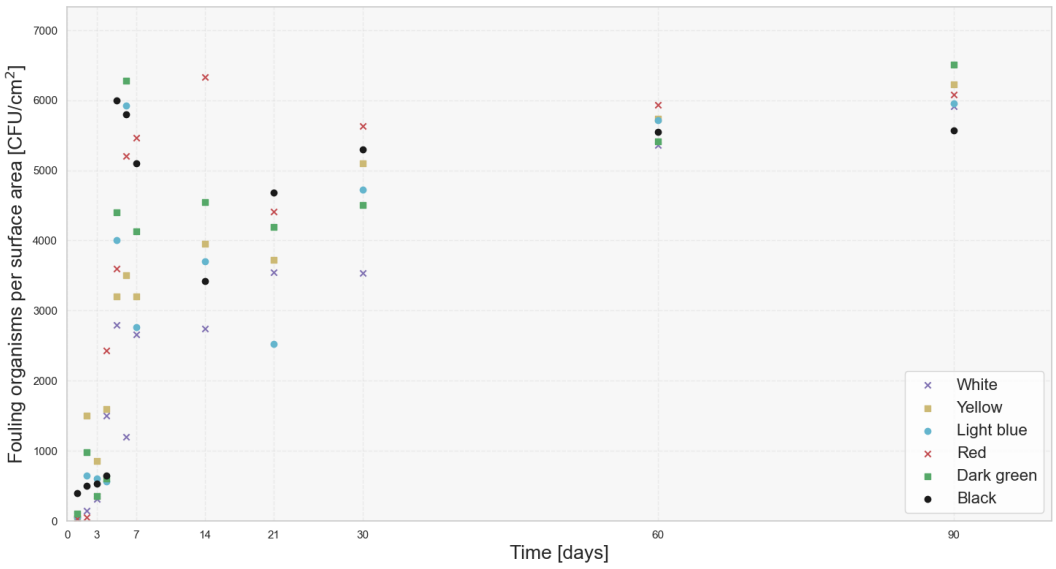

Figure 2.15: Number of organisms per surface area, based on Salam et al. [49]

Ship speed

Merchant ships spend a great part of their operational life sailing from one port to another to deliver cargo. The remaining share of their time is split between harbour operations (loading/unloading) and drydock. Despite this, the growth models currently available do not include the sailing time. Instead, solely the idle condition is accounted for: this is the most critical time, since most marine organisms attach more effectively to the surface when no flow-induced shear stress is present [42, 50]. As already mentioned in Section 2.1.1, one of the reasons why marine organisms attach to the hull is because of a fresh water flow, able to provide a steady flood of nutrients. Ship speed should however be regarded as a limiting factor for biofouling, both in terms of layer thickness and detachment. This is most important for FR coatings, which are designed to partially remove fouling through dynamic immersion [40].

Existing growth models

Currently there is no comprehensive growth model available in the literature, because of the great challenges its development would entail. These models tie together process parameters that increase the validation complexity as their number increase [41]. A higher number of involved variables thus requires a massive amount of data, for which extensive time and resources are needed. However, a few simple approaches have been recently developed. The most prominent attempt is given by Uzun et al. [42]. The authors propose a simplified time-based growth model, developed depending only on the exposure time t and antifouling coating performance η_c, function of ΔSST.

$$\mu = f(t, \eta_c) \qquad \eta_c = g(\Delta SST) \tag{2.17}$$

It is based on a number of simplifications [42]:

- Only the idle condition of ship in harbour is considered;
- The concentration of nutrients is accepted as identical for every port;
- Light intensity I is constant throughout the water column, and for the whole draft of the ship;
- Salinity is not included, since no mathematical model covers its effect [41];
- The applied coating type does not change through the operational life of the ship, and the environmental factors do not have any effect on its properties, exception made for η_c;

From field test data on submerged plates, biofouling accumulations were categorized into three groups: (A) slime, (B) non-shell organisms, and (C) calcareous fouling [42]. The plate area covered by each category A_i is used to express the Fouling Rating (FR) in Equation 2.18. This is also expressed in relation to the maximum rate of regression a, and to the performance parameters τ, t_0.

$$FR = 0.2 \cdot A_{(A)} + 0.5 \cdot A_{(B)} + 15 \cdot A_{(C)} \qquad FR = ae^{\left[-\left(\frac{t-t_0}{\tau}\right)^2\right]} \tag{2.18}$$

The growth rate can be calculated by considering the temperatures in conjunction with the geographic location. Multiplying the specific growth rate with the idle times, the fouling growth may be obtained (Equation 2.19). Such formulation does however not consider surface coverage.

$$FR_{tot} = \sum_{i=0}^{n} \left(\frac{\delta FR}{\delta t}\right)_i t_i + \left(\frac{\delta FR}{\delta t}\right)_{i+1} t_{i+1} + ... \tag{2.19}$$

2.2.2. Roughness in Computational Fluid Dynamics

The CFD code that will be used for the main part of the project is ReFRESCO (Reliable & Fast Rans Equations Ships Constructions Offshore). The availability of literature that carries out CFD simulations for biofouling evaluation on ReFRESCO is however limited, as this solver is intellectual property of MARIN. STAR-CCM+ represents a well-known and widely used substitute for simulations in the field, and related literature will be referenced for this stage only.

Until the end of the 20th century, CFD was only used in the academic environment due to its high cost and time-intensive nature. The recent developments in computational power have however led to a switch from experiments (i.e. towing tank experiments) to numerical simulations. There are a few reasons for this:

- CFD does not require any calibration of the experimental setup equipment [51], which normally induces uncertainty of the measurement parameters. Numerically, the uncertainty derives from the discretization method used to solve the Navier-Stokes equations, and it needs to be assessed through verification;
- Computational methods allow to have a visualization of the flow behaviour throughout the whole domain [52];
- CFD has no needs for prototypes, test facilities or expensive equipments. On the other hand, it requires a long time to obtain significant results and a powerful computer.

For roughness, CFD allows to fully appreciate the wave pattern modification due to surface roughness. It may have limitations while resolving small-scale roughness phenomena in large domains. This can become computationally prohibitive, leading to approximations or the use of averaged roughness parameters, which may not capture all the desired effects.

Computational methods

The choice of a certain computational method over another has profound consequences on the simulation results. Physical modelling of roughness sources on CFD is currently impossible because of the complex geometries they entail [20]. However, the relationship between roughness function ΔU^+ and roughness Reynolds number k^+ can be implemented in the wall function of the turbulence models [20].

Among the most common methods that solve the Navier-Stokes equations lies the Reynolds Averaged Navier Stokes (RANS). RANS evaluates turbulence through averaged equations that decompose the flow variables into a mean and fluctuating part [52]. This implies that the time-averaging scale determines the accuracy of the method. Their main advantage is given by reduced computational costs. The Unsteady variant of RANS (URANS) considers the unsteady terms and simulates turbulence unsteadiness to some extent, with a coarser grid. The use of URANS models allows to simulate the phenomena with a fully non-linear method [20, 53].

Differently from the approaches presented, the Direct Numerical Simulations (DNS) method resolves all turbulence, independently from the scale. This means that the only errors present will be the numerical ones [52]. DNS is usually exploited only for research purposes, as it requires great computational and time resources. In between RANS and DNS lies the Large Eddy Simulation (LES) method. This technique directly simulates the largest turbulence and models the effect of the smaller ones. From the analysed literature, the most commonly used methods are either RANS or URANS.

Wall functions

Wall functions are mathematical expressions used to link the viscosity affected region between wall and log-law region [54]. They do not accurately represent each flow type (smooth, transitional, fully rough), but they are in agreement with the real behaviour for only a portion of the total Reynolds numbers range. This means that the model implemented in the simulations should be chosen based on the expected flow regime and fouling type. The need for a definition of a wall roughness function ΔU^+ comes from the boundary layer velocity profile. Different equations connecting ΔU^+ and k^+ have been developed through the years. These can generally be divided into single regime (one equation) and three regimes functions. The most relevant are reported in the following paragraphs.

Grigson [55] and Apsley [56]

Song et al. [57, 58] and Farkas et al. [59] exploit the single-condition function in Equation 2.20. The function is used to model the effect of boundary layer modification due to hard fouling, especially barnacles [58]. It provides more accurate results for smooth and transitional flow regimes. Similar to Grigson is Apsley's [56] model in Equation 2.21. This considers the roughness Reynolds number k^+ divided by an empirical constant $A \approx 0.26$, and it is most indicated for the fully rough regime.

$$\Delta U^+ = \frac{1}{\kappa} ln(1 + k^+) \tag{2.20}$$

$$\Delta U^+ = \frac{1}{\kappa} ln\left(1 + \frac{k^+}{A}\right) \tag{2.21}$$

Demirel et al. [53]

Owen et al. [20] adopt the model developed by Demirel et al. [53], which consist in a three-conditions function that considers a different value for ΔU^+ depending on the flow regime (k^+). Comparisons with results previously obtained from experiments in the literature reveal that the function is not completely accurate for low values of k^+.

$$\Delta U^+ = \begin{cases} 0 & k^+ < 3 \\ \frac{1}{\kappa} \ln\left(0.26k^+\right)^{\sin\left[\frac{\pi}{2} \frac{\log\left(k^+/3\right)}{\log(5)}\right]} & 3 < k^+ < 15 \\ \frac{1}{\kappa} \ln\left(0.26k^+\right) & 15 < k^+ \end{cases} \tag{2.22}$$

Farkas et al. [60]

This model was developed for the impact prediction of biofilm on ship resistance, but it can also be used for evaluating the influence on propeller performance characteristics. Assuming a value of 0.42 for the Von Karman coefficient κ, Farkas' model includes various surface coverage SC conditions. Namely, a coverage of more than 25% corresponds to a fully rough flow, where viscous shear stress is negligible and frictional resistance is formed only because of roughness [60].

$$\Delta U^+ = \begin{cases} SC \geq 25\% & \begin{cases} \frac{1}{\kappa} \ln(0.27767k^+) & k^+ \geq 3.61 \\ 0 & k^+ < 3.61 \end{cases} \\ 10\% < SC < 25\% & \begin{cases} \frac{1}{\kappa} \ln(1.14492 + 0.0988k^+) & k^+ \geq 4.5 \\ 0 & k^+ < 4.5 \end{cases} \\ SC \leq 10\% & \begin{cases} \frac{1}{\kappa} \ln(1.06492 + 0.05332k^+) & k^+ \geq 4 \\ 0 & k^+ < 4 \end{cases} \end{cases} \tag{2.23}$$

Geometry and boundary conditions

It is important to select appropriate boundary conditions for CFD problems prior to simulations, since they directly affect the accurate flow solutions [20]. The majority of papers in the literature use a hexahedric domain that includes both air and water, This consists of an inlet, outlet, hull, side, upper and lower boundaries [61]. The distance of each edge is measured as a function of the length of the analysed object. For ships, this dimension is equivalent to the length between perpendiculars. Table 2.3 presents an overview of the most commonly adopted distances of the domain edges from the object. Half width is usually considered because accuracy is not compromised in any way by halving the domain, while it allows to reduce computational times.

Table 2.3: Overview of the domain characteristics and distances from plate/hull

Model	Type	Inlet	Outlet	Water depth	Upper limit	Half width
Demirel et al. [53]	Hull	$1.5L$	$2.5L$	$2.5L$	$1.5L$	$2.5L$
Demirel et al. [54]	Plate	L	$2L$	-	L	L
Zou et al. [61]	Hull	$3L$	$9L$	$5L$	$2L$	-
Song et al. [57]	Hull	$1.5L$	$2.5L$	$2.5L$	$1.25L$	$2.5L$
Farkas et al. [59]	Hull	$1.5L$	$3L$	$2.5L$	$1.5L$	$2.75L$

The distances are dependent on the authors and analysed situation. It is good practice to adopt an outlet distance that allows to investigate how the fluid behaves behind the hull. The inlet span should generate a fully developed fluid at the bow [20]. Sufficient space should also be available in the transversal direction to possibly register disturbances to the flow due to the presence of the hull. Demirel et al. [54] present a different domain from the rest of the papers, since a plate submerged in an infinite ocean is considered instead.

As far as the type of condition assigned to each of the boundaries is concerned, all authors agree in defining the inlet and outlet with respectively a velocity inlet and pressure outlet boundary condition. Hull or plate are implemented with a no-slip wall condition, to which a roughness function from Section 2.2.2 is integrated to consider the effect of biofouling. The remaining edges of the domain are however different for each paper, as reported in Table 2.4.

Table 2.4: Boundary conditions overview

Model	Bottom	Top	Side
Demirel et al. [53]	Velocity inlet	Velocity inlet	Velocity inlet
Demirel et al. [54]	Symmetry plane	Symmetry plane	Symmetry plane
Zou et al. [61]	Velocity inlet	Velocity inlet	Velocity inlet
Song et al. [57]	Slip wall	Slip wall	Slip wall
Farkas et al. [59]	Velocity inlet	Velocity inlet	Velocity inlet

The ordinary CFD analysis of the hull is coupled in the literature with a validation study carried out on a plate to simulate the conditions of a towing tank experiment. In this case, bottom and side of the computational domain are usually characterized with a no-slip condition to reproduce the solid walls of the tank.

Grid construction

The simulation software used for evaluating the hydrodynamic behaviour of ship and plate is STAR-CCM+, a complete multiphysics simulation solution software developed by Siemens. The mesh is built with the automated tool of the software, while additional refinements are applied to generate finer grids in critical regions [53]. These include trailing and leading edge of the plate, the area where the ship bow encounters the free surface or where water breaks with the stern, and the wake [53]. The computational domain is most times discretized with an unstructured hexahedral mesh, main output of the automatic generation, implemented with a cut-grid prism layer mesh around hull/plate [59]. An unstructured grid allows to model complex and irregular geometries and to refine the mesh where needed, while ensuring the computational resources are well allocated to capture the necessary details.

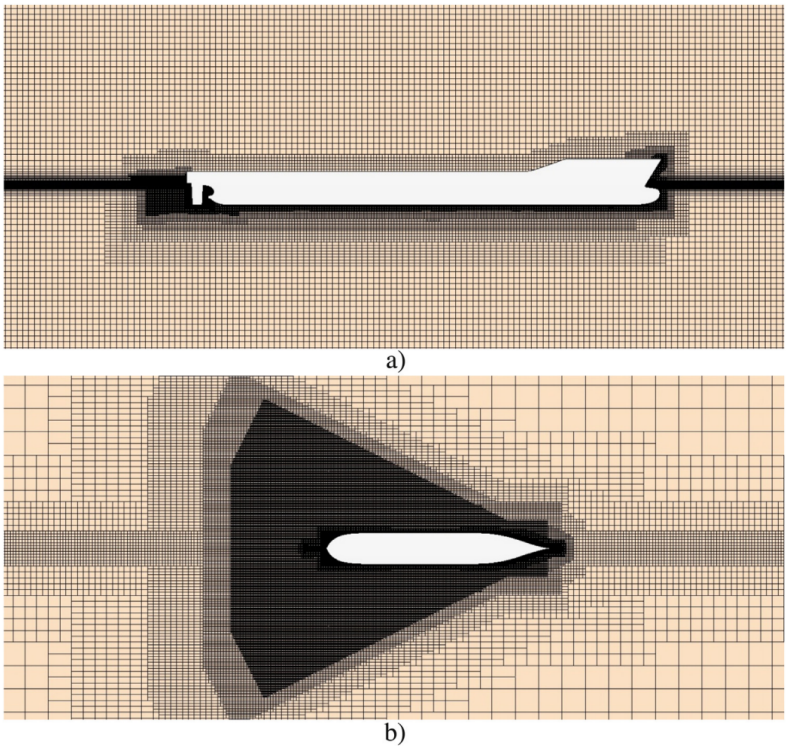

Figure 2.16: Mesh of the domain in a) profile and b) top view

Table 2.5 shows the correlation between the mesh cell number and surface roughness. It is evident that the grid needs to be more refined for lower roughness value, as it should be able to capture the smaller scale turbulence. The grid thickness is determined in such a way that y^+ is higher than 30 and than k_s [53]. The selection of the prism layer thickness is of particular importance, since it represents the boundary layer of the object and its gradients. The verification study to determine numerical uncertainties and the choice of the suitable mesh thickness will be discussed later.

Table 2.5: Total cell number for flat plate and full-scale KCS hull, based on Demirel et al. [53]

Surface condition (k_s)	Plate cell number	Hull cell number
$k_s = 0$, $k_s = 30$, $k_s = 100$, $k_s = 300$	5.5×10^6	4.09×10^6
$k_s = 1000$	5.28×10^6	4.00×10^6
$k_s = 3000$	4.5×10^6	3.70×10^6
$k_s = 10000$	4.0×10^6	3.58×10^6

Effect of fouling

Marine fouling varies in size, shape, hardness and density. Each of these characteristics has its own unique impact on the roughness of ship hulls and their hydrodynamic performance [61]. As already discussed in Section 2.1.2, the main effect of biofouling on ships is the modification of the boundary layer, which in turn generates additional frictional resistance. This phenomenon can be visualized in CFD simulations by analysing the velocity magnitude and the turbulent kinetic energy around the hull. Figure 2.17 shows the two cited characteristics for a smooth and heavy calcareous fouling hull conditions. It is evident how the turbulent kinetic energy increases with surface roughness, whereas the velocity magnitude decreases [53]. This is in agreement with the fact that the turbulent stress and wall shear stress rise, thus increasing C_F accordingly.

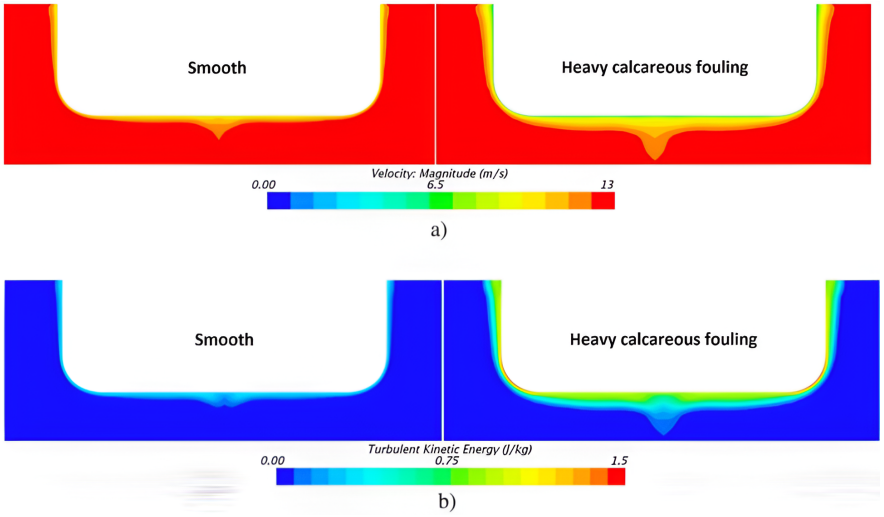

Figure 2.17: a) Velocity and b) turbulent kinetic energy contours amidship of a KCS hull for smooth and heavy calcareous fouling [53]

While the entire literature agrees on considering frictional resistance as heavily affected by biofouling and surface roughness, the same does not hold for residuary resistance C_R. Demirel et al. [54] claim that surface roughness only affects skin friction and justify with this the boundary conditions choice (Table 2.4). Demirel et al. [34] also consider C_R for a smooth plate equal to that of a rough surface in their experimental results. On the other hand, Farkas et al. [59], Zou et al. [61] and Demirel et al. [53] acknowledge that C_R is to some extent influenced by biofouling.

According to Demirel et al. [53], residuary resistance coefficients show an increasing trend for heavy fouling conditions at a speed of 19 knots, while at 24 knots the trend is inverse [53]. This behaviour can be implied to the dominance of wave-making resistance at higher speeds in comparison to viscous pressure resistance (see Figure 2.11), function of C_F through the form factor k. Such a trend is confirmed in Table 2.6, where the effect of a particular fouling condition on wave resistance is less relevant at lower speeds [53]. Figure 2.18 also corroborates what above explained, but highlights the small differences in C_P versus k_s (here indicated as k_G) because of C_{VP} and C_W opposite trends. In the former, surface roughness decelerates the fluid around the ship stern, enlarging the wake field which interacts with the pressure distribution [58, 61]. For the latter, the influence of k_s consists in a velocity reduction below the free surface behind the hull, causing reduced wave elevation.

Table 2.6: Computed $\%\Delta C_W$ for full scale KCS hull [53]

Description of condition	24 knots	19 knots
Hydraulically smooth surface	–	–
Typical as applied AF coating	−4.4	−5
Deteriorated coating or light slime	−15.2	−17.9
Heavy slime	−23.2	−30.1
Small calcareous fouling or weed	−32.2	−43.8
Medium calcareous fouling	−43	−57.9
Heavy calcareous fouling	−55.8	−72.3

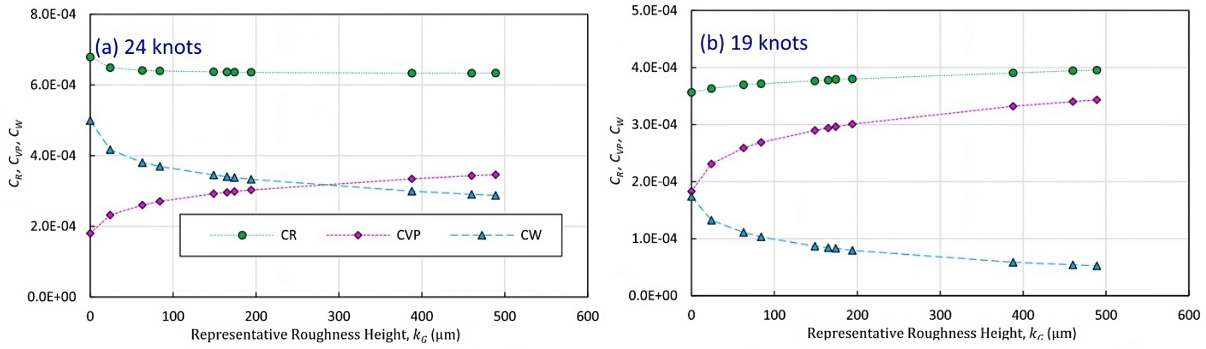

Figure 2.18: Comparison of residuary, viscous pressure and wave making resistance versus representative surface roughness height at a) 24 knots and b) 19 knots

What previously stated for the wave making resistance can be further investigated by analysing the generated wave profile. Song et al. [58] observed that the wave profile generated in the simulations for smooth and rough hull are generally equivalent, exception made for the area downstream of the ship. This is also confirmed in Demirel et al. [53] for the heavy calcareous fouling condition, where wave amplitudes appear to be reduced by roughness effects.

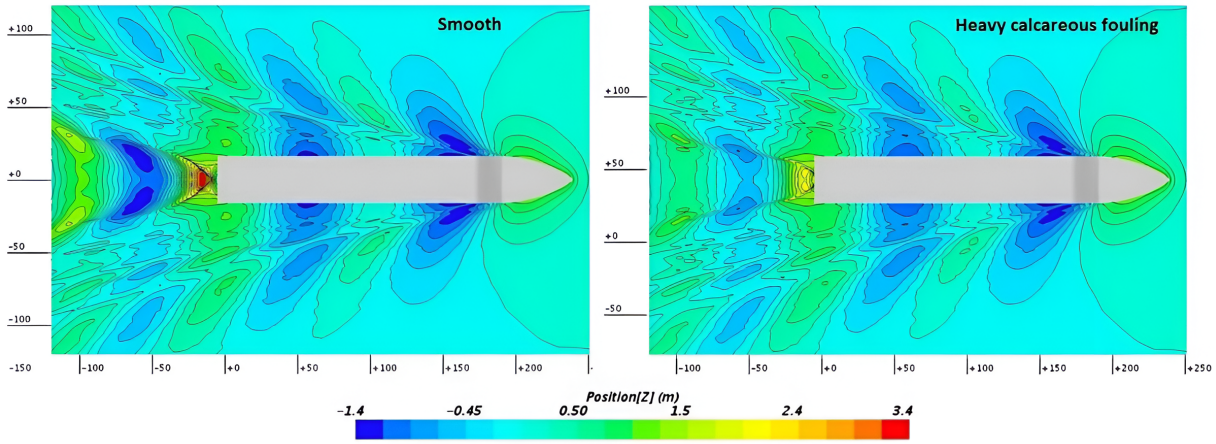

Figure 2.19: Wave pattern around KCS hull for smooth and heavy calcareous fouling condition

Uncertainty Evaluation

When conducting a CFD simulation, several types of errors are present. These should be estimated to understand how accurate the obtained results are. In particular, there could be:

- numerical errors deriving from discretization of the equations and approximated methods used in the simulations, which lead to deviations from the true solution;
- numerical errors occurring while making assumptions about geometry and boundary conditions;
- convergence errors, arising from insufficient mesh refinement.

The most widely used method to evaluate these uncertainties is the Grid Convergence Index (GCI) based on Richardson extrapolation [19, 20, 53, 58, 62]. This consists in the creation of at least three meshes (fine, medium and coarse), each obtained from the other by increasing or reducing the grid refinement of the same amount r_{21} (and r_{32}). From literature, this value is usually taken as $\sqrt{2}$ [20, 53]. The order of convergence p_a is calculated through the following equation:

$$p_a = \frac{1}{\ln(r_{21})} |\ln \left| \frac{\phi_3 - \phi_2}{\phi_2 - \phi_1} \right| + q(p_a)| \tag{2.24}$$

with ϕ_1, ϕ_2 and ϕ_3 being respectively the results of the coarse, medium and fine mesh. The term $q(p_a)$ can be neglected if the refinement ratios are taken as equal, otherwise:

$$q(p_a) = \ln \left(\frac{r_{21}^{p_a} - s}{r_{32}^{p_a} - s} \right) \qquad s = \text{sign} \left(\frac{\phi_3 - \phi_2}{\phi_2 - \phi_1} \right) \tag{2.25}$$

The extrapolated values are obtained by Owen et al. [20], with their relative errors in Equation 2.26. It follows that the GCI is as indicated in Equation 2.27.

$$\phi_{ext}^{21} = \frac{r_{21}^p \phi_1 - \phi_2}{r_{21}^p - 1} \qquad e_a^{21} = \left| \frac{\phi_1 - \phi_2}{\phi_1} \right| \qquad e_{ext}^{21} = \left| \frac{\phi_{ext}^{12} - \phi_1}{\phi_{ext}^{12}} \right| \tag{2.26}$$

$$GCI_{fine}^{21} = \frac{1.25 e_a^{21}}{r_{21}^p - 1} \tag{2.27}$$

It should also be checked that the convergence analysis is carried out within the asymptotic range of convergence, so that the solution is independent of the grid. With three grids:

$$\frac{GCI_{2,3}}{r^p \cdot GCI_{1,2}} \simeq 1 \tag{2.28}$$

2.3. Knowledge Gaps

Based on the findings from this chapter, some knowledge gaps can be identified. These are directly related to the formulation of the research questions in Section 1.3.

- No complete equation used in official regulations is currently available for an accurate evaluation of frictional resistance increase due to surface roughness (Section 2.1.2);
- The growth models only take into account the idle condition of the ship, since it is at that time that biofouling develops more rapidly. No reference is made to the sailing condition (Section 2.2.1);
- Lack of comprehensive analytical growth models that consider more influencing factors simultaneously (Section 2.2.1).
- It is not clearly understood how and to which degree residuary resistance is influenced by surface roughness (Section 2.2.2);

3 Methodology

3.1. Dataset description

The dataset that will be used in the project is related to a containership with approximate dimensions reported in Table 3.1. The vessel is equipped with six sensors: four acoustic correlation logs (AC1-AC4) installed at frame 150, a Doppler log (DC) and another acoustic correlation log (AC-5) positioned at the bow.

Table 3.1: Main particulars of the containership

Parameter	Notation	Value	Unit
Length overall	L_{oa}	$\simeq 200$	m
Length between perpendiculars	L_{pp}	$\simeq 180$	m
Breadth	B	$\simeq 30.0$	m
Design draught	T	$\simeq 10.0$	m
Container capacity	C_c	$\simeq 2000$	TEU
Deadweight	DWT	$\simeq 20000$	t
Design speed	V	20.5	kn

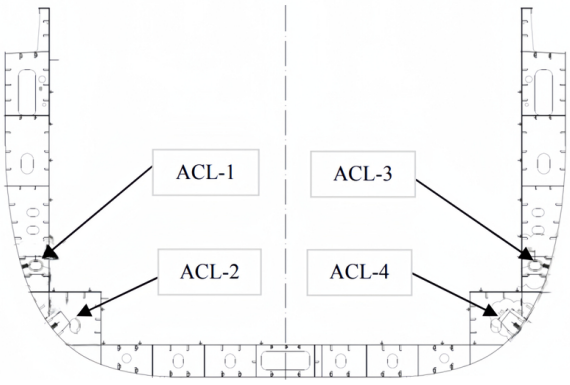

Figure 3.1: Position of the correlation logs [63]

The dataset contains information of various nature for the period January 2012 - December 2016. The routes of the ship are shown in Figure 3.2. The sampling rate for each sensor was set to 1 Hz, generating a measurement per second and for a total of 86400 daily recordings. Table 3.2 shows an overview

of the main conditions, as well as the instrument used to gather them. These provide an overview of the operational conditions of the ship, as well as of the external environmental variables. Current and wave characteristics were not directly measured on board, but they were integrated through weather hindcasts from the ERA-5 Database.

Doppler log speed is measured through velocity and direction of water currents relative to the ship's motion. Its operation involves the transmission of an ultrasonic signal that measures the frequency shift of the signal, as it bounces off of water particles. This implies that non-null speeds may be registered even when the ship is at anchor, because of ocean current speed and direction. Such an aspect should be carefully considered during data filtering, and while evaluating the resistance profile of the containership. The acoustic correlation logs will also be influenced by the presence of the boundary layer and its modifications due to drifting events.

Table 3.2: Monitored and implemented variables

Instrument	Variable	Unit
Anemometer	Wind angle	°
	Wind Speed	kn
Shaft sensor	Power	kW
	Torque	kNm
	Revolutions	rpm
Hydrometer	Density	t/m^3
	T_{fore}	m
	T_{aft}	m
GPS	Latitude	°
	Longitude	°
	Date	-
Doppler log	Speed	kn
Gyroscope	Heading	°
ERA-5 Database	Current speed	m/s
	Current direction	°
	Wave height	m

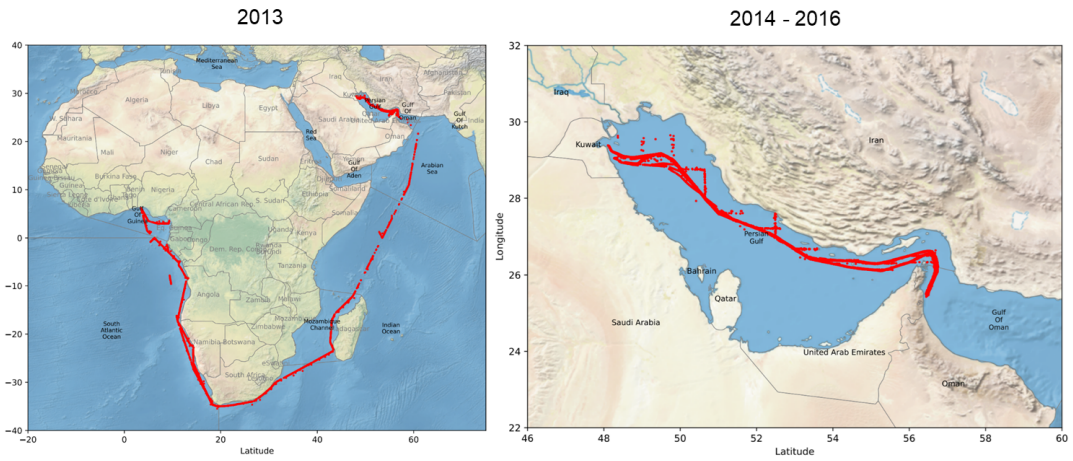

Figure 3.2: Routes of the containership [63]

3.1.1. Data Filtering

Data cleaning is carried out by analysing first the distribution of the variables. This is done via skewness Sk and kurtosis K: the former gives an indication on the asymmetry, while the latter measures the sharpness of the peak. Normal distributions are characterised by null values for both variables. Table 3.3 shows skewness and kurtosis per year, for the main variables used. Density ρ is the only characteristic that has a Gaussian distribution for all years but 2013. Speed V and heading H_c have an acceptable skewness, while their kurtosis suggests the presence of extreme outliers that should be filtered out. Shaft power P_S, revolutions rpm and torque Q have more asymmetric distribution, and K provides evidence of long tails. The p-values are also checked, and show a normal scatter only for density in the years with $Sk = K = 0$. The standard deviation σ is also reported to provide an indication of the uncertainty related to each variable. The measurement unit for σ is not reported for visualization purposes, but it is equal to that of the related variable.

Table 3.3: Skewness and kurtosis for statistical distributions per year, before filtering

Year	Sk_V	K_V	σ_V	Sk_ρ	K_ρ	σ_ρ	Sk_{H_c}	K_{H_c}	σ_{H_c}	Sk_{P_S}	K_{P_S}	σ_{P_S}	Sk_{rpm}	K_{rpm}	σ_{rpm}	Sk_Q	K_Q	σ_Q
2012	−0.11	4.69	2.21	0	0	0	1.46	19.8	28.5	0.72	9.69	1302	0.21	6.00	12.6	0.39	7.30	132
2013	0.53	5.59	3.02	−27.3	1523	0.01	−0.24	2.85	56.8	2.23	65.4	1159	1.23	30.9	16.5	1.82	57.1	142
2014	0.72	5.95	3.03	0	0	0	−0.95	140	56.8	2.96	107	1149	1.91	57.3	16.9	2.55	92.4	148
2015	0.60	10.9	0.60	0	0	0	−0.29	3.62	50.4	5.59	306	790	4.41	260	12.9	4.54	192	101
2016	0.98	6.31	2.79	0	0	0	−0.40	2.46	61.3	5.94	217	11751	5.70	216	68.3	3.24	106	151

Depending on the values of skewness and kurtosis of the daily measurements (≈ 86400), the most appropriate filtering technique is chosen. Chauvenet's criterion is most indicated for data that approximate a normal distribution ($-1 \leq Sk \leq 1$, $-2 \leq K \leq 2$). The method allows to create an acceptable band of data around the mean value, providing a condition to identify outliers. It states that, given the dataset length N, if the probability of occurrence of a certain measurement is less than $1/2N$, then the associated datapoint x_i is an outlier. The procedure involves the calculation of the mean and standard deviations of the dataset, respectively μ and σ, and of the cumulative density function Φ. Non numeric and unavailable measurements are momentarily filtered out to obtain the effective statistical distribution. A preemptive check for time domain measurement duplicates is also performed. Equation 3.1 shows the filtering condition for outliers identification. The procedure is applied twice, as this allows to remove the extremes first, and then refine the distribution further.

$$1 - \Phi\left(\frac{|x_i - \mu|}{\sigma}\right) < \frac{1}{2N} \tag{3.1}$$

When Sk and K are outside the range indicated for Chauvenet, the Interquartile Range (IQR) method is applied. This is based on measuring the spread of the middle 50% of the data, and identifying all points outside the first and third quartiles as outliers. Furthermore, all columns deemed unnecessary for the scope of the project are filtered out: sensor alarms and quality measurements, speeds from acoustic correlation logs, and ship motions. This allows to speed up the reading time of the total multi-year dataset in Python: from a starting 20 billions measurements, approximately 3 billions are reached. An additional filtering condition is provided for the speed: measurements with $V < 1\ kn$ are disregarded when referring to variables dependent on V (P_S, t, w). This is done because speed measurements under the set limit hold small significance on resistance evaluation, and may present sensors uncertainties. Table 3.4 show the statistical values after filtering is applied.

Table 3.4: Skewness and kurtosis for statistical distributions per year, after filtering

Year	Sk_V	K_V	σ_V	Sk_ρ	K_ρ	σ_ρ	Sk_{H_c}	K_{H_c}	σ_{H_c}	Sk_{P_S}	K_{P_S}	σ_{P_S}	Sk_{rpm}	K_{rpm}	σ_{rpm}	Sk_Q	K_Q	σ_Q
2012	−0.01	0.06	0.95	0	0	0	−0.11	0.26	18.9	0.07	−0.13	600	−0.02	−0.32	3.31	0.04	−0.30	55.8
2013	0.15	−0.65	0.18	0	0	0	0.02	−0.26	19.5	−0.01	−0.26	356	−0.08	−0.26	1.41	0.03	−0.34	1.41
2014	−0.03	0.67	2.03	0	0	0	−0.15	0.91	48.5	−0.09	−0.09	644	−0.36	−0.01	4.96	−0.13	−0.02	71.6
2015	−0.07	0.14	1.76	0	0	0	−0.07	0.20	40.6	0.01	0.15	550	−0.23	0.32	4.56	−0.03	0.13	66.1
2016	0.03	2.50	1.48	0	0	0	−0.12	−0.40	35.5	0.19	−0.27	5491	−0.08	−0.17	31.3	0.02	−0.31	39.6

3.1.2. Data Processing & Enrichment

Two datasets are produced: one containing the total filtered data, and another that considers the daily average of all measurements. The former is used to derive the uncertainty of the variables, and the latter for resistance trend and growth model. This is done to reduce the running time of the script, as biofouling growth can be captured only in the long term, while hourly changes can be neglected. In such a way, the total dataset becomes of size 1492×20. All measurements also need to be converted into International System of Units.

Despite filtering and processing, the datasets still present many unavailable data that can be further modified to facilitate the development of the models. Namely, the provided set of data does not contain information for some of the days of the observation period. Table 3.5 reports the missing portions of the dataset. These amount to 19.5% of the total period, and they are added to the comprehensive dataframe as ”NaN” values.

Table 3.5: Missing days for the provided set of data

Year	Period	Year	Period
2012	31/08	2015	24/02→ 27/02
	30/11		21/04
2013	31/01		01/05 → 30/05
	28/02		01/12 → 31/12
	31/03	2016	13/03 → 02/04
	03/04 → 29/04		30/05
	01/05 → 29/06		01/06 → 29/06
	31/10		01/07
	31/12		20/07
2014	02/04		31/07 → 01/08
	30/05		20/08
	01/07 → 30/07		30/09 → 31/12

As previously explained, the dataset provides information on four different drafts of the ship: midship starboard and port, connected to heeling monitoring, and aft and fore drafts for trim. These draughts are most of the time not monitored. Also, no knowledge on any of the geometrical characteristics from hydrostatic tables is available. Because of this, forward and aft drafts gathered through noon reports by the Master are implemented in the dataset. Despite the intrinsic uncertainty given by human errors while reading the draught values, they still provide a better estimate of the real operational condition of the ship. This would otherwise be unknown and defined with even less precision. Additional missing data is then integrated by assuming that the ship will operate in its optimal condition, which means at its design draft. The resultant time evolution of draft throughout the considered period is shown in Figure 3.4.

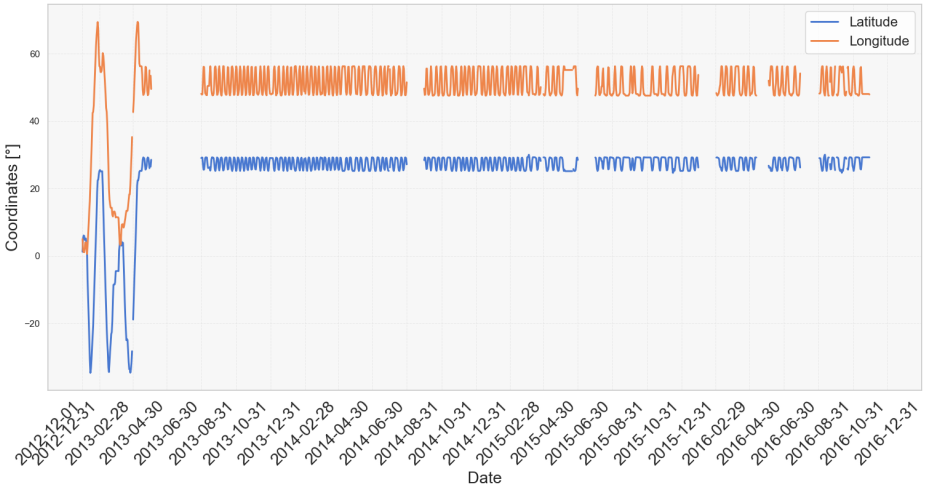

Figure 3.3: GPS coordinates of the ship

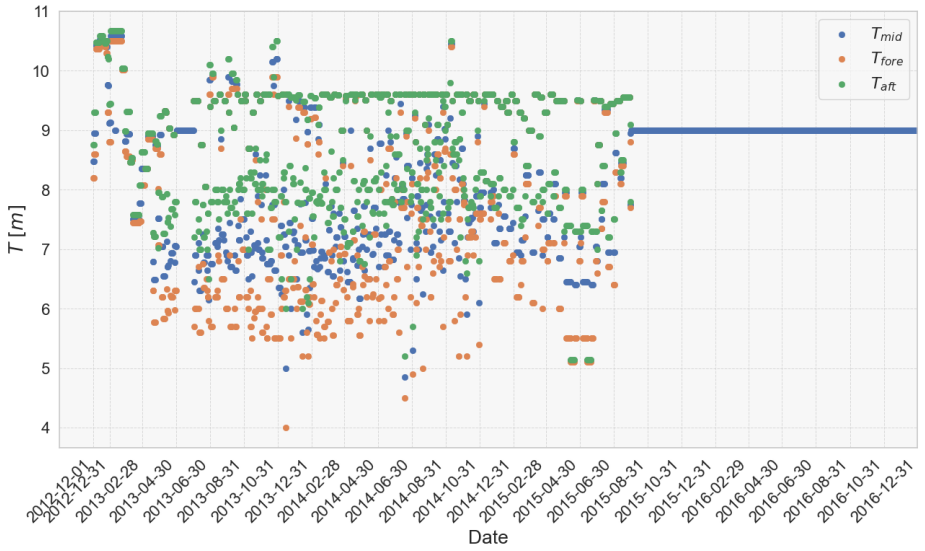

Figure 3.4: Forward, aft and averaged midship drafts evolution

The dataset already contains a few environmental characteristics representative of the area in which the containership is operating. Such information is however not always available for each day of the desired time period. For this reason, weather hindcasts are integrated when needed. This is the case of current speed and direction, and wave information (height, period, direction). For these, the data would otherwise be available only in the period December 2012 - April 2013. The archive used is Copernicus [64], from which non-filtered information is gathered with GPS position and date as only inputs. Such an approach is adopted to obtain daily light intensity I_0 as well, which will be used as described in Section 3.3.2. Water density missing values are on the other hand implemented through the well-known $\rho = 1025\ kg/m^3$. Additional environmental variables are implemented in the dataset via experimental evidence from literature. This is the case for sea surface temperature, which can be evaluated with the latitudinal GPS position and Figure 2.13 from Uzun et al. [50]. Similarly, the mole concentration of phosphate PO_4 is implemented with latitude and longitude of the ship through Copernicus Marine [65].

3.2. Resistance evaluation

The evaluation of the resistance profile allows to understand what is the evolution of added frictional resistance ΔC_F, and thus the biofouling status on the ship. Information on the main maintenance events can also be obtained from it. To do so, the shaft power P_S from the dataset is related with the effective power P_E through the efficiency chain, as reported in Equation 3.2. Among the provided information for the containership, open water and self-propulsion model test results are available. This means it is possible to evaluate the single efficiencies and thus implement η_{tot}. As reported in Equation 3.2, the total efficiency allows to consider the energy losses from the position where the shaft sensor is installed, up to the wake of the ship.

$$P_E = P_S \eta_{tot} = P_S \eta_H \eta_O \eta_R \eta_S \tag{3.2}$$

The shaft efficiency η_S varies with the rotational speed due to frictional effects in the bearings. After thorough evaluation of standards and common practices, a constant value of 0.99 is assumed: this is in contrast to $\eta_S = 0.98$ chosen for the ship in power prediction phase. The higher efficiency can be justified for the project by the position of the shaft sensor, through which P_S is acquired, aft of the main bearing. This means that a portion of the friction is not included in the measured power, thus implying lower losses. The gearbox efficiency η_G is disregarded, since the ship is equipped with a 2 strokes engine. The relative rotative efficiency η_R, together with the thrust deduction factor t and wake fraction w, constitute the propulsive coefficients. These are available from self propulsion tests for a range of speeds between 16 and 20 knots. The lower range is included through the BSRA regression series (see Equations 3.3, 3.4 and 3.5). The applicability of such methodology depends on how similar the containership geometry is to the hulls of the systematic serie. Since they are characterised by one propeller, flat bottom, vertical sides and block coefficient in the order of $C_B \simeq 0.7$, the propulsive coefficients may be used. Once the values are known, the hull efficiency $\eta_H = (1-t)/(1-w)$ is obtained accordingly. It is however assumed that it is not influenced by biofouling. Finally, the open water efficiency η_O is available through the homonymous propeller test results, given the advance ratio $J = V(1-w)/(nD)$ as input.

$$w = a_0 + a_1\, C_B + a_2\, C_B^2 + a_3\, C_B\, \frac{V}{\sqrt{L_{wl}}} + a_4\, C_B^2\, \frac{V^2}{L_{wl}} + a_5\, C_B\, D_w + a_6\, \delta LCB \tag{3.3}$$

$$\begin{aligned} t = b_0 + b_1\, C_B + b_2\, C_B^2 + b_3\, \frac{1}{C_B}\, \frac{V}{\sqrt{L_{wl}}} + b_4\, \frac{1}{C_B^2}\, \frac{V^2}{L_{wl}} + b_5\, \frac{1}{C_B^3}\, \frac{V^3}{L_{wl}^{3/2}} + \\ + b_6\, \frac{V}{\sqrt{L_{wl}}} + b_7\, D_t + b_8\, \delta LCB + b_9\, C_B\, \delta LCB \end{aligned} \tag{3.4}$$

$$\eta_R = c_0 + c_1\, C_B + c_2\, C_B^2 + c_3\, C_B\, \frac{V}{\sqrt{L_{wl}}} + c_4\, \frac{D}{\nabla^{1/3}} \tag{3.5}$$

δLCB represents the distance between the standard x-coordinate of the centre of buoyancy and the real value. D_t and D_w are instead used as non-dimensional numbers of the propeller diameter.

$$\delta LCB = LCB_{PPam} - 20(C_B - 0.675) \qquad D_t = \frac{BD}{\nabla^{2/3}} \qquad D_w = \frac{B}{\sqrt{\nabla^{1/3} D}} \tag{3.6}$$

The resultant efficiencies are shown in Figure 3.5. Given the effective power, the total resistance coefficient C_T can be calculated through the wetted surface of the ship S in Equation 3.7.

$$C_T = \frac{P_E}{\frac{1}{2}\rho S V^3} \tag{3.7}$$

Since the additional frictional resistance due to hull roughness has to be obtained, Holtrop & Mennen [37] method is used to determine the components of C_T reported in Equation 3.8. The applicability of

the methodology for the containership is checked, and the conditions are satisfied (see Appendix C).

$$C_T = C_F(1+k) + C_W + C_{bulb} + C_{transom} + C_A \tag{3.8}$$

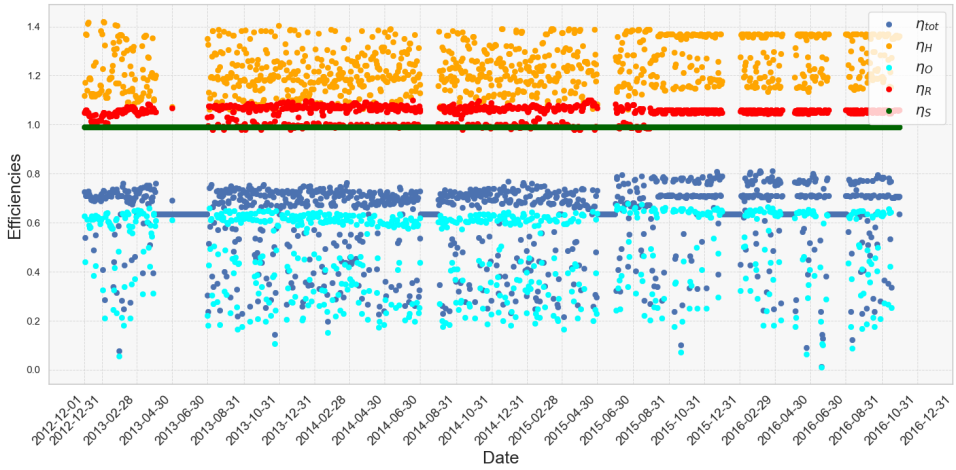

Figure 3.5: Efficiencies time evolution

Equation 3.8 is used to obtain a general estimation of the total resistance in still water conditions: environmental forces should therefore be added. Furthermore, the correlation allowance coefficient C_A includes multiple contributes. Beside a resistance increase due to hull roughness, possible instrumentation errors and a correction for carrying out towing tank experiments in partial Froude similitude are encompassed in C_A. Since the former two elements are not relevant for the project, it is decided to isolate the hull roughness component into a frictional resistance increase ΔC_F. The total resistance coefficient can then be rewritten as in Equation 3.9. The resistance of the appendices is not included, since none is present in the ship.

$$C_T = C_F(1+k) + C_W + C_{bulb} + C_{transom} + \Delta C_F + C_{wind} + C_{waves} + C_{current} \tag{3.9}$$

While the formulations used to evaluate the original resistance components are reported in Appendix C, Equations 3.10 and 3.11 provide respectively the added resistance due to wind and waves. In both cases, the relative direction with the ship is taken into consideration, and only the component aligned with its heading contributes to the resistance. The Newton number for wind resistance is obtained through the wetted surface of the ship S, while speed V_{wind} and pressure p_{wind} are enriched from the mentioned weather hindcasts, and using the Beaufort scale based on the speed. Similar reasoning applies to C_{waves}. Force and speed associated to the waves are obtained through the height H_{waves} and period T_{waves} previously implemented in the dataset with Copernicus Marine [65]. Ocean current is not included as an additional resistance component, since it is already accounted for in the measured speed: V is gathered through a speed log that is influenced by the current flowing against it.

$$C_{wind} = \frac{p_{wind}}{\frac{1}{2}\rho S V_{wind}^2} cos(\theta_{wind} - \theta_{ship}) \tag{3.10}$$

$$V_{waves} = \frac{gT_{waves}}{2\pi} \qquad F_{waves} = \frac{1}{2}\rho g H_{waves} \qquad C_{waves} = \frac{F_{waves}}{\frac{1}{2}\rho S V_{waves}^2} cos(\theta_{waves} - \theta_{ship}) \tag{3.11}$$

In conclusion, the added frictional resistance due to hull roughness is isolated from the other components in Equation 3.12.

$$\Delta C_F = C_T - (C_F(1+k) + C_W + C_{bulb} + C_{transom} + C_{wind} + C_{waves}) \tag{3.12}$$

3.3. Growth model development

3.3.1. Modelling assumptions

As previously mentioned in Section 2.2.1, some assumptions should be made to simplify the model and avoid validation problems deriving from the great amount of variables otherwise implemented. This stems from the fact that the dataset does not provide information on all of the characteristics that should be considered for growth. Equation 3.13 shows the biofouling growth rate μ as a function of some of the variables analysed in Chapter 2, and following Uzun et al. [42] methodology.

$$\mu = f(t, SST, psu, I, z, P, C, \sigma, V, \eta_c, k_{coating}) \tag{3.13}$$

The assumptions are carried out in such a fashion to still consider the main elements involved in biofouling growth, with greater focus on the environmental conditions and operational profile of the ship. The following simplifications have been carried out:

- Salinity psu: it does not influence the growth directly, but instead the attachment of the species. Since a biofilm consists of multiple organisms, it is generally difficult to define with precision a specific psu. As it is connected to water density ρ, it is implicitly included in the computational simulations through the resultant shear stress values (Equation 3.14). This way it is then possible to assess whether the biofilm detachment occurs or not;

$$\tau_w = \mu_w \frac{\partial u}{\partial y} = \frac{\nu}{\rho} \frac{\partial u}{\partial y} \tag{3.14}$$

- Antifouling coating performance parameter η_c: the variable is heavily dependent on sea surface temperature variations and may be determined through immersion field tests. It is therefore decided to disregard it to avoid adding further uncertainties to the model, considering the lack of available data in the literature;
- Surface energy σ: for the present project it is neglected. This is due to the fact that it does not affect the growth rate itself, but rather the detachment of the biofilm for ships applied with Foul Release coatings;
- Painting roughness $k_{coating}$: although it should be considered when determining how easily the initial biofouling colonies attach to the hull, it will only be accounted for when evaluating the time evolution trend of the equivalent sand-grain roughness height k_s.

The comprehensive final growth rate model, that takes into account the aforementioned assumptions, is reported in Equation 3.15. It should be highlighted that the speed's influence on biofouling will not be analysed independently, but it will instead be included indirectly with an additional factor alongside the other variables.

$$\mu = f(t, SST, I, z, V, P) \tag{3.15}$$

The model does not account for the likelihood of attachment, but it assumes that foulers developing near the hull will attach to it entirely. In addition, the growth rate μ would be physically expressed in terms of biofilm thickness increase $[mm/day]$. The lack of equations in the literature however leads to considering this variable in $[1/day]$ units, for which equations and constants are already available. This allows to associate the growth rate with fouling rating FR_{tot} first, and then with equivalent sand-grain roughness height k_s.

3.3.2. Influencing variables

Surface colour

Surface colour is here analysed and implemented in the model through already existing literature only. Starting from the biological samples results shown in Figure 2.15, a validation attempt is carried out by comparing these results with the ones obtained by Dobretsov et al. [47] in Figure 2.14. This is done by evaluating the ratio between total density of bacteria grown on a black and white surface for the two experimental tests. Such a procedure is deemed necessary to provide more consistency to the limited available data. Furthermore, the ratio needs to be taken into account to normalize the results with respect to the environmental conditions. These would otherwise compromise the validation due to the great influence they have on biofouling density.

Table 3.6: Black/white surface ratios of total fouling density

Experimental setup	5 days	10 days	20 days
Salam et al. [49]	2.14	1.24	1.32
Dobretsov et al. [47]	3.66	1.33	2.51

As it can be noticed from Table 3.6, the ratios between black and white surface coatings for the two experiments have same order of magnitude, but different values. Salam's results may therefore be used to obtain an approximated trend of how growth rate is influenced by the colour of the applied paint.

Figure 3.6 shows the soft foulers density on a white surface. The behaviour for other coating colours is illustrated in Appendix B. The trend line is obtained by fitting a quadratic polynomial to the biological sample data reported in Figure 2.15, deriving from Salam et al. [49]. From 90 days onward, at the red line, the curve is made constant for two reasons: the referred literature does not contain any information on longer time periods, and it is stated that the growth rate is expected to be neglectfully influenced by the coating's colour in the long term. It is therefore reasonable to assume $\mu_{colour} = 0$ after such time frame, as the density remains constant and the rate is expressed as its derivative with respect to time.

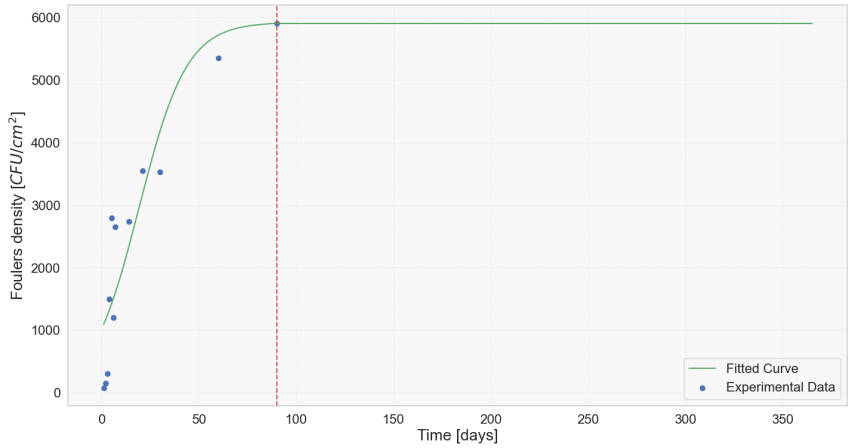

Figure 3.6: Foulers density for white surface

Due insufficient available data, the effect of surface colour is disregarded. As explained in Chapter 2, the entirety of previous research focuses solely on the biological standpoint of fouling. This entails that no connection to either surface roughness or drag is given, and the lack of information on the matter would create great uncertainties in the comprehensive growth model. In addition to that, both Dobretsov [47] and Salam et al. [49] refer to fouling density in CFU/cm^2. This unit cannot be directly related to the more classical formulation for the growth rate ($1/day$), unless a description of the connection between density of bacteria and thickness of the biofilm is provided. It is possible to conclude that CFU/cm^2 does not constitute a suitable quantification of fouling, as far as the development of a growth model for ship resistance is concerned.

Light intensity

Light intensity is recognized as one of the main variables influencing biofouling growth. An accurate quantification of its impact may be carried out through information on weather forecast. The formulation chosen to correlate these variables is based on the model by Steele [45] in Equation 2.15, modified to account for the operational profile of the ship. As already indicated in Section 3.1.1, the daily speed measurements are filtered to count the total number of velocities lower than 1 knot, here called $N_{V<1kn}$. A threshold of $1\ kn = 0.514\ m/s$ is deemed sufficiently low to carry out the filtering, since the measurements in the dataset may contain errors that prevent perfectly zero speeds. These may be due to incoming ocean current or doppler-log uncertainty. $N_{V<1kn}$ is then divided by the total number of filtered daily speed measurements N_{total}. This adjustment allows to include the relevance of each operative day and the effect of speed into the growth rate, which is known to be higher when the ship is stationary in harbour or at anchor. Equation 3.16 presents the adapted light intensity growth rate formulation, with optimal light $I_{opt} = 180000\ lux$, corresponding to a sunny day at the Equator. The equation is fitted from experimental data, where the carbon fixation (conversion process of inorganic carbon into organic substances) was measured through oxygen concentration in the water. The maximum growth rate is $\mu_{max} = 0.0886$ for diatoms.

$$\mu_{light} = \mu_{max} \frac{I}{I_{opt}} e^{(1-\frac{I}{I_{opt}})} \frac{N_{V<1kn}}{N_{total}} \tag{3.16}$$

The dataset presented in Section 3.1 does not contain any information on light intensity I. The draft of the ship should also be included, as it influences the amount of light reaching the hull at different depths. For this reasons, a formulation able to consider the daily evolution of I and the variation of draft is created in Equation 3.17. This consists in a weighted average of the day and night light intensities.

$$I = \frac{I_{day}}{24} D_l + \frac{I_{night}}{24} (24 - D_l) \tag{3.17}$$

The day and night contributions, respectively I_{day} and I_{night}, are included through the daylength D_l from Forsythe's theory [66]. This involves revolution and sun's declination angles (θ in Equation 3.18 and ϕ in Equation 3.19). The dataset is therefore further modified to include the number corresponding to the day of the year J_d.

$$\theta = 0.2163108 + 2\ arctan[0.9671396\ tan(0.0086\ (J_d - 186))] \tag{3.18}$$

$$\phi = arcsin(0.39795\ cos\theta) \tag{3.19}$$

$$D_l = 24 - \frac{24}{\pi} arccos\left[\frac{sin\left(\frac{p\pi}{180}\right) + sin\left(\frac{L^\circ\pi}{180}\right) sin\phi}{cos\left(\frac{L^\circ\pi}{180}\right) cos\phi}\right] \tag{3.20}$$

The daylength formulation above also considers the latitude L° and the daylength coefficient p. Such a constant, equal in this case to zero, establishes that sunrise and sunset occur when the center of the sun is even with the horizon. Figure A.1 shows the length of day, expressed in hours, for a range of standard latitudes. Consequently, the specific case of the ship can be implemented through interpolation of available curves with the latitudes in Figure 3.3. The resulting hours of light throughout the whole time period are illustrated in Figure 3.7. It is interesting to notice how, especially from July 2013, the trend presents a double oscillatory behaviour: the low-amplitude oscillation is due to the alternating destinations of the ship, and the low-frequency, high-amplitude one is given instead by the cycle of seasons.

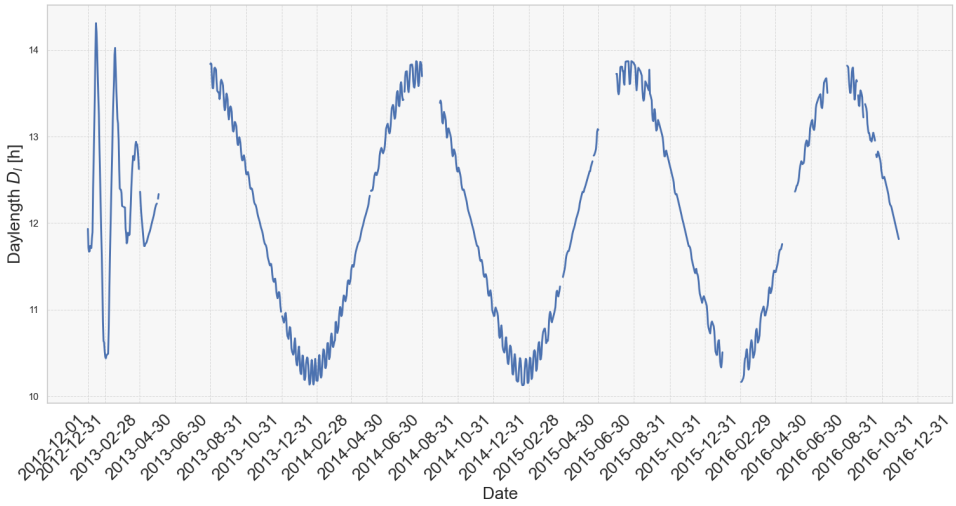

Figure 3.7: Daylength evolution at ship's latitude

While considering the light intensity that reaches a body submerged in water, four phenomena should be included: reflection, refraction, absorption and diffraction. The former two, both implying an intensity loss due to the air-water interface, are disregarded. Instead, the day-averaged light intensity perpendicular to the water surface I_0 at the ship's GPS position is implemented through the History Forecast Data [67]. The real impacting angle of sunrays will be considered only when scattering is a meaningful phenomena. The gathered information is plotted in Figure A.2, where the general trend reflects the seasonal cycle. Many of the scatter points deviate from such behaviour, but they are not considered as outliers since weather conditions are intrinsically ever-changing and not completely dependent on the season.

Absorption is described with Beer-Lambert law in Equation 2.14, which allows to include in day and night light intensities the effect of water depth and light dispersion through the attenuation rate $k = 0.21\ m^{-1}$. Such value is chosen from Kirk et al. [68], as it is connected to the most relevant light spectrum wavelengths for diatoms (average of blue and red light, $\lambda = 6000$ Å). Figure A.3 shows the time evolution for I_{day} and I_{night} for any point at the bilge ($z = T$ as in Figure 3.4). I_{night} is obtained through division of a factor 10^4 from I_{day} to adjust I_0 to night's radiation. The value stems from available online data. The daily biofouling diatomic light growth rate alone is presented in Figure 3.9. A trend line is added to aid the visualization of how the growth rate evolves, as well as to provide a prediction for the portions of missing dataset. The seasonality influence is downsized by the presence of null values, corresponding to full days of navigation.

The last of the previously mentioned phenomena, diffraction, is included only when evaluating the light reaching the bottom of the ship. This implies the redirection of a portion of light rays due to the water molecules. According to Fraunhofer's equation for far-field diffraction in Manakov et al. [69], such component can be calculated as:

$$I_{diffr} = I_{light}\left(\frac{sin\beta}{\beta}\right)^2 \qquad \beta = \frac{\pi a sin\theta_z}{\lambda} \tag{3.21}$$

with $a = 0.001\ m$ the width of a slit and θ_z the solar zenith angle (Equation 3.22) from Fatemi et al. [70]. This is dependent on latitude, declination angle ϕ in Equation 3.19 and hour angle H. The latter is however null for daily averaged values.

$$cos\theta_z = sinL^\circ\ sin\phi + cosL^\circ\ cos\phi \tag{3.22}$$

Figure 3.8 shows the resultant light intensity reaching bilge I_{light} and bottom I_{diffr}. The oscillatory trend due to seasonality is still present in the former, while it is not visible for the latter. As expected, the diffracted light is much lower than the other component, meaning that biofouling growth on the bottom is likely not influenced to a great extent by light.

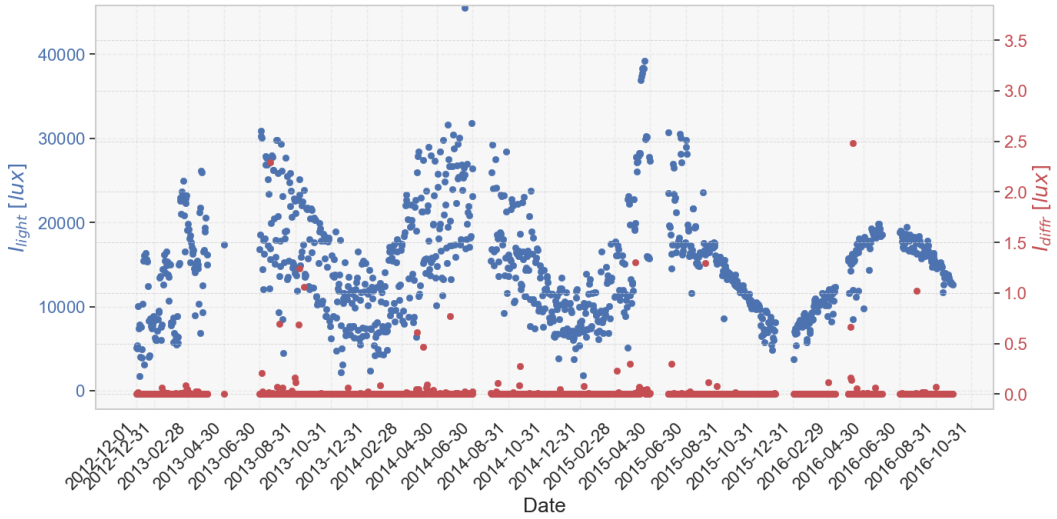

Figure 3.8: Light intensity reaching bilge I_{light} and bottom I_{diffr}, according to Equation 3.17

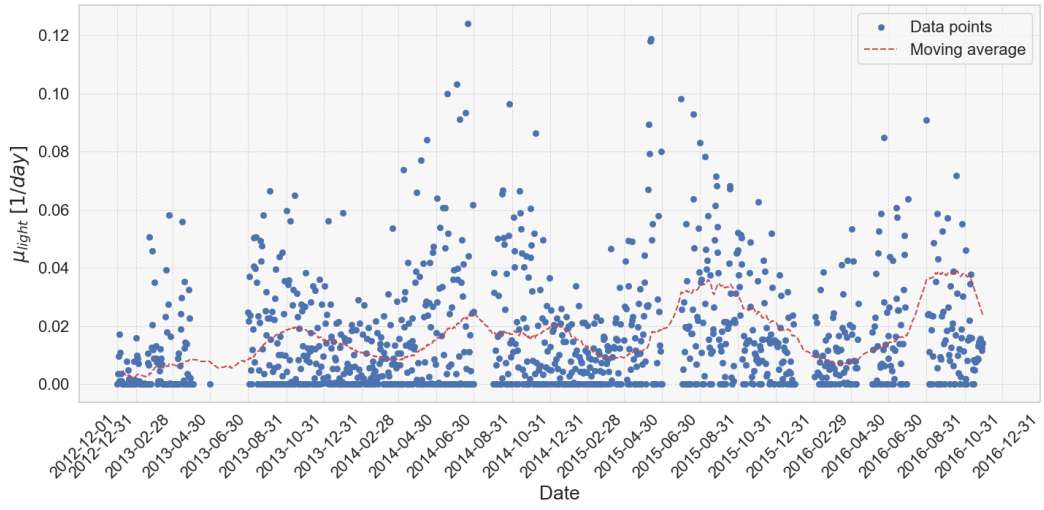

Figure 3.9: Growth rate due to light intensity μ_{light} at $z = T$

The growth rate due to light intensity at the ship's position is shown in Figure 3.9. The missing values have been filled with a moving average with a window of 100 data. The individual scatter points are however more widely spread throughout the graph. This is the influence of the speed contribute in Equation 3.16, flattening the points associated with ship sailing at $V > 1\ kn$ for greater portions of the entire day.

Temperature

Sea surface temperature is added to the dataset as already described in Section 3.1.2. Longitude is, to this extent only, disregarded because of evidence in the literature highlighting the modest impact it has on temperature variations. Figure A.4 shows the temperature time evolution for the analysed period. Such line is not continuous, but characterised by occasional blank portions deriving from missing GPS information. No attempt to simulate the behaviour on the lacking time-frames was made, as it would have required the development of a machine learning model, outside the scope of the project.

The calculation of the growth rate due to sea surface temperature alone, μ_{SST}, can be achieved through Equation 3.23. This stems from Bernard et al. [44] model in Equation 2.13, modified with the addition of the ratio between $N_{V<1kn}$ and N_{total}, used to consider the effect of speed. The characteristic maximum growth rate μ_{max}, and minimum, maximum, optimum temperatures (respectively SST_{min}, SST_{max}, SST_{opt}) vary depending on the species. Since from literature it is well known that diatoms represent one of the most important fouling groups, the above mentioned variables have values as reported in Table 3.7.

Table 3.7: Temperature characteristics for *Bentic diatoms*

μ_{max}	$8.86 \cdot 10^{-2}$	$1/day$
SST_{max}	38.2	$°C$
SST_{min}	0	$°C$
SST_{opt}	25.3	$°C$

$$\mu_{temp} = \frac{(SST - SST_{max})\,(SST - SST_{min})^2\,(SST_{opt} - SST_{min})^{-1}\,\frac{N_{V<1kn}}{N_{total}}}{(SST_{opt} - SST_{min})\,(SST - SST_{opt}) - (SST_{opt} - SST_{max})\,(SST_{opt} + SST_{min} - 2SST)} \tag{3.23}$$

Figure 3.10 shows the daily growth rate of biofilm due to temperature's influence. Once again, a rolling average line is generated from the scattered data to provide a better visualization of how μ_{SST} evolves through time. This uses a window of 100 data points.

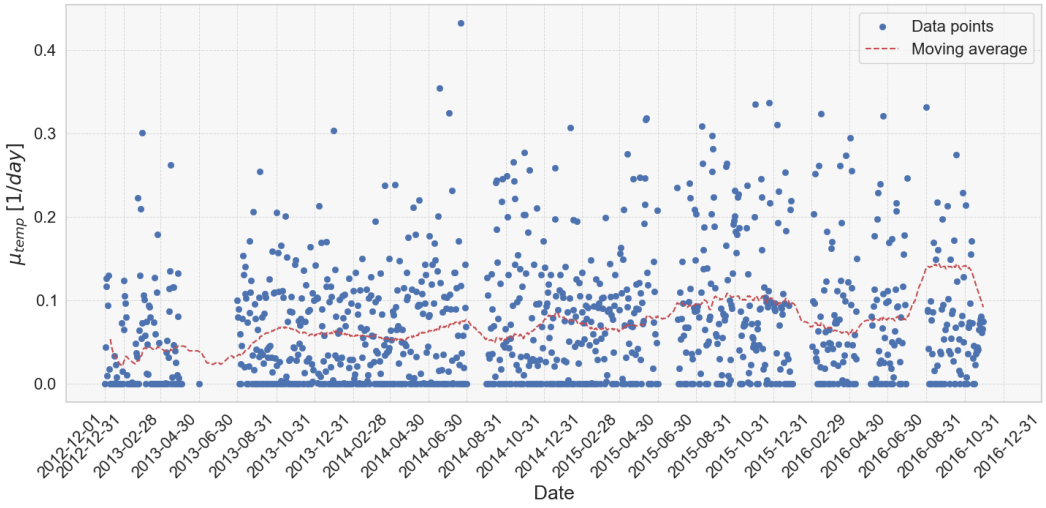

Figure 3.10: Growth rate due to Sea Surface Temperature μ_{temp}

Concentration of nutrients

Nitrogen, cobalt and iron are all reckoned as important elements for biofouling growth. Only phosphorous concentration P in the water will however be considered for the project. The concentration of phosphate PO_4 is implemented in the dataset using the Copernicus Marine tool [65]. Similarly to what done for light and temperature, a model from the literature is adopted and modified to include the effect of speed. In this case, Equation 2.16 by Martinez et al. [46] is chosen. This allows to include the inhibition of the substrate due to lack of nutrients.

$$\mu_{nutr} = \frac{\mu_{m1} K_i P + \mu_{m2} P^2 + \mu_{m3} K_S K_i}{K_S K_i + K_i P + P^2} \frac{N_{V<1kn}}{N_{total}} \tag{3.24}$$

K_i and K_S are normally dependent on water temperature. However, it is in this case decided to not include such aspect, but instead to take a constant value for both characteristics. This is done in order to avoid inter-correlations between the three main variables (light intensity, temperature and nutrients). Such an approach leads to the benefit of having a more clear separation of the different effects influencing biofouling growth, especially for what will be explained in Section 3.3.3. Table 3.8 shows the nutrient-related constants for the *Scenedesmus obliquus* species, a type of diatom.

Table 3.8: Phosphorous characteristics for *Scenedesmus obliquus*

μ_{m1}	$4.38 \cdot 10^{-2}$	$1/day$
μ_{m2}	$2.19 \cdot 10^{-2}$	$1/day$
μ_{m3}	$2.55 \cdot 10^{-2}$	$1/day$
K_i	10.5	μM
K_S	1.33	μM

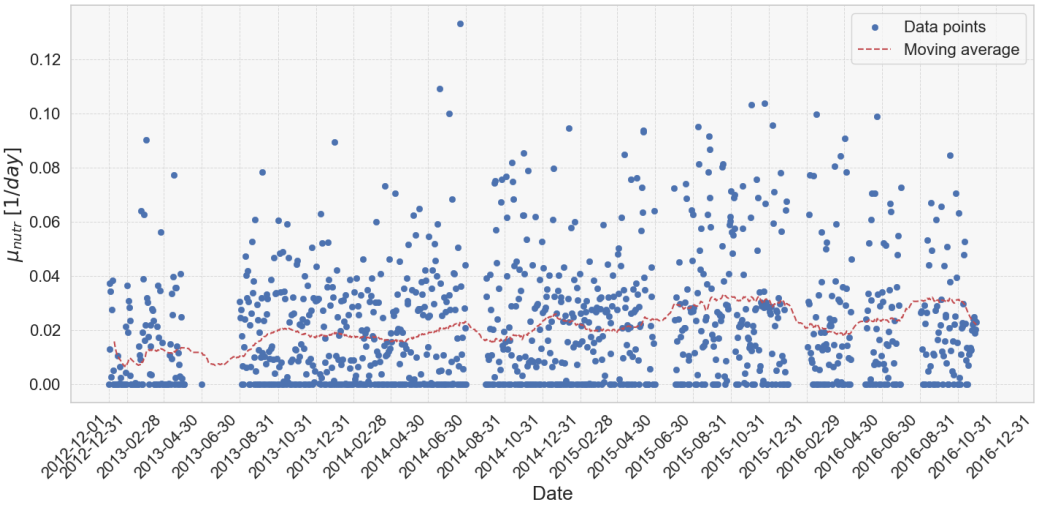

Figure 3.11: Growth rate due to phosphorous concentration μ_{nutr}

The seasonal oscillatory behaviour for the water-dissolved phosphorous concentration P in Figure A.5, input for the growth rate model, is not reflected in Figure 3.11. Differently from light intensity, the model by Martinez et al. [46] considers the daily growth as a combination of three partial μ. These heavily modify the scatter. The moving average considers 100 data points in its window.

3.3.3. Total growth rate & Equivalent sand-grain roughness height

As already highlighted in Section 2.2.1, there is no model in the literature that allows to consider simultaneously the impact of different variables on the growth rate of foulers. It follows that the combination of the analysed characteristics will be done in a simplified way, as there are no available tools to evaluate with more precision the effective growth. Considering that colour has been disregarded for lack of data, a linear superposition is used to combine the effect of light intensity, temperature and nutrients together. Speed, time, latitude and water depth are also implicitly included inside any of the characteristics.

$$\mu(t, SST, I, z, V, P, L^{\circ}) = c_l\ \mu_{light}(t, I, z, V, L^{\circ}) + c_t\ \mu_{temp}(t, SST, V, L^{\circ}) + c_n\ \mu_{nutr}(t, P, L^{\circ}) \quad (3.25)$$

The growth rate μ does not provide any information on the current state of the surface as far as roughness is concerned. It is therefore connected to the equivalent sand-grain roughness height k_s. To do so, the formulation from Uzun et al. [42] for Fouling Rating as reported in Equation 2.19 is used. This can be adapted to the growth rate, as they both indicate the variation in time of fouling presence on the surface. Equation 3.26 correlates the two variables. This states that the total Fouling Rating is given by the discrete summation of the daily growth rate superposition values μ_i, at a given time t_i.

$$\left(\frac{\partial FR}{\partial t}\right)_i \approx \mu_i \quad \rightarrow \quad FR_{tot} = \sum_{i=0}^{n} \mu_i t_i \quad (3.26)$$

The k_s model by Uzun et al. [42] can also be used. This is connected to the most prominent attempt in the literature of developing a comprehensive growth model, and it allows to take into account the inherent roughness of the coating $k_{coating}$. An additional condition is however implemented for clarity: according to Schultz [71], roughness values higher than $k_s = 300\ \mu m$ can be associated with the combined presence of heavy slime and calcareous organisms, outside the scope of the project. This corresponds to a Fouling Rating of 20. Equation 3.27 shows the final formulation for the equivalent sand-grain roughness height. FR_{tot} is directly implemented in the equation, despite the apparent difference in measurement units (FR_{tot} non-dimensional and k_s $[\mu m]$). The dimensional coherence is however guaranteed by the constants appearing in the equation. These have been obtained in the original paper by fitting the regression deriving from experimental data.

$$k_s(t) = \begin{cases} k_{coating} & FR_{tot} = 0 \\ 0.007143\ FR_{tot}^2 + 13.36\ FR_{tot} + k_{coating} & 0 < FR_{tot} \leq 20,\ k_s \leq 300 \\ hard\ fouling & k_s > 300 \end{cases} \quad (3.27)$$

The determination of the constants c_i in Equation 3.25 should be discussed. In general, these elements allow to provide an indication of what is the importance of each variable contributing towards the total growth rate. However, there is no available information for the containership, as far as drydocks and status of the hull at that time are concerned. This implies that obtaining the values for the constants with precision, namely through a Monte Carlo simulation by randomly varying c_i, is not feasible. A possible approach consists in evaluating with Equation 3.27 the resultant k_s trend deriving from the non-superposed μ_{light}, μ_{temp} and μ_{nutr} separately. The values obtained for the no-drydock scenario on the last useful day of the dataset (September 29th 2016) are then compared to obtain their relative weight to the total k_s, direct sum of their contributes. While the resultant trends will be shown Section 5.2, Table 3.9 provides the final k_s values for the single variables, as well as that of the constants. The results seem to confirm what stated in the literature about the great importance temperature has on growth, while light intensity has increasingly less influence the further the point on the hull is from the free surface (in this case $T = 0.3\ m$). The main disadvantage of this approach is that it assumes that the equations used to evaluate the environmental variables influence on growth are entirely independent from one another. This may however not be the case, since the formulations have been obtained by fitting outdoor experimental studies: the growth due to temperature thus contains non-measured information about nutrients, and vice-versa for the other ones. At the current state of research in the

subject, assuming the constants as indicated in the table would generate unreliable results. It is then preferred to have $c_l = c_t = c_n = 0.333$. This way, the importance of each environmental factor is directly provided by the values of the correlated growth rate, and the superposition is normalized.

Table 3.9: Tentative values of k_s and c_i for the single variables

Variable	c_i	k_s
Light intensity	0.380	950.1
Sea Surface Temperature	0.469	1183
Phosphorous concentration	0.151	368.1

Equation 3.27 provides an indication of how the equivalent sand-grain roughness height grows through time. However, it does not include any information about drydock operations. These are manually inserted in the graph by resetting k_s to the value of coating roughness. It is then assumed that during drydock the hull is repainted with the same coating. As previously mentioned, no information on the maintenance schedule of the ship is available. To provide a general indication of a more feasible behaviour of surface roughness, the following approach is followed. In particular, latitude and longitude of the ship, gathered through the GPS, are analysed to check what its position is. If these variables do not vary more than $0.1°$ (to account for sensors uncertainty) on consecutive days, then the ship is not moving. This is an accurate assumption despite only considering the average of all daily measurements, since the vessel operates among harbours that require more than one full day of navigation to be reached. If the ship appears to be still for 10 or more days, then it is safe to say that a hull cleaning was carried out. The choice of such period stems from the characteristics of the containership, and of the areas of the world where it operates. For example, the type of equipment, facilities availability and expected waiting times of the harbour should be considered. Since the vessel mainly operated in the Gulf of Guinea and in the Persian Gulf, where oil is extracted and the need for tankers is generally higher, the waiting time for the container pier should not be excessive. For the same reason however, the equipment may not be suitable to provide quick loading/unloading operations. Provided that the maximum capacity of the containership in object is relatively low ($C \approx 2000$), it is reasonable to assume that the operations will not take more than 2 full days to be completed.

Given the line of reasoning above elucubrated, three possible periods of drydock are found. These are indicated in Table 3.10, together with the corresponding GPS location. In two of the three locations, a drydock/floating dock is present. This means that the hull cleaning operations are indeed possible, and the likelihood of the still time being a scheduled maintenance is higher. Al-Jahra does not have any facility that allows such activities. An unforeseen event, like the failure of a vital component of the ship (either structural or mechanical), is thus the most probable cause of no navigation. It would also not be reasonable to have another drydock so close to the previous (4 months apart). Such unpredictable events may still be the main motivation for the other two periods as well, but it is here assumed that this is not case.

Table 3.10: Possible drydock periods and location

Period	Latitude [°]	Longitude [°]	Location	Drydock?
2015-04-07 $\rightarrow$ 2015-04-19	$25.15\ N$	$55.16\ E$	Dubai, UAE	Yes
2015-08-27 $\rightarrow$ 2015-09-05	$29.21\ N$	$47.55\ E$	Al-Jahra, Kuwait	No
2016-09-17 $\rightarrow$ 2016-09-28	$29.35\ N$	$47.92\ E$	Madinat al-Kuwait, Kuwait	Yes

3.4. CFD Simulations - ReFRESCO

The solver used for Computational Fluid Dynamics is ReFRESCO [72]. It is a CFD software package, developed at the Maritime Research Institute Netherlands (MARIN) in collaboration with several universities and partners. It solves unsteady (in)compressible viscous flows based on the Navier-Stokes equations, complemented with turbulence models and volume-fraction transport equations for different phases. The equations are discretized using a finite-volume approach of the continuity and momentum equations, reported respectively in Equation 3.28 and 3.29. Here, $\bar{u}_i$ is the averaged velocity vector, $\rho\overline{u_i' u_j'}$ the Reynolds stress, $\bar{p}$ the averaged pressure, and $\bar{\tau_{ij}}$ the mean viscous stress tensor components.

$$\frac{\partial\left(\rho\bar{u}_i\right)}{\partial x_i} = 0 \tag{3.28}$$

$$\frac{\partial\left(\rho\bar{u}_i\right)}{\partial t} + \frac{\partial}{\partial x_j}\left(\rho\bar{u}_i\bar{u}_j + \rho\overline{u_i' u_j'}\right) = -\frac{\partial\bar{p}}{\partial x_i} + \frac{\partial\bar{\tau}_{ij}}{\partial x_j} \qquad \bar{\tau}_{ij} = \mu\left(\frac{\partial\bar{u}_i}{\partial x_j} + \frac{\partial\bar{u}_j}{\partial x_i}\right) \tag{3.29}$$

For both the flat plate and full-scale containership cases that will be later explained, the Reynolds number based on the significant wetted length characterises a fully turbulent flow. The most widely applied turbulence model is the $k-\omega$ model: it uses a transport equation for the turbulent kinetic energy k, and one for the specific dissipation rate ω. An alternative is given by $k-\epsilon$, more indicated for simulations where the boundary layer characteristics are not the most important features. For the simulations that will be carried out, the Shear Stress Transport SST $k-\omega$ equations will be exploited. This hybrid approach combines the two models above explained, using $k-\omega$ in the near-wall region and $k-\epsilon$ in the free stream [58].

ReFRESCO uses a collocated, cell-centred variable arrangement and a face-based approach. This enables the use of unstructured, body-fitted computational meshes with arbitrary polyhedral cells. Picard linearization is applied, and segregated or coupled approaches are available with mass conservation. This is ensured by using a SIMPLE-like algorithm [73] and an pressure-weighted interpolation technique to avoid spurious oscillations [74]. Mesh handling techniques such as moving, sliding, deforming and overset meshes are available, as well as automatic mesh refinement and coarsening. The 6 DoF rigid-body motion is being solved within the code, and full fluid-structure interaction (FSI) with flexible-body motion is also possible. Lastly, coupling to external codes is made possible for propeller models (RANS-BEM coupling), fast-time simulation tools (MARIN's time-domain simulation framework XMF), and wave generation potential flow codes (OceanWave3D, SWASH, REEF3D). ReFRESCO is continuously being developed, verified and validated for maritime applications.

This section presents the methodology followed for the production of the results relative to flat plate and full-scale containership simulations. It includes a description of the case study, domain characteristics and boundary conditions, grid generation, and main settings chosen in the simulations setup.

3.4.1. Flat Plate

A flat plate of unit length and height L is here considered. Nine geometrically similar multi-block structured grids are considered. These are not self-produced but gathered from Tecnico Lisboa - Universidad de Lisboa [75]. Structured grids have their points arranged in a regular pattern that can be described through a indexing system, with each having a consistent number of neighbours. This kind of mesh has the benefit of being computationally efficient, but it does not allow for a great geometric flexibility. In the far-field they then still need a great number of points. This implies that structured meshes are best for domains with simple geometries, such as flat plates. The main characteristics of the grids are enumerated in Table 3.11. It is possible to notice how the finest grids have a smaller refinement ratio between each other in comparison to the coarsest ones. It can therefore be expected that the results will present greater variations between meshes 6, 7, 8 and 9.

Table 3.11: Grids characteristics for flat plate [75]

Grid	$N_{cells} \times 10^6$	N_{plate}	$r_i = N_{plate,1}/N_{plate,i}$
1	2.048	2560	1.00
2	1.311	2048	1.25
3	1.003	1792	1.43
4	0.800	1600	1.60
5	0.512	1280	2.00
6	0.327	1024	2.50
7	0.251	896	2.86
8	0.200	800	3.20
9	0.128	640	4.00

The flat plate is completely submerged in water and subjected to a seawater flow aligned with the plate at a velocity $V = 20.5\ kn$ ($Re = 1.75 \cdot 10^9$). There is no need for modelling the free surface modification, and the Reynolds Averaged Navier Stokes (RANS) method is sufficient. A range of k_s values are input so as to appreciate the flow modification and the consequent drag characteristics. The inflow velocity is set to $1\ m/s$ for the simulations, while the kinematic viscosity of seawater at $15°C$ is decreased to $\nu = 9.52 \cdot 10^{-8}\ m^2/s$. This allows to run the simulations at the Reynolds number above mentioned, without having to modify the characteristic length L of the domain. The study is carried out through wall-resolved simulations. This means that the flow near the flat plate is resolved directly by the grid, and it does not rely on already existing empirical models such as wall functions. As a consequence, the grid must be fine enough to evaluate the characteristics of the flow with reliable accuracy. Since the geometry is simple and the domain is small, applying wall-resolved methods does not imply great computational costs. It brings then to the advantage of having higher accuracy. Comparing with the grids for the containership in Table 3.14, the order of magnitude of the cells number between the two studied cases is the same. That is even though the domain of the flat plate is significantly smaller. The reason for this is given by the use of structured grids and wall-resolved method for the flat plate, bringing to the need for a generally finer refinement.

The study of the flow over the flat plate is meant to provide a general understanding of how the frictional characteristics of the object change with respect to the surface roughness. This can be considered as an idealized scenario, because of the simple geometry and the completely submerged surface.

Domain & Boundary Conditions

The calculation of the flow over the flat plate is carried out through a hexahedric domain of length $1.5L$, width $0.25L$ and height L. The origin of the coordinate system is positioned at the leading edge of the plate, with the x axis aligned with the object. The inlet is thus located at $x = -0.25L$ and the outlet at $x = 1.25L$. Figure 3.12 shows the domain above described. It is also possible to notice how the leading and trailing edges of the computational domain have a higher refinement. At the leading edge the flow transitions from free-stream condition to boundary layer, that starts forming and developing along the surface of the plate. At the trailing edge, the boundary layer detaches from the plate, causing flow separation and wake formation. A finer grid helps resolving velocity gradients and pressure variations in the flow for both portions of the domain.

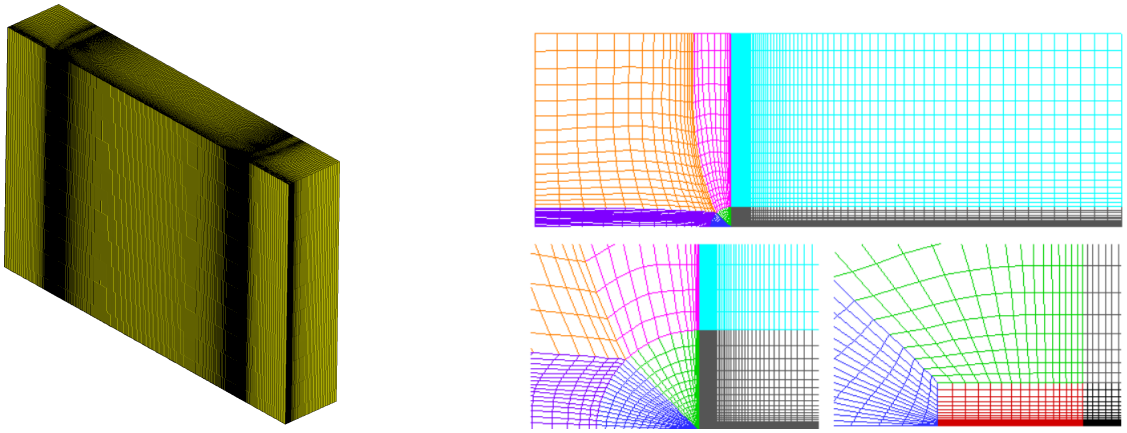

Figure 3.12: On the left the computational domain, on the right the leading edge refinement detail [75]

Each of the boundaries of the computational domain need to be associated with a condition. These should reflect the physical conditions of the simulated case, while providing a stable solution to the flow equations. Table 3.12 shows the boundary conditions chosen for the domain. The Inlet surface is associated with an Inflow condition to generate the uniform flow $V = (1, 0, 0)$, while the Outlet with the Outflow one. The External surface of the domain is provided with the Pressure condition: this allows to input null pressure at the surface, and to have the derivatives of all other variables in the y direction equal to zero. The SymmetryPlane condition is used for the two portions of surface positioned at $y = 0$, as well as for top and bottom (FreeSlip) of the box. For this kind of simulation setup, that is equivalent to imposing a slip wall condition, as they both enforce no normal velocity and shear stress adjacent to the boundary. This is also confirmed in Section 2.2 via Table 2.3 and 2.4. Finally, the flat plate itself is correlated with a Wall condition and roughness model by Wilcox, which enables the evaluation of the surface roughness effect on the drag of the plate.

Table 3.12: Boundary conditions for the flat plate

Surface	Boundary condition	Distance from origin
Inlet	Inflow	0.25L
Outlet	Outflow	1.25L
Flat plate	No-slip wall	-
External	Pressure	0.25L
Symmetry	Symmetry Plane	-
Top	Symmetry Plane	L
Bottom	Symmetry Plane	0

3.4.2. Full-scale containership

Full-scale simulations on the containership are carried out to evaluate what is the influence of surface roughness on both frictional and wave resistance. This section contains a description of the main steps followed to obtain the desired results, as well as of the simulation settings.

Geometry & Boundary Conditions

The containership geometry needs to be prepared and modified to guarantee the possibility of further refining the mesh where needed. It is of uttermost importance to subdivide the hull at locations that present a critical change in surface development. This is the case for the fore and aft edges of the cylindrical body, named respectively fore and aft shoulder, and for the bow of the ship. The areas close to bulb and transom are be separated from the rest of the ship to later increase their number of cells. This is needed, since they correspond with the zones where the water flow enters (leading edge) and exits (trailing edge) the ship. Figure 3.13 shows the end result for the bare hull geometry. No appendices are present and the propeller is disregarded.

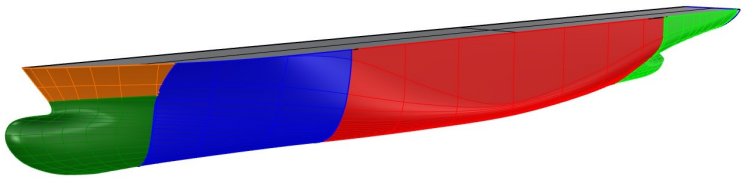

Figure 3.13: Subdivided bare hull geometry

The domain and boundary conditions are chosen to represent the containership as floating at design draft T in an ocean of infinite depth, and with a still water free-surface. Figure 3.14 provides a visual representation of the computation domain. Table 3.13 shows the boundary conditions chosen for each of the surfaces, and their distance from the origin of the left-handed reference system. This sees the x-axis directed towards the bow of the ship and the y-axis facing port side. The origin is positioned in the symmetry plane, at the aft perpendicular and at the waterline distant T from the keel line. Only half ship is considered to reduce the required cell number and halve the computational effort, since it does not significantly affect the computation. The distances of the boundaries are chosen to fulfill the following requirements: the bottom is deep enough to avoid shallow water effects, the left side position allows the Kelvin wedge to exit the domain at the outlet, and there is some transversal wave length astern of the ship [72].

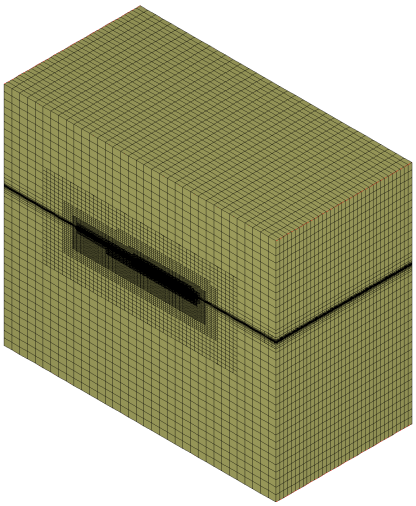

Figure 3.14: Overview of computational domain

Table 3.13: Boundaries and associated conditions

Surface	BC	Distance from origin
Inlet	Inflow	3L
Outlet	Outflow	3L
Bottom	Pressure	3L
Top	Pressure	2L
Left	Pressure	3L
Symmetry	Symmetry	-
Ship	No-slip wall	-

Mesh generation

A set of unstructured grids is generated using Hexpress: a grid generation package for non-conformal body-fitted full hexahedral unstructured meshes on complex arbitrary geometries [72]. Unlike structured meshes, the unstructured type is not identified by a regular connectivity and can assume triangular, quadrilateral and polygonal shape. The main advantage deriving from it, is the possibility to accommodate complex and arbitrary geometries, generating anisotropic meshes. This is particularly beneficial for free-surface simulations, as they allow to capture the water level, while keeping the cell count relatively low. Hexpress follows the volume-to-surface approach. This implies that the mesh generation starts from the domain volume, and it is later adapted to the geometry [76].

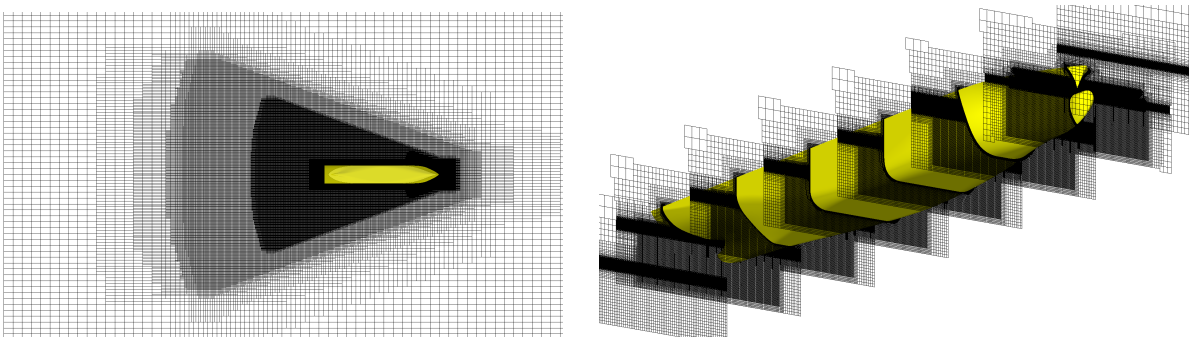

(a) (b)

Figure 3.15: Refinement a) at the free surface and b) transversely along the hull

Different refinement levels are chosen for the surfaces depending on their shape and position along the hull. For example, a low refinement number is chosen for the transom, as it is not submerged at the given draft, and the simulation does not involve incoming waves. Variations in pressure distributions along the hull can however cause it to get partially under water. The midship cylindrical body of the ship is also coarser than the rest of the hull, as it does not present any sudden shape change. The water flow will not therefore undergo relevant changes in direction that needs to be captured. Prismatic refinements are added to the free surface around the ship to capture the effects of the developing boundary layer. Box refinements are added at the bow and stern, where pressure gradients and flow detachment occur. Figure 3.15 shows the free surface final refinement in bird view and along the hull.

Differently from the flat plate, the full-scale ship simulations are carried out through wall-modelled methods. Since the computational domain is large, and the ship geometry is complex at its bow and stern, using wall-resolved methods would require an extremely fine grid. The required computational effort deriving from this would result unfeasible for the timeline of the project, and unnecessarily precise for its scope. Wall-modelled methods are based on wall functions (see Section 2.2.2) that model the behaviour of the fluid without solving the viscous sub-layer. Such an approach is particularly beneficial for high Re simulations, for which finer grids would otherwise be necessary. The wall-function used to model surface roughness effects on the boundary layer is Apsley's, reported in Equation 2.21. Since the Reynolds number for any of the ship speeds considered is higher than the critical transition values, and the flow is fully turbulent, the model can be accurately used as it is more suitable for such condition.

Table 3.14: Grids characteristics for containership

Grid	$N_{cells} \cdot 10^6$	$r_i = \sqrt[3]{N_{cells,1}/N_{cells,i}}$
1	11.50	–
2	9.401	1.069
3	5.812	1.255

Table 3.14 reports the number of cells and refinement ratios for the different grids used in the simulations. Despite multiple roughness values and ship speeds are considered, only three meshes are employed, as it is first checked that the y^+ values are in a range that allows their application for the whole range of k_s and V. It must be highlighted that the grid convergence study is carried out for only a single value of the two above mentioned variables: this means that after evaluating the numerical uncertainty deriving from the mesh size, only the most suitable grid (compromise between results accuracy and computational effort) will be used for the remaining runs.

Simulation settings

Beside the boundary conditions of the domain, grid and wall roughness function already described, additional settings need to be defined in the input file before running the simulations. Namely, air and water properties for a temperature of $20°C$ are implemented, as they are needed to computationally solve the Navier-Stokes equations. Table 3.15 reports some of the settings and input values used in the simulations. Three input speeds are also considered: $20.5\ kn$ is the design speed, while $V = 14\ kn$ is the most common velocity at which the ship sailed. The lowest $V = 7\ kn$ is used to appreciate the wave resistance at low inflow speeds. The turbulence model is the $SST\ k-\omega$ by Menter [77] already mentioned at the beginning of this Section.

Table 3.15: Air and water characteristics

$\rho\ [kg/m^3]$	1025
$\nu\ [m^2/s]$	$1.22 \cdot 10^{-3}$
$\rho_a\ [kg/m^3]$	1.225
$\nu_a\ [m^2/s]$	$1.80 \cdot 10^{-5}$

Table 3.16: Reynolds and Froude numbers

Speed $V\ [kn]$	$Re \cdot 10^8$	Fr
7	4.470	0.046
14	7.200	0.066
20.5	13.1	0.261

Among the main goals of the project lies the evaluation of surface roughness influence on wave resistance. This means that the free surface at the design draft needs to be modelled accordingly. Beside the free surface refinement shown in Figure 3.15, unsteady simulations (URANS) need to be used to capture the water level and wave pattern modification. The timestep needs to be chosen so that the Courant-Friedrichs-Lewy (CFL) condition is respected. This states that a fluid particle should not travel a distance in one time step Δt that is larger than a grid cell Δx. Such a condition maintains the stability of the simulation, preventing numerical errors and guaranteeing physically meaningful results. Since the input flow velocity is $V = (u_x, u_y, u_z) = (V, 0, 0)$, the condition can be written as in Equation 3.30. To ensure that the condition is respected, $\Delta t = 0.01\ s$ is chosen for all grids, independently from their refinement level.

$$CFL = \Delta t \left| \frac{u_x}{\Delta x} + \frac{u_y}{\Delta y} + \frac{u_y}{\Delta y} \right| \leq 1 \quad \rightarrow \quad CFL = \frac{|u_x| \Delta t}{\Delta x} \leq 1 \tag{3.30}$$

No incoming waves are present, but the wave absorption zone should be defined to prevent wave reflections from the outer boundaries of the domain. This area needs to be accurately set to prevent the results from inaccuracies in wave pattern prediction and ship resistance. An inner and outer radii are necessary. The former $r_i = (1.5L_{pp}, L_{pp}, 100L_{pp})$ delineates the elliptic portion of the free surface where no absorption is applied. In the latter $r_o = (3L_{pp}, 2L_{pp}, 100L_{pp})$ absorption increases from zero at the boundary with the inner radius, to its maximum value of 50.

The kind of approach needed to model the motions of the ship should also be discussed. A complete 6-DoF dynamic free-motion equation is not needed, since it is possible to visualize the ship as towed in an infinitely deep ocean with no incoming waves. A quasi-static approach is thus chosen. This allows to consider the small variations in trim and sinkage (2-DoF motion equation) through grid deformation up to convergence, despite the fact that no initial displacements are present.

4

Verification

Computational fluid dynamics simulations are characterised by a certain degree of uncertainty, given by either errors committed while modelling the physical phenomena at hand, or by a grid that is not fine enough to capture the results with precision. Verification and validation are two fundamental processes that ensure the reliability and accuracy of a CFD simulation result. Verification checks that the numerical solution represents the governing equations and boundary conditions used, and it is typically associated with the answer to the question *"Are we solving the equations right?"*. On the other hand, validation guarantees that the mathematical model accurately represents the physical phenomena that are being simulated. This is associated with the question *"Are we solving the right equations?"*.

This chapter presents the procedure followed to verify the numerical results. This is carried out through a grid convergence study for the flat plate, and with the Grid Convergence Index integrated with Richardson extrapolation for the containership. Validation is not included, since no experimental data for the vessel is available.

4.1. Flat plate: Grid convergence study

To ensure the solutions that will be later presented are independent of the mesh size, a grid convergence study is performed. Differently from what discussed in Section 2.2.2, this will be carried out, for the flat plate only, by direct comparison of the results obtained for each of the meshes. The values of y^+ were checked to make sure that the wall-resolved settings are accurately solved and portrayed in the results. In particular, the dimensionless distance from the wall should be lower than 1 for all simulations. This ensures that the viscous effects in the near-wall mesh are captured, and that the values of shear stress, drag and pressure will be accurate. Both global and local variables are checked for convergence. The former provide information on how the overall solution behaves as the grid is further refined. They may not reveal issues in specific regions, that are instead captured by local quantities.

Figure 4.1 shows the x-direction global frictional resistance coefficient for the last iteration, for different roughness values and across the grids. The global drag does not vary significantly as the grid is progressively refined, implying that even the coarsest mesh is sufficiently precise to represent the viscous effects inside the domain. A greater dependence is noticed for the highest roughness $k_s = 300$, which suggests greater turbulence in the simulation that needs to be captured more accurately. For this, the finest grid (1) has a slightly different value from the others. The percentage variation in comparison to grids 2 and 3 is low enough to consider the results as independent from mesh size while using the finest mesh. This means that grid 1 can be used to generate further results, and it is expected that an even finer grid would produce same values.

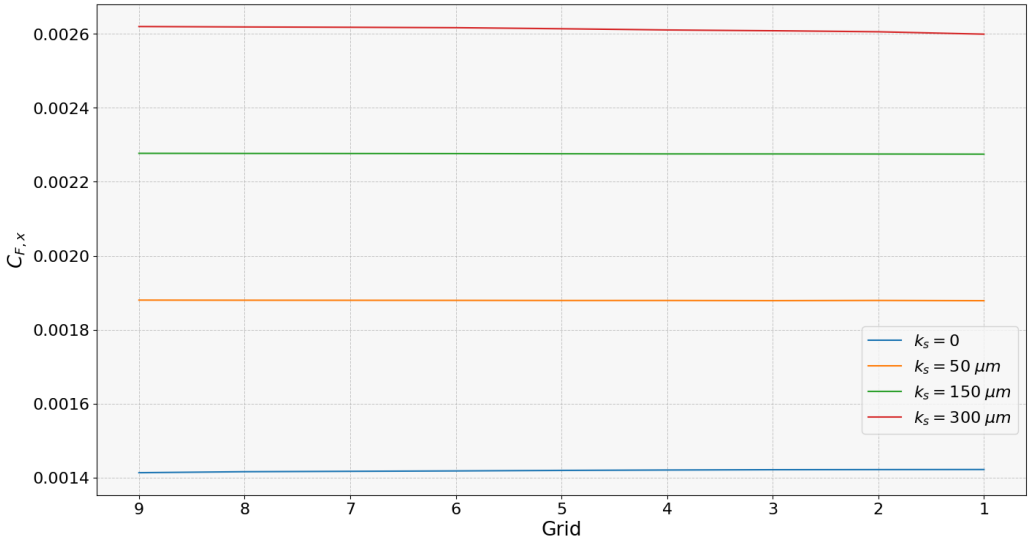

Figure 4.1: Converge study for x-direction total frictional force

The local convergence is evaluated in Figure 4.2, where the skin friction C_f is plotted against the non-dimensional position along the plate. Only the convergence for the highest equivalent sand-grain roughness height number is checked, since it resulted from Figure 4.1 being the more heavily grid-dependent scenario. Both trend and values of the local drag suggest that the solution is converging well with respect to the grid resolution. That is especially at the center and trailing edge of the plate, while the leading edge is characterised by greater differences due to the steep pressure gradients in that region. The effect of the wall-resolved approach can be visualized by the fact that the finest grids still possess a small variation in the results. The y^+ values are small enough to guarantee the accuracy of the obtained variables trends.

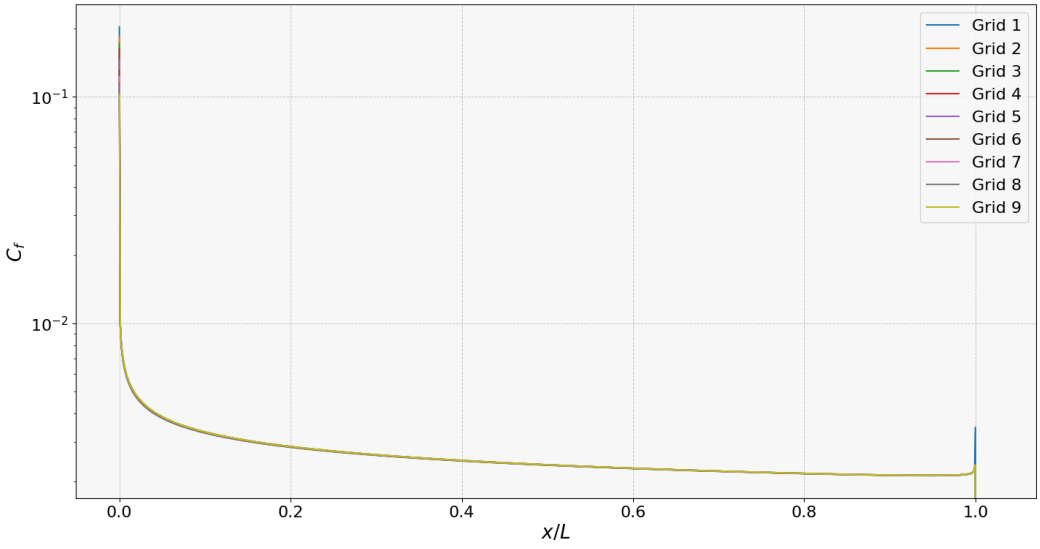

Figure 4.2: Local x-direction skin friction convergence study for $k_s = 300\ \mu m$

4.2. Full-scale containership: Grid Convergence Index

The independence from the grid resolution of the full-scale containership results is checked via the Grid Convergence Index, in conjunction with Richardson extrapolation. The followed procedure is the same indicated in Section 2.2.2. The refinement ratios between the grids are not $\sqrt{2}$ as it is normally done in the literature, but they have values as in Table 4.1. This means that the additional term reported in Equation 2.24 needs to be implemented. Table 4.2 shows the discretization error calculation for the spatial convergence study of the considered variables, obtained for $V = 14\ kn$ and $k_s = 300\ \mu m$. Only global variables are taken into consideration, as they are of primary importance for the project at hand.

Table 4.1: Number of cells and grid refinements

N_1	N_2	N_3	r_{21}	r_{32}
$11.5 \cdot 10^6$	$9.40 \cdot 10^6$	$5.81 \cdot 10^6$	0.935	0.852

Table 4.2: GCI analysis results

	$R_{F,x}\ [kN]$	$R_{press,x}\ [kN]$	$M_x\ [kNm]$	$H_{wave,max}\ [m]$ at hull
ϕ_1	-180510	-28763	$3.771 \cdot 10^8$	1.510
ϕ_2	-180517	-30890	$3.770 \cdot 10^8$	1.500
ϕ_3	-180066	-30670	$3.770 \cdot 10^8$	1.440
ϵ_{32}	$2.50 \cdot 10^{-3}$	$7.10 \cdot 10^{-3}$	0	0.040
ϵ_{21}	$4.00 \cdot 10^{-5}$	0.074	$2.70 \cdot 10^{-4}$	$6.62 \cdot 10^{-3}$
e_a^{21}	$4.00 \cdot 10^{-5}$	0.074	$2.70 \cdot 10^{-4}$	$6.62 \cdot 10^{-3}$
q	-2.360	0.100	0.090	-1.280
p_a	-26.85	32.48	1.000	-7.658
ϕ_{ext}^{21}	-180509	-31165	$3.77 \cdot 10^8$	1.525
e_{ext}^{21}	10^{-5}	0.077	$4.10 \cdot 10^{-3}$	$9.75 \cdot 10^{-3}$
GCI_{medium}^{32}	$4.00 \cdot 10^{-5}$	$-8.95 \cdot 10^{-3}$	0.021	0.021
GCI_{fine}^{21}	10^{-5}	-0.104	$-5.00 \cdot 10^{-3}$	0.012

The resulting GCI for the fine grid is small for all the investigated variables, with the highest being the one related to $R_{press,x}$. The grid is thus sufficiently fine, and the solution approaches the real value with a neglectable discretization error. The results are then independent of the grid, and further refinements will not alter them in a significant manner. The findings of the following chapter are obtained with the medium grid. This involves a low GCI for all variables, providing a good compromise between computational costs and accuracy. Given the values of the GCI_{medium}^{32} and GCI_{fine}^{32}, it can be concluded that all meshes are excessively fine for the needs of the simulations. This was however done on purpose for time-management reasons: generating a set of grids for each of the speeds would have increased heavily the overall computational effort. Higher grid refinements were then chosen during the generation of the domain mesh. This way, the grid convergence could be carried out for only the medium speed.

A wall-modelled approach is adopted, thus y^+ can assume a wider range of values with no implications on the simulations. A check on its maximum is however carried out: $y^+ > 1000$ would imply that the boundary layer effects are not accurately captured in some regions, leading to potential inaccuracies that do not show in the global values. In this case, $y^+_{1,max} = 191$, $y^+_{2,max} = 279$ and $y^+_{3,max} = 422$. The results will therefore not suffer from relevant numerical errors, as it is also confirmed by the GCI. Figure 4.3 shows the y^+ distribution on the hull with a surface roughness of $300\ \mu m$ and for the two

speeds considered. As already mentioned and expected, the values for $7\ kn$ are generally lower because of a smaller friction velocity acting on the hull, and the lower amidship grid refinement results to be suitable thanks to the flow conditions. At $V = 14\ \mu m$, the fore shoulder mesh could have been further refined to lower the value of the non-dimensional distance from the wall. Nonetheless, it is low enough to not create any relevant numerical uncertainty on the final results.

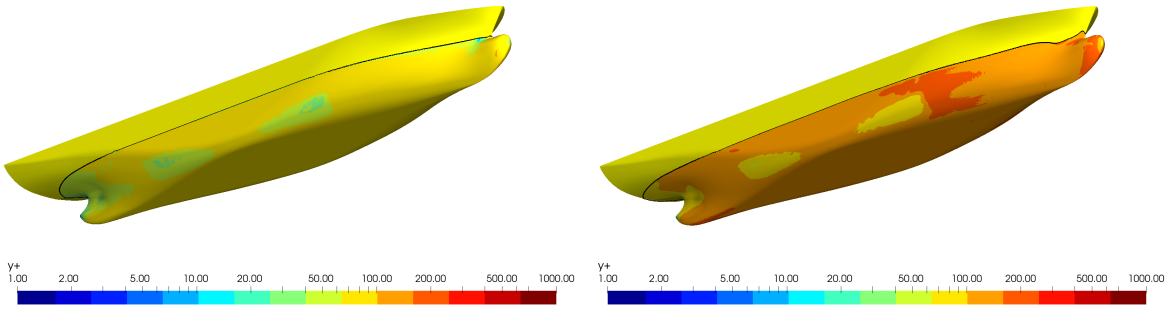

(a) $V = 7\ kn$ (b) $V = 14\ kn$

Figure 4.3: Resultant medium grid y^+ for $k_s = 300\ \mu m$ at (a) $7\ kn$, (b) $14\ kn$

Another characteristic that can be checked to ensure the quality of the results is the air volume fraction. This variable expresses the proportion of a computational cell that is occupied by air in a multi-phase flow simulation, where both air and water are present ($0 \rightarrow$ only water, $1 \rightarrow$ only air). This provides an indication of whether ventilation has occurred due to high speeds and wave interaction, that may cause air entrapment. Figure 4.4 shows the air volume fraction distribution on the hull. For both speeds, the areas above the waterline only contain air, ensuring the physical meaningfulness of the results. All portions under the waterline have maximum ratio of 0.08, which indicates that some air is trapped underwater. This is due to either poor mesh resolution of the air-water interface, or errors in the solution of the turbulence equation. Such values are still acceptable and expected for ReFRESCO simulations as suggested in the documentation [72]. The low speed simulations are characterised by less ventilation, since the entire bottom and bilge of the hull have a null fraction value. The highest speed instead has air that extends up to the external portions of the bottom.

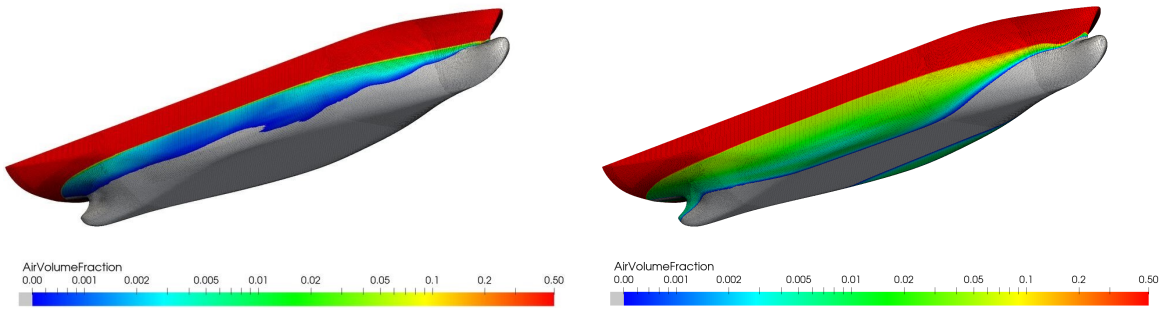

(a) $V = 7\ kn$ (b) $V = 14\ kn$

Figure 4.4: Resultant medium grid air fraction for $k_s = 300\ \mu m$ at (a) $7\ kn$, (b) $14\ kn$

5 Results

In Chapter 3 the methodology followed for the numerical simulations, analytical growth model and data processing was presented. In Chapter 4, the CFD verification procedures quantified the numerical errors of both flat plate and full-scale containership. The results for the three parts of the project can now be presented. First, the resistance evaluation trend from data processing will be analysed. Following that, the surface roughness and added frictional resistance prediction of the growth model will be discussed together with a sensitivity study. The numerical evidence for flat plate and ship will be given. Finally, the three parts will be combined together to evaluate whether the growth model accurately predicts the real growth or not.

5.1. Resistance from data processing

According to the procedure illustrated in Section 3.2, the added frictional resistance trend can be obtained. This helps understanding how biofouling influenced the containership throughout its operative life, and to identify possible maintenance operations. This is done only considering the days when the ship sailed at a speed of 14 kn, one of the most common velocities. The formulations used, as well as a portion of the results, are provided in Appendix C.

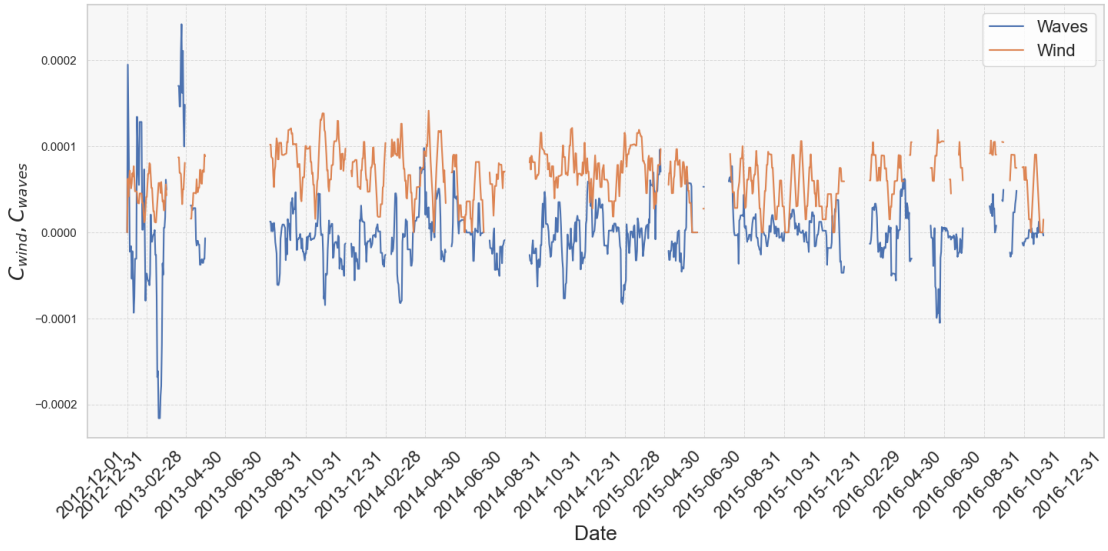

Figure 5.1: Wind and wave non-dimensional resistance coefficient (rolling average, window of 8 data)

Figure 5.1 shows the rolling average (8 measurements window) for the non-dimensional environmental resistance coefficients: wind and waves. Current is not shown, as it is already accounted for in the speed measurements. The negative values correspond to wind and waves acting on the stern of the hull, providing a small decrease in the total resistance. It is interesting to notice how the sailing location of the vessel is reflected into the wave resistance. In the first half year, up until April 2013, the ship navigated in the Gulf of Guinea and circumnavigated Africa multiple times. Ocean waves are characterised by a generally higher height if compared to enclosed waters. This implies greater resistance on the ship according to Equation 3.11.

The final added frictional resistance ΔC_F daily values, obtained according to Equation 3.12, are reported in Figure 5.2.Multiple negative daily values are present. These are not physically relevant, since they would imply a reduction in resistance due to roughness. The presence of these points is given by the great uncertainties, intrinsic to the followed procedure and to the measurement errors of input variables. For the current status of the scatter, an uncertainty of $|\Delta C_F| \approx 8 \cdot 10^{-4}$ can be observed (the extremely negative points are considered to be outliers). Despite the fact that a general trend can be recognized, the data is further filtered by taking out the negative values. This may help identifying the above mentioned maintenance periods.

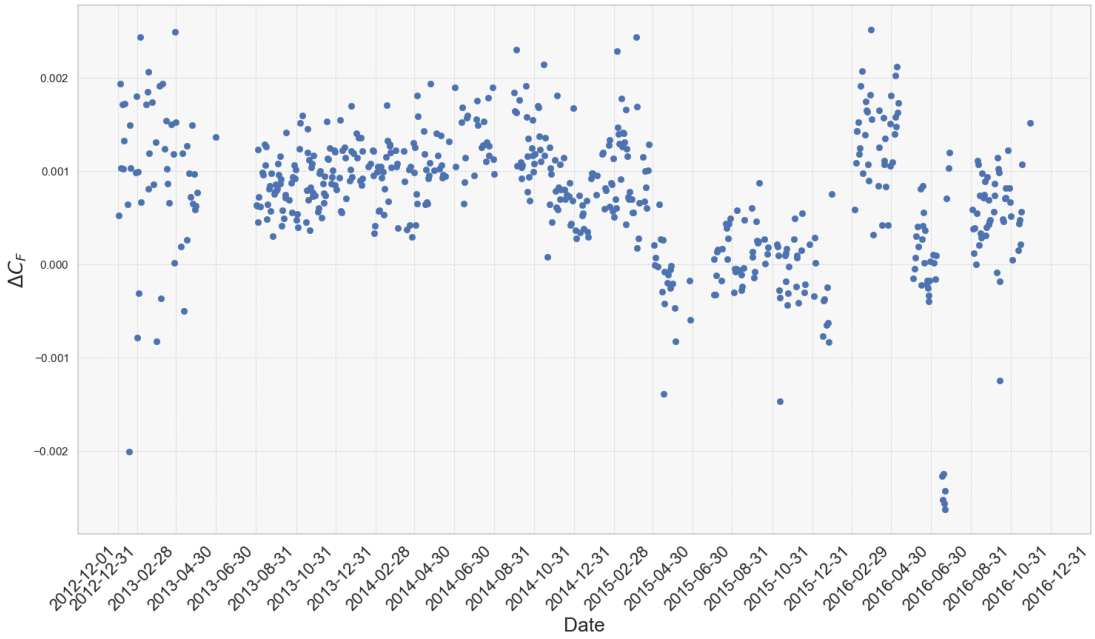

Figure 5.2: Added frictional resistance ΔC_F due to surface roughness, no filtering

Figure 5.3 shows the daily ΔC_F values, and the rolling average with a window of 80 scatter points. The frequency of each coefficient value is also reported to provide an indication on the entity of fouling. The trend is highly monotonically unstable, meaning that multiple oscillations are present. The small ones, occurring between a few consecutive days, are likely due to the uncertainty of wind and waves. It is also possible that a few of such drops are given by detachment of biofilm due to the water flow. Five relevant ΔC_F drops can be identified. Two of these fall into the periods indicated in Table 3.10: one at the beginning of April 2014, and the other in September 2016. The one at the end of the figure (October 2016) is possibly given by the lack of measurements. There is no information regarding the other two drops (February 2012 and August 2014). These may correspond to maintenance periods carried out directly in the water. They are however not included in the growth model, as there is no evidence of stationary ship by GPS position.

Exploiting Bowden's Equation 2.12 it is possible to evaluate the type of fouling the ship is mostly subjected to according to the literature. If $\Delta C_F \leq 6.36 \cdot 10^{-4}$, then soft fouling is dominant, otherwise up to $\Delta C_F = 1.27 \cdot 10^{-3}$ isolated barnacles are developing. Non-dimensional resistance coefficients higher than such value correspond to heavy calcareous fouling. From this, it stems that the ship sailed for 20.3% of the total time covered in soft fouling alone, 70.2% with isolated barnacles, and the remaining 9.45% with heavy calcareous fouling. This subdivision is purely theoretical, since it is proven by the literature that hard fouling grows on top of the biofilm. The great relevance of soft fouling is in any case highlighted. Figure 5.4 shows the requested power evolution for a constant speed of $13\ kn$, from Pozzi [78], for the same containership. This was obtained by analysing all the daily gathered measurements, and filtering out the outliers. Despite the different speed and variable, the general trends can still be compared as they are both related to a worsening in the ship performance. The moving averages have similar behaviour in the period August 2013 - March 2016. The power presents however a more steady and monotonic behaviour to be implied to the higher number of samples used in the average. It can be concluded that the followed methodology is sufficiently accurate to provide an overview of how the added frictional resistance trend varies in time. However, a more precise evaluation of this performance loss can only be obtained through machine learning strategies. Since this is outside the scope of the project, more information on the matter can be gathered from the associated thesis, in Pozzi [78].

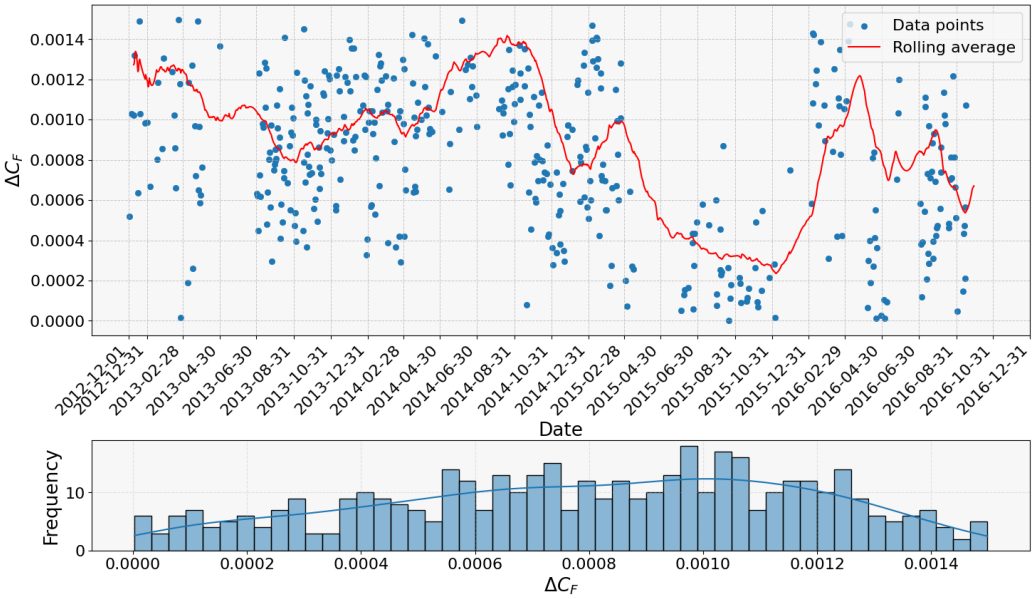

Figure 5.3: Added frictional resistance ΔC_F due to surface roughness, after filtering

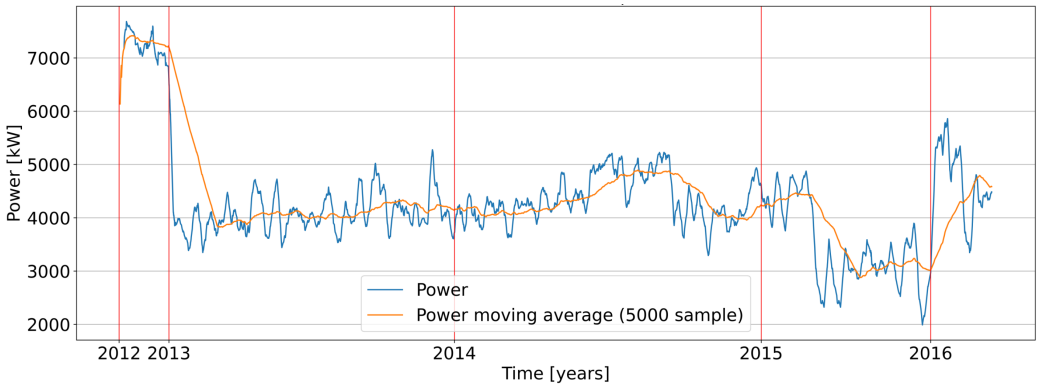

Figure 5.4: Power over time at a constant speed of $13\ kn$ [78]

5.2. Growth model

The results for the growth model are presented here. These are related to the superposition constants $c_l = c_t = c_n = 0.33$. After an evaluation of Fouling Rating, equivalent sand-grain roughness height, and the related added frictional resistance, a sensitivity study will be analysed to understand what is the uncertainty that derives from the choice of the superposition constants. Finally, the influence of draft on the final k_s trend will be discussed.

5.2.1. Equivalent sand-grain roughness height & Added frictional resistance

Figure 5.5 shows the growth rate μ for the superposed variables. The daily values are represented in the form of scatter points. A rolling average of 100 samples is used to indicate the general behaviour throughout the whole period. The seasonal changes, mostly deriving from nutrients and light intensity, are still present and oscillating around a mean value $\overline{\mu} = 0.036\ 1/day$. The amplitude of the variations is however dampened in comparison to the single variables. The average trend allows to estimate the missing measurements for the periods indicated in Table 3.5. The null values correspond to complete navigation days, due to how speed is considered in the model (see Section 3.3.2). This means that growth when the vessel is sailing is not included, nor investigated in this project. Future works should however address this aspect.

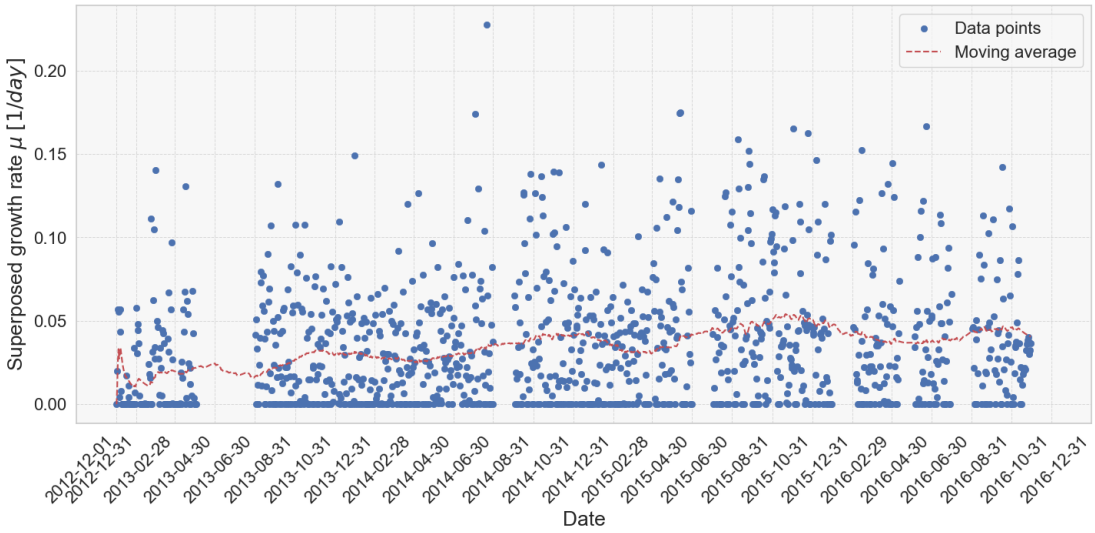

Figure 5.5: Growth rate superposition $\mu(SST,\ I,\ P)$

According to Equation 3.26, the Fouling Rating can be calculated using the superposed growth rate μ. The FR trend for both the no-drydock and drydock scenarios is shown in Figure 5.6. The latter is included by imposing a sudden decrease of the rating to 0, and a constant null trend for the periods listed in Table 3.10. The dotted parts of the lines represent the missing portions of the original dataset. These are implemented through the rolling average line from Figure 5.5 when needed. Their influence is a smoothing of the trend, which does not present sudden changes (100 samples are used). The rating limits from the literature for soft fouling and isolated barnacles, respectively $FR_{tot} = 20$ and $FR_{tot} = 70$, are also indicated. These provide an indication on when the biofilm is fully developed. This occurs respectively 694 and 472 days after the maintenance periods, assuming that the first day of the dataset (December 1st 2012) corresponds to the first day of operations after drydock. It is interesting to notice how the two drydocking periods are carried out in moments of the operative life of the vessel when the soft fouling limit was crossed, and the first isolated barnacles and non-shell foulers started to establish in the hull. If such maintenance operations were indeed done in the mentioned periods, then the profound detrimental effect of soft fouling on ship performance is highlighted. The uncertainty of when hull cleaning was operated also stems from the relative closeness between the two dates (17 months). This need can be partly justified by the areas where the ship sailed from 2014

onward, which are particularly prolific for biofouling growth. It must be reminded that the model only includes diatoms, and just some of the environmental variables influence growth. This can also be noticed on the no-drydock scenario, in which case the fouling rating for calcareous fouling $FR_{tot} > 70$ is not reached despite the analysed period of over 4 years.

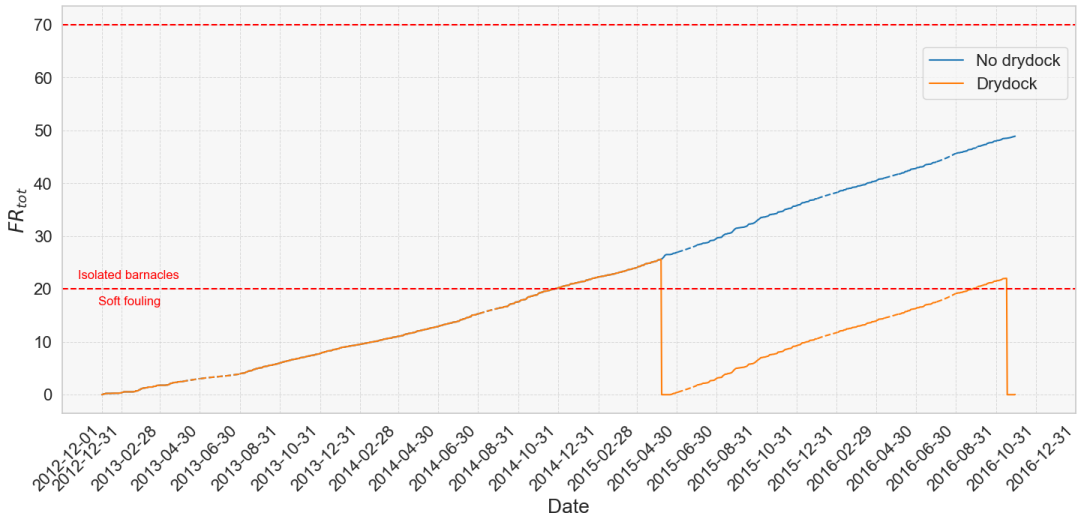

Figure 5.6: Total Fouling Rating FR_{tot}

Figure 5.7 shows the equivalent sand-grain roughness height k_s evolution through the considered time period. This is obtained from the Fouling Rating with Equation 3.27. Given the close relation of the two variables, similar considerations already discussed for FR also apply to k_s. The values for Fouling Rating and k_s corresponding to soft fouling limits (respectively 20 and 300) are here confirmed. This not only proves the equivalence between the values reported in the literature, but it also confirms that Equation 3.27 is suitable for evaluating surface roughness with the methodology proposed in the project. After the first 857 days, right before drydock, $k_s = 376.9\ \mu m$. When the vessel was sent to hull cleaning for the second time in September 2016, the surface roughness reached a value of $326\ \mu m$. If none of the maintenance operations would have been done, $k_s = 700.3\ \mu m$ at the end of the period.

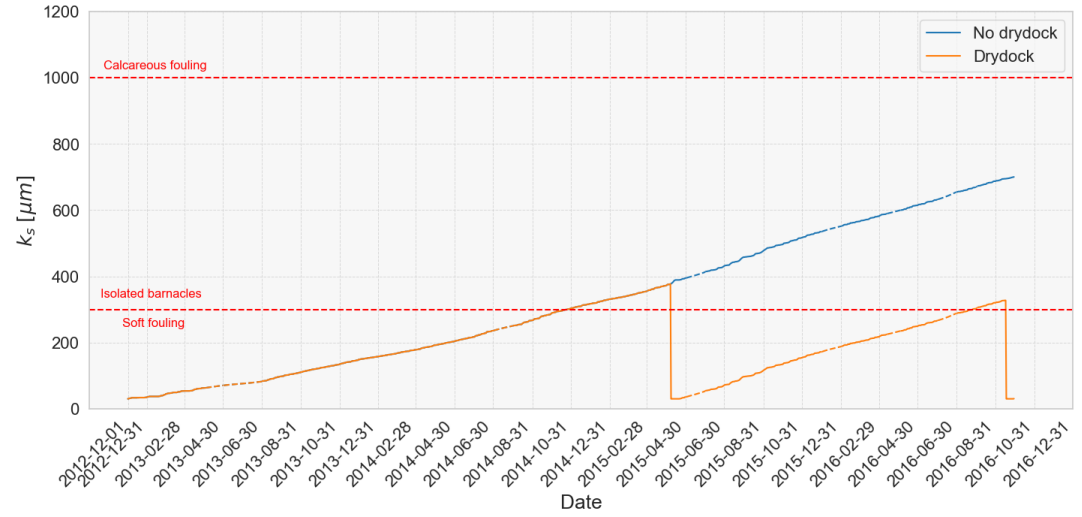

Figure 5.7: Equivalent sand-grain roughness height k_s time evolution

Finally, the added frictional resistance coefficient ΔC_F can be evaluated. This is done using Bowden equation from Section 2.1 and reported in Equation 5.1 to favour readability. This however gives negative increases (decrease) for the first weeks of the period, when k_s is still low. Such values are not physically meaningful, since increased roughness cannot generate a reduction on the skin friction on the hull. For this reason, negative values are corrected to $\Delta C_F = 0$, so that the remaining part of the trend is not influenced by the modification.

$$\Delta C_F = 0.001 \left[105 \sqrt[3]{\frac{k_s}{L_{wl}}} - 0.64 \right] \tag{5.1}$$

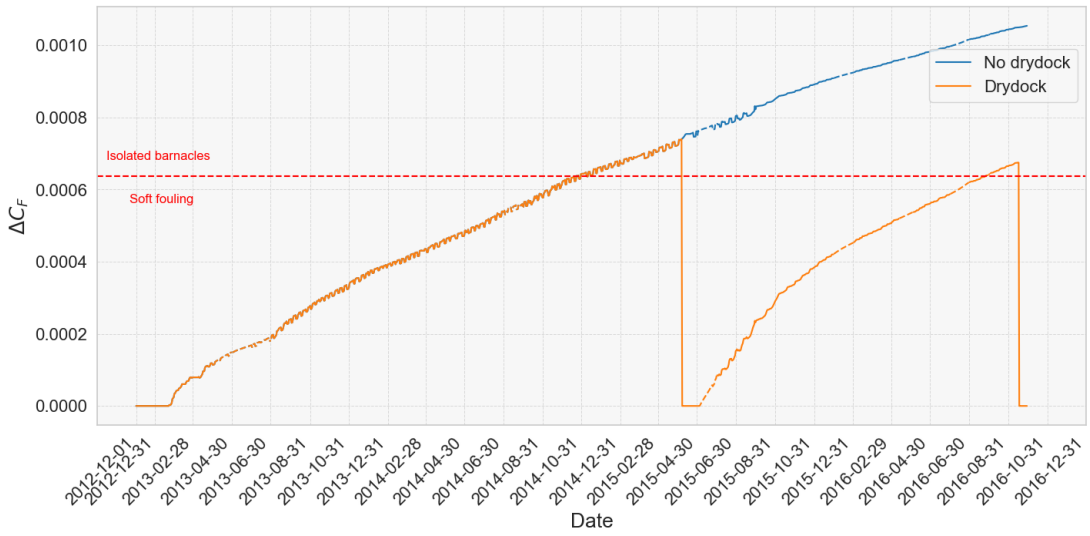

Figure 5.8: Added frictional resistance coefficient estimation ΔC_F

Figure 5.8 shows the mentioned trend for added frictional resistance, both if drydock periods are considered or not. The dotted portions represent once again the missing parts of the dataset, modelled using the average on Figure 5.5. The soft fouling limit is reached at the end of October 2014, and not on the same period as for FR and k_s, because of what explained on Equation 5.1. Before the first drydock, $\Delta C_F = 7.40 \cdot 10^{-4}$, while the added frictional resistance coefficient has reached a value of $6.75 \cdot 10^{-4}$ before the second maintenance. If the no-drydock scenario is considered, the coefficient increases up to $1.05 \cdot 10^{-3}$. The small oscillations in the behaviour are given by the modification of waterline length as reported in Equation 5.1, consequence of the varying operational draft. They represent only fictional decreases in ΔC_F. It is interesting to notice how the trend for ΔC_F after the first drydock is steeper than for the no-maintenance scenario during the same days. This is in agreement with the following CFD results, and with what agreed in the literature over the importance small surface roughness (i.e. soft fouling) has on the hydrodynamic performance.

A clear visualization of the direct influence of surface roughness on ship performance can be obtained by plotting the dimensional frictional resistance increase ΔR_F. This is obtained by multiplication of the non-dimensional coefficient ΔC_F with the wetted surface S and speed V of the ship, as reported in Equation 5.2.

$$\Delta R_F = \frac{1}{2} \rho S V^2 \Delta C_F \tag{5.2}$$

The rolling averages of ΔR_F for the drydock and no-drydock scenarios are shown in Figure 5.9. The drop at the start of the maintenance periods is not sudden because of the number of samples used to calculate the mean value (100). This is preferred to a scatter plot, that would represent more accurately the effective added resistance, but a less clear presentation of the effects of drydock. Despite the rolling average, the trend is not monotonic because draft and speed vary throughout the period: lower velocities produce less resistance according to their relation $R \propto V^2$, while a more submerged ship generates greater frictional resistance because of an increased wetted area. The peak resistance $\Delta R_F = 62\ kN$ for the drydock scenario is reached on October 2014. After that, a decrease lasting until the first maintenance period can be seen: at such time, the cruising speed of the vessel was significantly lowered for operational needs, causing an apparent reduction in the added resistance with an average of $50\ kN$. If no drydock is considered, then the maximum value is obtained at the end of 2015 with 94 additional kN to the total resistance.

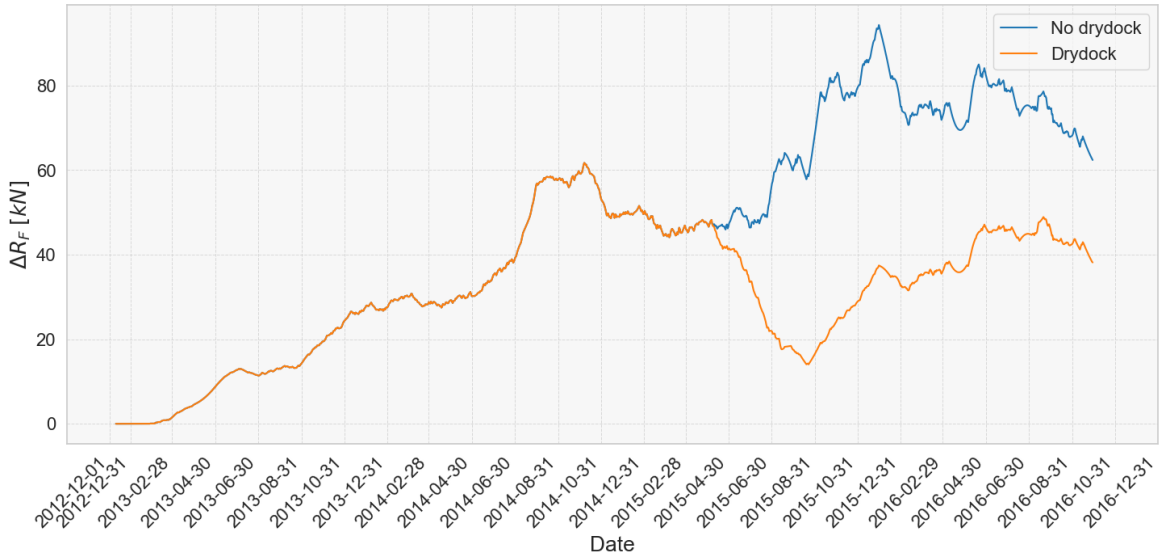

Figure 5.9: Mean added frictional resistance ΔR_F for the operative conditions of the ship

5.2.2. Fuel, emissions and expended capital

A quantification of the monetary and environmental consequences of biofouling can also be given. No information on the type of fuel used by the engine is given. Since the ship was built in 2010, when many of the regulations regarding air polluting emissions were already enforced, it is assumed that Marine Gas Oil (MGO) is employed. This represents a cleaner option in comparison to Heavy Fuel Oil. A total efficiency $\eta_{tot} = 0.7$ (mean value from Figure 3.5) and a Specific Fuel Consumption $SFC = 220 g/kWh$ from the Shop trial reports are also assumed: considering it as a constant is an approximation, since it is heavily dependent on the loading condition of the engine and the type of fuel used. Such aspects are for the moment disregarded since this discussion has the only object of highlighting soft fouling importance on emissions and capital. The mass of added fuel can be evaluated as in Equation 5.3, with the internal efficiencies of the engine neglected.

$$\Delta P_B = \frac{\Delta R_F V}{\eta_{tot}} \quad \rightarrow \quad \Delta m = \Delta P_B\ SFC\ t \tag{5.3}$$

Table 5.1: Added fuel, costs and emissions due to biofouling

Scenario	Fuel mass $[t]$	Cost $[k\$]$	CO_2 $[t]$	SO_x $[t]$	NO_x $[t]$
Drydock	895	740	2836	1.789	63.53
No drydock	1223	1012	3878	2.447	86.87

Table 5.1 shows the total added fuel, emissions and expendend capital for both the drydock and no-drydock scenarios. The emissions have been obtained considering that for a ton of burnt MGO, $3.17\ t$ of CO_2 are produced, as well as $71\ kg$ of NO_x and $2\ kg$ for Low Sulfur Fuel Oil. The current price for MGO is $827\ \$/ton$. The benefits of drydock are in this case not made evident, since it appears that only $300\ k\$$ are saved if the two scenarios above shown are considered, while the emissions reduction is not relevant enough to justify a maintenance period. It is however somewhat eventful that a biofilm generated by only diatoms in a longer period of time still generates a revenue loss of up to one million dollars of capital. This implies that, if more than one specie of biofouling was to be taken into account, the growth would become faster, making such losses even more relevant.

5.2.3. Sensitivity study

A sensitivity study is carried out by systematically modifying the values of the superposition constants. This provides an overview of the uncertainty of the developed model with respect to the equivalent sand-grain roughness height. This is done only for the no-drydock scenario as shown in Figure 5.10, and considering a draft of $0.3\ m$ to appreciate the full extent of light intensity influence on k_s. The values are varied at steps $\Delta c_i = 0.1$ in the range $0.1 \div 0.6$. Only the combinations that sum up to a total of 1 are considered, to maintain the superposition normalized. Sea Surface Temperature is the variable that mainly determines the steepness of the trends: to higher c_t values correspond a sooner fully developed biofilm, and the rapidity of growth decreases with the constant. Six main groups are recognized, one for each of the possible values that the temperature-related constant can have. This implies that the uncertainty deriving from the choice of a c_t over another is high, as even small variations produce widely scattered values. Inside the above mentioned groups, the phosphorous concentration constant c_n influences the reaching time of $k_s = 300\ \mu m$ the most, with higher values increasing the steepness of the curve.

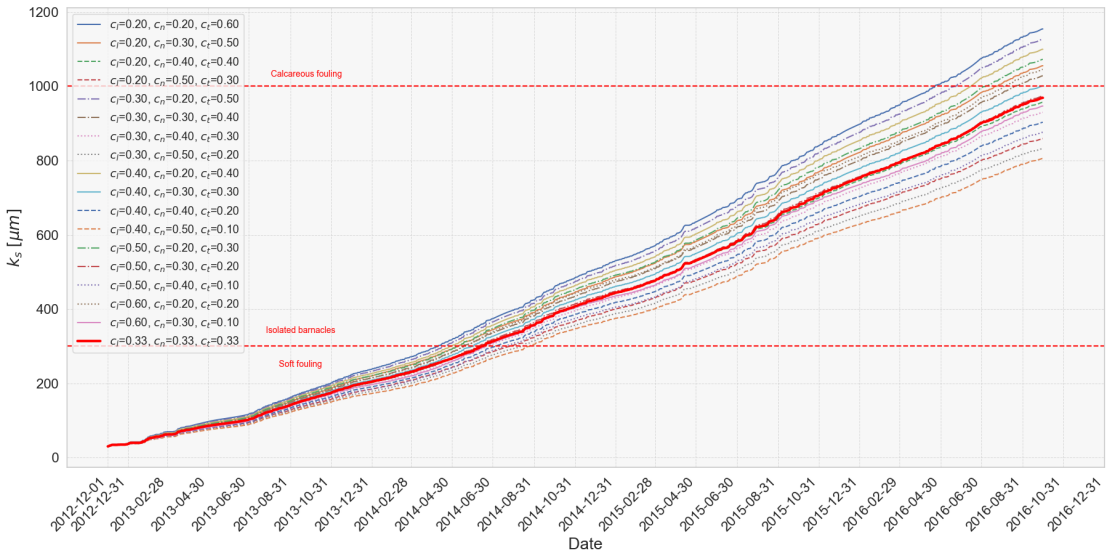

Figure 5.10: Uncertainty analysis deriving from superposition constants for k_s

It is possible to conclude that the choice of c_t involves the greatest uncertainty, followed by nutrients and light intensity, which does not possess a wide scatter even for points of the hull close to the water surface. It is to be expected that such variations will be even smaller for the round bilge and bottom of the ship. The choice of the constants $c_t = c_n = c_l = 0.33$ also results to be convenient, as the corresponding trend (represented with a thicker red line in the figure) falls approximately in the middle of the range. This means that the overall uncertainty of the date in which the soft fouling limit is reached amounts to 75 days.

Figure 5.11 shows a comparison between the surface roughness evolution obtained through the superposed growth rate μ, and those calculated with only one of the environmental variables considered at the time. This allows to analyse what is the error committed in the choice of 0.33 as value for all the constants. It may be argued that the growth rate μ could have been evaluated by summing the contributes of the single variables, without any type of normalization. It is however not clear how the different environmental conditions interact with each other in terms of total growth. It is possible that, namely, an excessive sea surface temperature would limit the concentration of nutrients and other substances dissolved in the water. Furthermore, the equations used to evaluate μ_{temp}, μ_{light} and μ_{nutr} have all been obtained by fitting experiments results from the literature. In these, the main environmental factor under study was only virtually isolated from the others. This means that the steep trend for temperature in the figure also takes into account other contributes in its formulation, which are not clearly reported in the papers as they are part of the general environmental conditions the experiments have been done with. The rate at which each of the trends increase is correlated with the relative error committed in the choice of the variable c_i. It can be concluded that, as already explained for Figure 5.10, temperature implies the greatest uncertainty, followed by phosphorous concentration and light intensity.

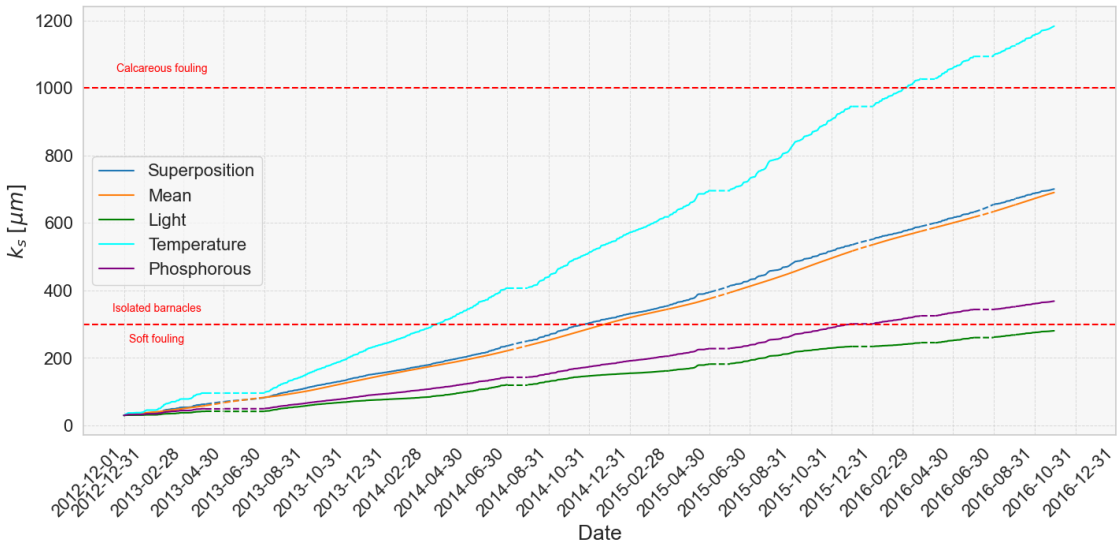

Figure 5.11: Influence on k_s of superposed growth rate μ definition

Influence of draft

Assuming that the superposition constants are the same used for the previous dissertations, it is possible to evaluate what the k_s evolution is in different points on the hull. Figure 5.12 shows the resultant surface roughness for a range of drafts in the no-drydock scenario.

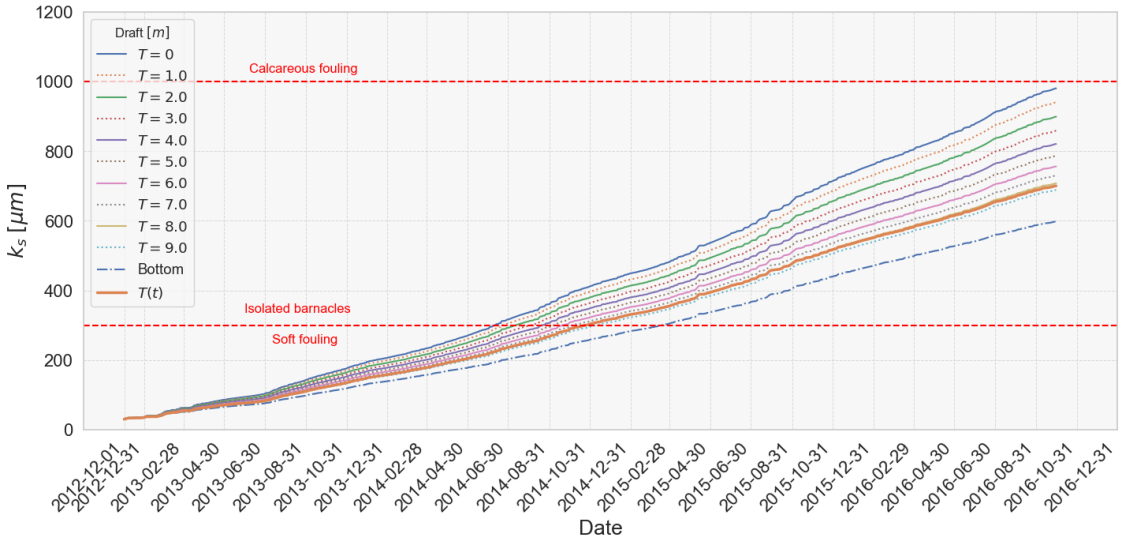

Figure 5.12: Draft influence on k_s

As expected, k_s development is faster for points of the hull positioned right below the waterline. In such case, the light intensity is not significantly affected by the absorption of water molecules ($I = I_0$). As depth increases, the light reaching the considered area is progressively lower. The minimum is reached for a point on the bilge ($T = 9.0\ m$). It is here assumed that such draft corresponds to the maximum loading condition, and it cannot be exceeded for safety reasons related to freeboard regulations. The time-span difference it takes to reach $k_s = 300\ \mu m$ between a point on the free surface and on the bilge is of 5 months. The trend lines are also progressively closer to each other as draft increases. The k_s time evolution of the entire bottom of the ship is also shown. Since this is not directly exposed to sunlight, the diffracted light from Equation 3.21 is used. This is in the order of 100 times smaller than the ordinary light intensity. Because of this, the value of $k_s = 300\ \mu m$ for soft fouling limit is reached three months later than any point in the round bilge. This behaviour highlights the relatively low influence light intensity has on the total growth rate, as the distance from the waterline increases. It should be highlighted that, in reality, multiple additional factors not included in the model may bring to a fully developed biofilm on the bottom, sooner than on the sides of the hull.

5.3. CFD

The results of the numerical simulations are here presented. First, the influence of surface roughness for the simple case of the flat plate will be analysed. Then, the outcomes of the full-scale containership will be provided. These include the frictional resistance trend, wave profile modification for a range of k_s values and influence on propeller.

5.3.1. Flat plate - Influence of surface roughness

The wall-resolved simulations involve the implementation of a surface roughness value k_s on the flat plate portion of the domain. The investigated values $k_s = (0, 50, 150, 300)\mu m$ are computationally input using Wilcox roughness model reported in Equation 5.4, with constant $A = 5.2$.

$$\Delta U^+ = \frac{\kappa}{ln\left(\frac{y^+}{A}\right)} \tag{5.4}$$

Figure 5.13 shows the results for added frictional resistance from Equation 5.5. This is then divided by the smooth drag, throughout the flat plate non-dimensional length, for different roughness values. The behaviour of the flow at only half-height of the plate is considered. This is possible because of the simulation characteristics, since the uniform steady flow aligned with the surface will generate the same frictional resistance at different heights. As expected, the skin friction ratio is higher at the leading and trailing edges of the plate. Such a trend is direct consequence of a greater shear stress, given the velocity gradients caused by the impact of the flow with the plate, and its detachment on the tail. Such an increase is more prominent as the surface roughness grows. The remaining surface of the plate presents a similar behaviour for all k_s, with the only difference given by their values.

$$\Delta C_{F,k_s} = C_{F,k_s} - C_{F,smooth} \tag{5.5}$$

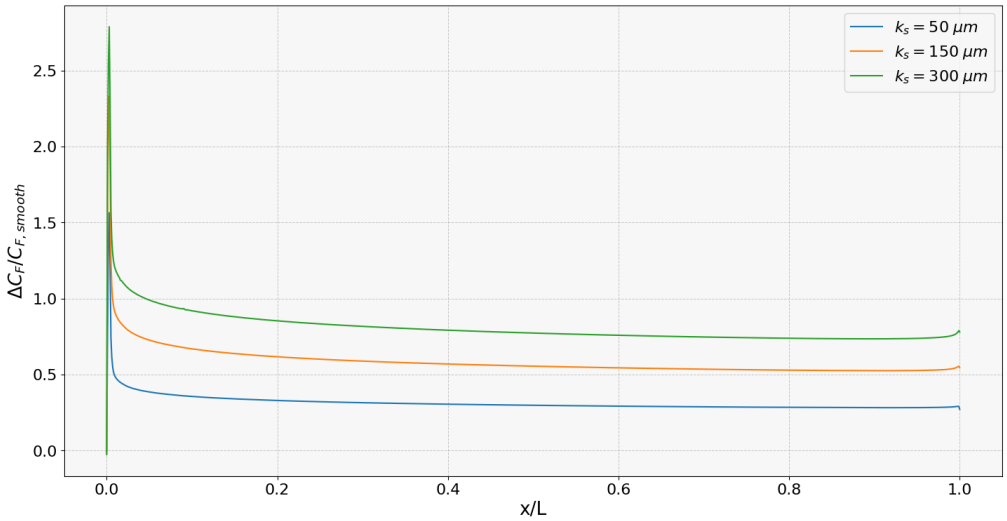

Figure 5.13: Added frictional resistance comparison for k_s value

Table 5.2 shows the global drag values for the range of equivalent sand-grain roughness heights, as well as their percentage increase in comparison to the smooth condition. The increment is not linear, but presents a steep surge in total frictional resistance as soon as the smooth wall condition is lost. Then, the trend flattens as surface roughness continues to increase, up until a converged value is reached. A significant increase of the total drag can then already be visualized for low k_s values, connected to soft fouling.

Table 5.2: Total and added frictional resistance for flat plate for the input k_s

k_s $[\mu m]$	C_F	$\%\Delta C_F/C_{F,S}$
0	$1.422 \cdot 10^{-3}$	–
50	$1.878 \cdot 10^{-3}$	32.1
150	$2.275 \cdot 10^{-3}$	60.0
300	$2.599 \cdot 10^{-3}$	82.8

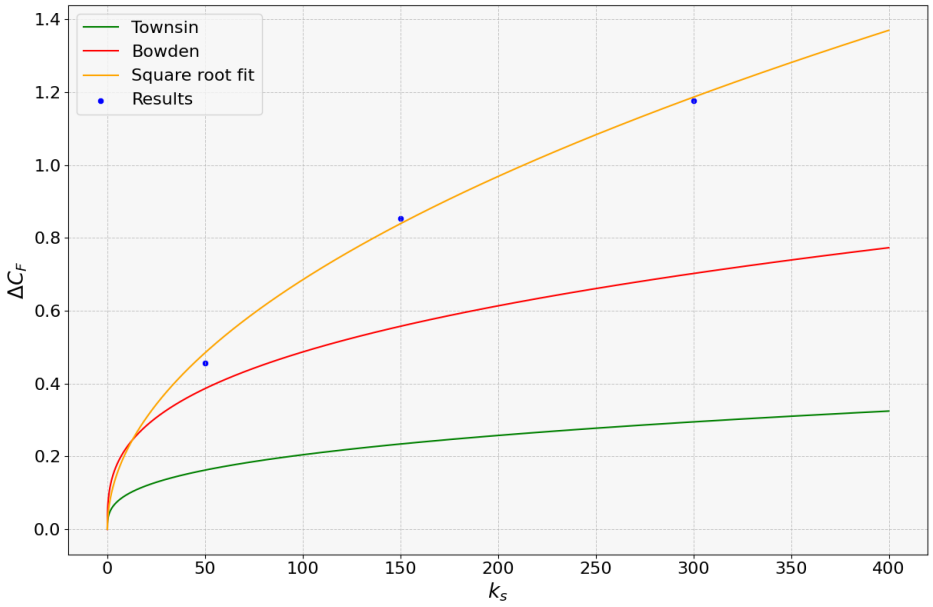

Figure 5.14: Comparison of flat plate ΔC_F with analytical formulations

What above explained can also be visualized in Figure 5.14. This shows the interpolated trend between the points reported in Table 5.2, together with the ΔC_F from different analytical formulations. Both Bowden et al. [38] and Townsin [33] equations (respectively 2.12 and 2.11) do not represent the additional resistance due to roughness on a flat plate. This is to be expected, since they are empirical correlations that estimate ΔC_F for ships, and they consider the cubic root of k_s. On the other hand, the curve fitted to the points obtained from the simulations has equation $\Delta C_F = 0.0704\sqrt{k_s}$. The difference in the order of the trends is to be implied to the geometry of the objects. The mentioned analytical formulations allow to include the effect of a ship's complex geometry, and free-surface effects on the incoming flow.

Some conclusions can be drawn from the results above presented. As already mentioned, the steep increase in ΔC_F for low surface roughness values suggests that soft biofouling can significantly impact the hydrodynamic performance of the plate (and thus of more complex objects). This highlights the great benefits that a better understanding of biofilm characteristics and behaviour would bring to the field. It however must be reminded that the initial coating roughness already implies a degradation of the overall ship performance. This means that the sharp increase for k_s close to zero is not to be implied to biofouling of any kind, but rather to coating roughness. The observed pattern also stresses the importance of early intervention in biofouling management: well-programmed drydock periods can help saving a considerable amount of emissions and expended capital, both in terms of fuel, and of duration of the hull cleaning operations.

5.3.2. Containership - Frictional resistance

Frictional resistance is known to be heavily affected by surface roughness. Despite it not being the main focus of the project, an overview of how it varies for different conditions is provided. Because of this, only the results for $V = 14\ kn$ are shown here. The other speeds are reported in Appendix D.

Figure 5.15 shows the skin friction ratio $C_{f,ratio}$ distribution on the hull for $V = 14\ kn$. This is defined as the ratio between the local skin friction coefficient C_f, and that of a reference smooth flat plate $C_{f,ref}$, dependent on the local Reynolds number Re_l. Both are reported in Equation 5.6. The differences between the two conditions are very evident throughout most of the ship. Already from the bulb, the ratio has approximately maximum value of 1.50 for rough condition, while the hydraulically smooth condition oscillates between $C_{f,ratio} > 1$ and $C_{f,ratio} < 1$. The fore shoulder, amidship and aft shoulder areas present a much higher skin friction (i.e. shear stress τ_w) in the rough condition. The skeg and transom have more similar ratio distribution, despite the generally greater values and spread of the high roughness case.

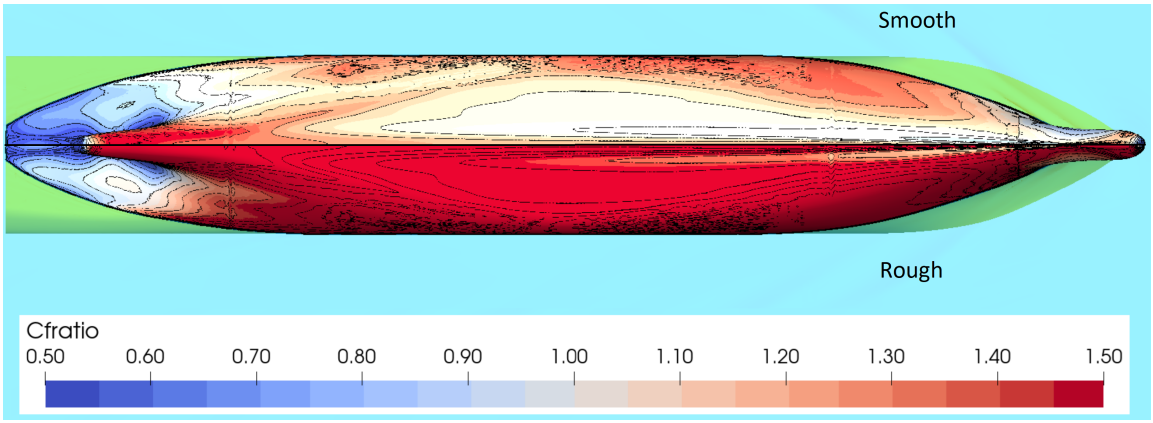

Figure 5.15: $C_{f,ratio}$ comparison for smooth and rough $k_s = 300\ \mu m$ surface for $V = 14\ kn$ (bottom view)

$$C_f = \frac{\tau}{\frac{1}{2}\rho V^2} \qquad C_{f,ref} = 0.37\, log_{10}(Re_l)^{2.584} \tag{5.6}$$

The skin friction coefficient C_f can be then used to obtain the shear stress distribution on the hull. A step forward in the development of a more complex and accurate model is the implementation of detachment occurrence. This implies that each of the species forming the biofilm can be associated with a shear stress value that causes them to separate from the hull, thus decreasing the surface roughness in that point.

The effect of increased shear stress and skin friction coefficient is a higher frictional resistance, since C_F is the surface integral of C_f. Table 5.3 illustrates the frictional resistance coefficient values for the input k_s values, as well as the percentage increase with respect to the smooth condition. This is characterised by $C_F = 1.578 \cdot 10^{-3}$, and increases up to $2.29 \cdot 10^{-3}$ at the soft fouling limit. The greatest relative increase occurs when passing from smooth to slightly fouled hull $k_s = 50\ \mu m$, with a 17.5% higher frictional resistance. The maximum increment is of 45.1% for the worst hull condition considered. The results reported in Appendix D for an inflow speed of 7 knots confirm the trend: the maximum increase amounts to 34.3%, thus meaning that roughness in the soft fouling range has a smaller influence on resistance at low speed. At $20.5\ kn$ the increase amounts to 52%. It can therefore be concluded that, as indicated in the literature, surface roughness holds a significant influence on frictional resistance. The relevance of this is even higher for displacement ships designed to sail at low speeds, where C_F covers great part of the total resistance.

Table 5.3: Containership frictional resistance and increase to smooth condition for $V = 14\ kn$

$k_s\ [\mu m]$	C_F	$\%\Delta C_F/C_{F,S}$
0	$1.578 \cdot 10^{-3}$	–
50	$1.855 \cdot 10^{-3}$	17.5
100	$1.993 \cdot 10^{-3}$	26.3
150	$2.092 \cdot 10^{-3}$	32.5
200	$2.169 \cdot 10^{-3}$	37.4
250	$2.233 \cdot 10^{-3}$	41.5
300	$2.290 \cdot 10^{-3}$	45.1

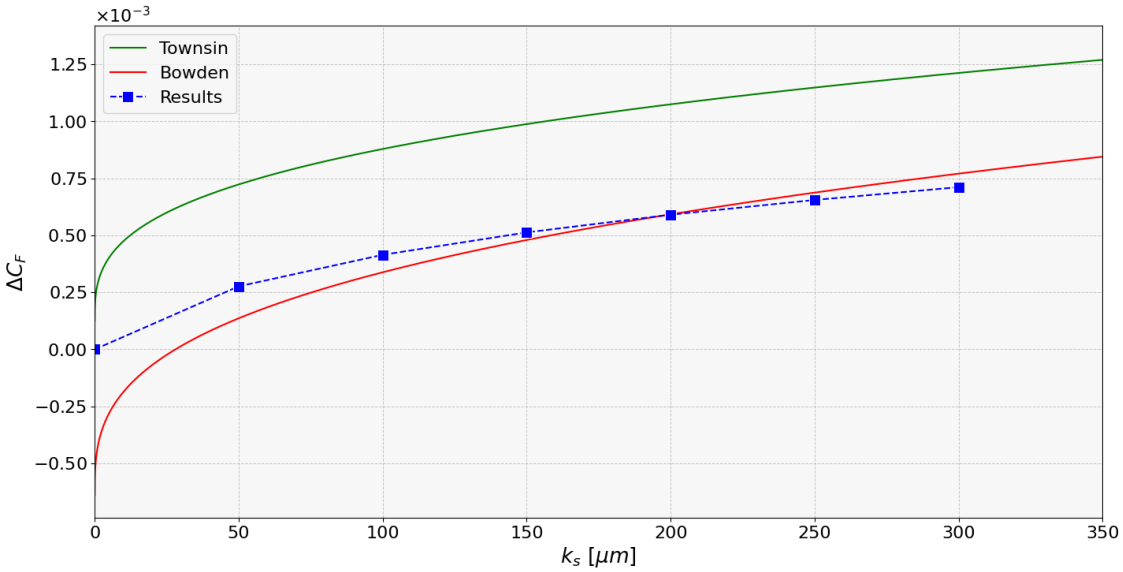

Figure 5.16: Added frictional resistance ΔC_F for containership at $V = 14\ kn$

Figure 5.16 shows the added frictional resistance results for the range of input k_s, at steps of $50\ \mu m$. These are plotted together with the empirical formulations proposed by Townsin and Bowden. Both use the Average Hull Roughness instead of k_s as representative roughness characteristic. This means that the constant α in the relation $AHR = \alpha k_s$ needs to be explicitly stated. The results from Eça et al. [79] for a KCLCC2 tanker show that $\alpha = 1.35$ for Bowden's equation, and 8.4 for Townsin's. As already mentioned in Section 5.2, Bowden's formulation provides negative added frictional resistance for low roughness values. Such a behaviour is not feasible, since an rise in k_s can only cause a positive increase in resistance. This is however justified by the fact that the formulation was obtained through fitting of data deriving from existing ships. These are all characterized, even after hull cleaning, by the roughness of the coating $k_s \geq 30\ \mu m$. A completely smooth surface is also a purely ideal condition, used to quantify the increase in resistance with respect to a standardized scenario. Townsin seems in this case to completely overestimate the added frictional resistance, presenting an average of 0.50 increase in the coefficient. The results are in accordance with Bowden's equation only for higher roughness values, and especially in the range $150 \div 250\ \mu m$. Considering the trend of the results, it is expected that higher k_s will not comply with either equations. To understand the full extent of this differences, a coefficient α specific for the containership should be used instead. Similar considerations apply to Figure D.11, where Townsin is asssociated with $Re = 5.28 \cdot 10^5$. Section D.2 contains an overview for all speeds of the k^+ distribution on the hull. This provides an indication on the type of flow occurring on the ship. The consequences of this on the numerical setup will be discussed in Chapter 6.

5.3.3. Containership - Residuary resistance

The previous section highlighted the influence of surface roughness on the frictional resistance of a ship. This analysis aims to provide an answer to the lack of clarity in the literature about the true influence roughness holds on residuary, and especially wave resistance.

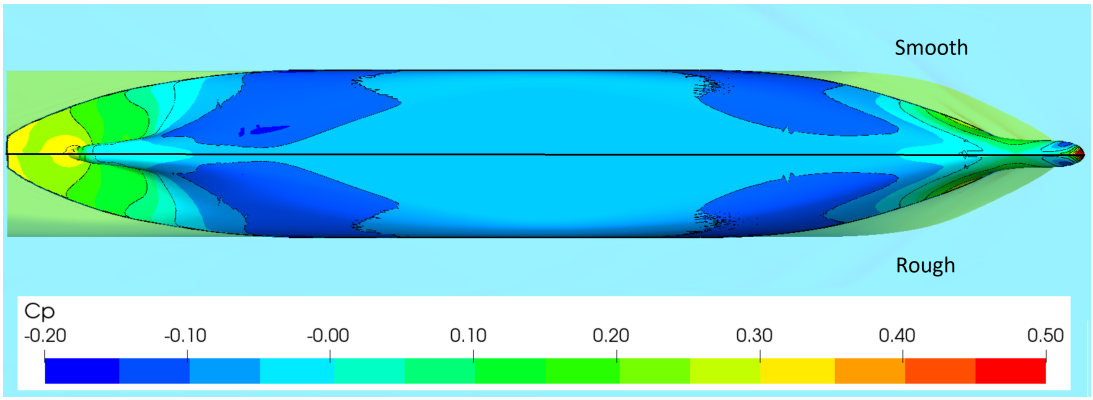

Figure 5.17: Pressure coefficient C_p comparison at $14\ kn$ between $k_s = 300\ \mu m$ and $k_s = 0$ (bottom view)

Figure 5.17 shows the distribution of the dynamic pressure coefficient C_p on the hull. Such variable has formulation reported in Equation 5.7, and it is dependent on both the dynamic P_d and hydrostatic P_{hs} pressures. Despite an increase in roughness of $300\ \mu m$, there are no relevant differences observed between the conditions. This is especially the case for bow and amidship. The most visible differences occur only at the stern and transom, where roughness creates a decrease in the extension of the higher pressure areas. It is therefore possible to conclude that the variable is not significantly affected by surface roughness, unless an adverse pressure gradient occurs. A reduction of the wave pattern elevation immediately after the transom is expected. These results can be explained by the influence of roughness on the boundary layer, that makes it thicken and accelerate its transition to fully turbulent regime. The adverse pressure gradient on the stern regions can create separation of the flow, thus generating a low-pressure wake region.

$$C_p = \frac{P_d - P_{hs}}{\frac{1}{2}\rho V^2} \tag{5.7}$$

Changes in the pressure distribution on the hull can lead to variations in wave-making resistance, a significant component of the total resistance a vessel encounters. Figure 5.18 shows a comparison between the wave patterns generated by the ship for the two extreme conditions of the analysed range at $V = 14\ kn$: smooth and rough $k_s = 300\ \mu m$ hull. The same figure for 7 and 20.5 knots are reported in Appendix D. It is possible to notice how roughness does not generally create significant changes in the wave elevation, especially at the bow and midship. Both conditions generate the highest peak in correspondence of the bulbous bow and at the transom, while the lowest troughs are created at the fore and aft shoulders. The main difference in the figures is given in the wake field, immediately aft of the transom. In that position the wave amplitude for the smooth condition is greater than for the rough case. As already discussed, roughness alters the characteristics of the boundary layer by increasing its thickness and making it transition earlier from laminar to turbulent flow. This thicker, more turbulent boundary layer can suppress the pressure variations along the hull that are responsible for generating larger waves.

At the design draft, the transom is dry. The pressure distribution on the hull can however generate waves that make it go partially under water. This possibility is checked in Appendix D for all speeds. For all fouling conditions the transom remains almost completely dry, thus not generating further increases in frictional resistances and another wave train (see Table D.1).

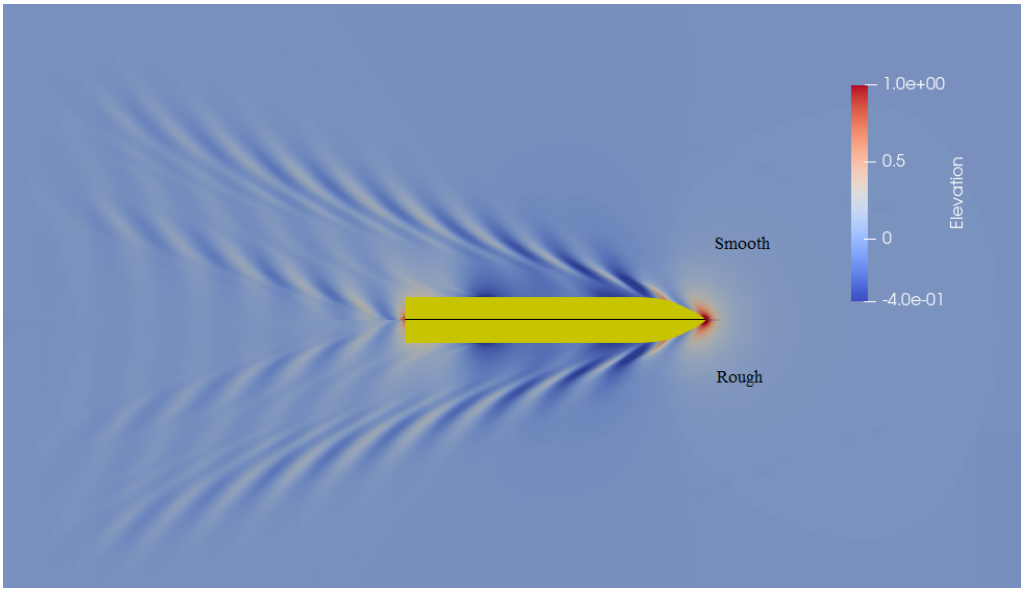

Figure 5.18: Wave pattern for smooth and $k_s = 300\ \mu m$ hull condition at $14\ kn$

A better visualization of the phenomena is provided in Figures 5.19, 5.20 and 5.21. These show the wave elevation for free-surface cuts at three transversal distances from the hull, for three surface roughness conditions. Small variations in the behaviour where none is expected (especially at the bulb and at locations fore of the vessel) can be implied to the convergence of the solution. The wave height along the hull is not influenced to any extent by surface roughness, exception made for a higher peak of the smooth condition at the bulb. Some modifications appear at the transom ($x = -5.5\ m$), where the wave elevation reaches $0.852\ m$ for smooth hull and $0.796\ m$ for the highest roughness. As previously noticed, the most relevant differences are however generated in the wake field. In the range $-66\ m \leq x \leq -13\ m$, the smooth hull presents a regular oscillating behaviour, with peaks and troughs of $0.2\ m$ in height. The same cannot be concluded for the fouled ship conditions: the pressure distribution on the hull make it so that the waves are not as high, and the troughs for $k_s = 300\ \mu m$ are above the still water level. After that, the wave pattern is more quickly dampened as roughness increases, reaching the undisturbed surface condition at a shorter distance from the transom.

The variations due to roughness are much more evident in Figure 5.20, for the wave cut obtained at $y = 0.55B$. The pattern is here different due to the propagation angle of the waves, that causes the highest peak $H_{wave} = 0.556\ m$ for all k_s at the fore shoulder, instead of at the bulb location. While height is not significantly affected, the waves at the longitudinal coordinates of the hull are interestingly heavily shifted for $k_s = 150\ \mu m$, whereas the other two are almost entirely equivalent. From the aft perpendicular and towards the stern however, the similarity is between the rough scenarios, although the smooth hull is characterised by wider and higher waves. The undisturbed condition is reached at around $x = -260\ m$ for all input roughnesses. The average difference in wake wave height for the fouling scenarios is of $0.5\ m$ in both peaks and troughs, with smooth peaks of $0.2\ m$.

Finally, the wave cut extracted at $y = 0.25L_{pp}$ can be analysed. Once again, because of the waves propagation angle (Kelvin angle), the presence of the hull is first acknowledged aft of the fore shoulder. Two main behaviours can be visualized: for $x > 16\ m$ the two fouled conditions are equivalent in both wave height and longitudinal disposition (trough $H_{wave} = -0.31\ m$), whereas $k_s = 0$ is shifted towards the stern. This may suggest that the wave propagation angle is also influenced by surface roughness. Aft of the skeg ($x < 16\ m$), each of the conditions generate a different wave pattern, both in height and position of peaks/troughs. In this case, the ΔH_{wave} between the fouled conditions and smooth is on average $0.03\ m$, thus essentially a negligible variation.

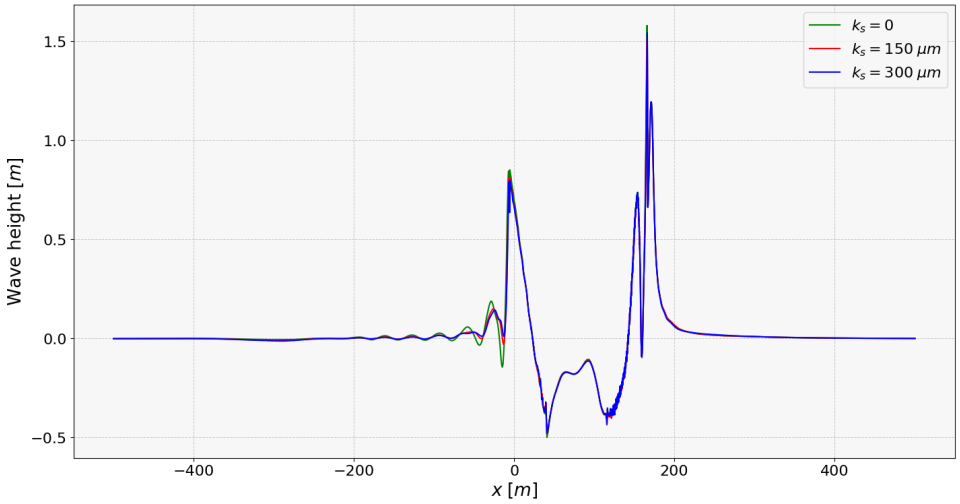

Figure 5.19: Wave elevation at $y = 0$ and along the hull, $V = 14\ kn$

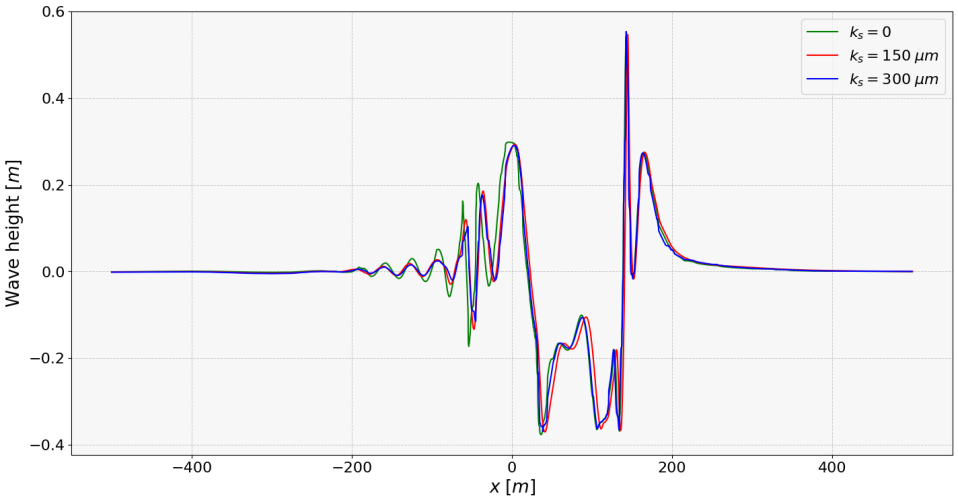

Figure 5.20: Wave elevation at $y = 0.55B$, $V = 14\ kn$

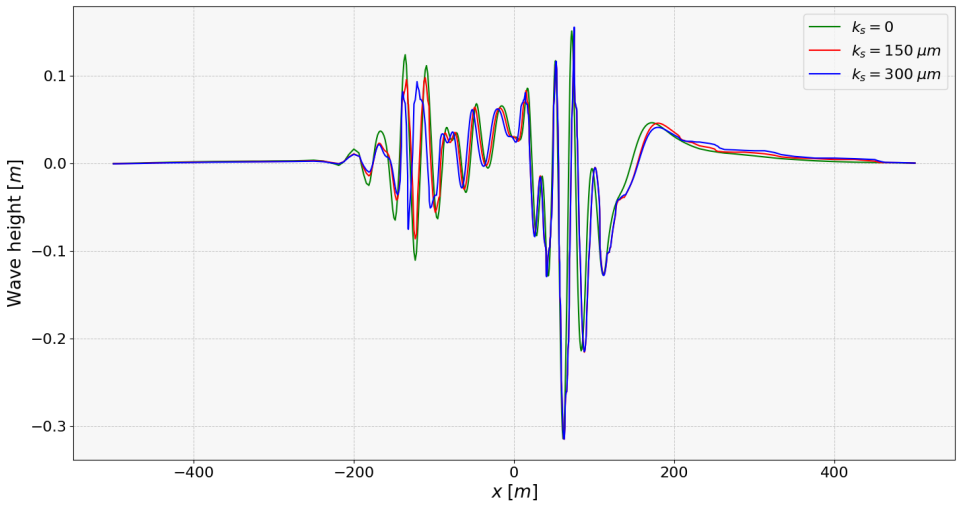

Figure 5.21: Wave elevation at $y = 0.25L_{pp}$, $V = 14\ kn$

Figure 5.22 and 5.23 show a comparison of the percentages of each resistance component for the range of k_s. The total resistance coefficient C_T is considered to be split as in Equation 2.9. The standard output of ReFRESCO simulations however does not provide a separation of the residuary resistance into viscous-pressure and wave-breaking. Instead, only the frictional and pressure factors are output. The separation is operated by evaluating the form factor k through Holtrop & Mennen [37] in Equation C.3. The standardised approach for its evaluation involves double-body simulations. For time-management reasons, this possibility is not explored in the project. The subdivision of the residuary resistance is therefore only fictional, used to provide an indication on the relative importance between its two components. The lower pressure field shown in Figure 5.17 may generate a increase in C_{VP}. The thicker boundary layer can however also yield a lower influence of pressure on form, thus decreasing the coefficient.

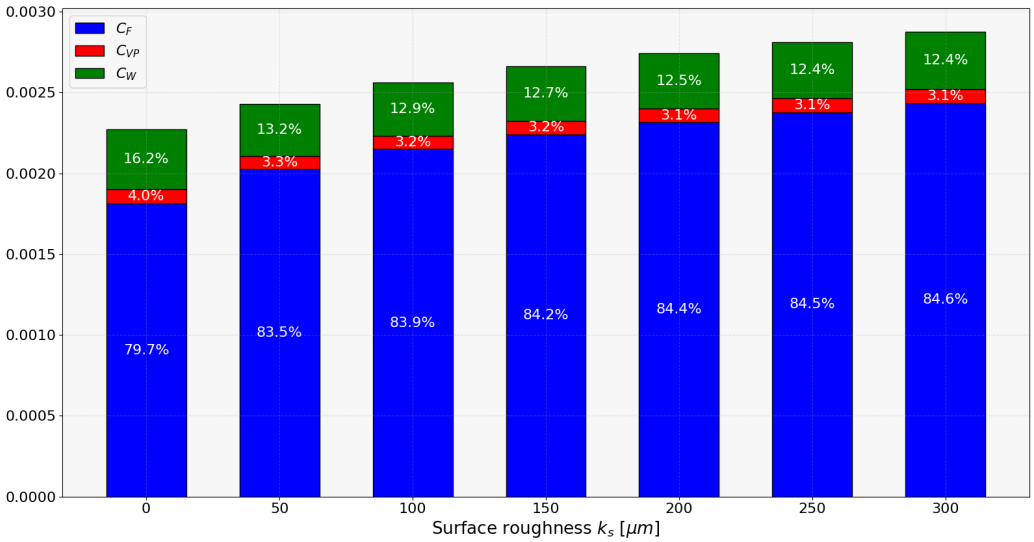

Figure 5.22: Percentage bar diagram of the resistance components at $7\ kn$

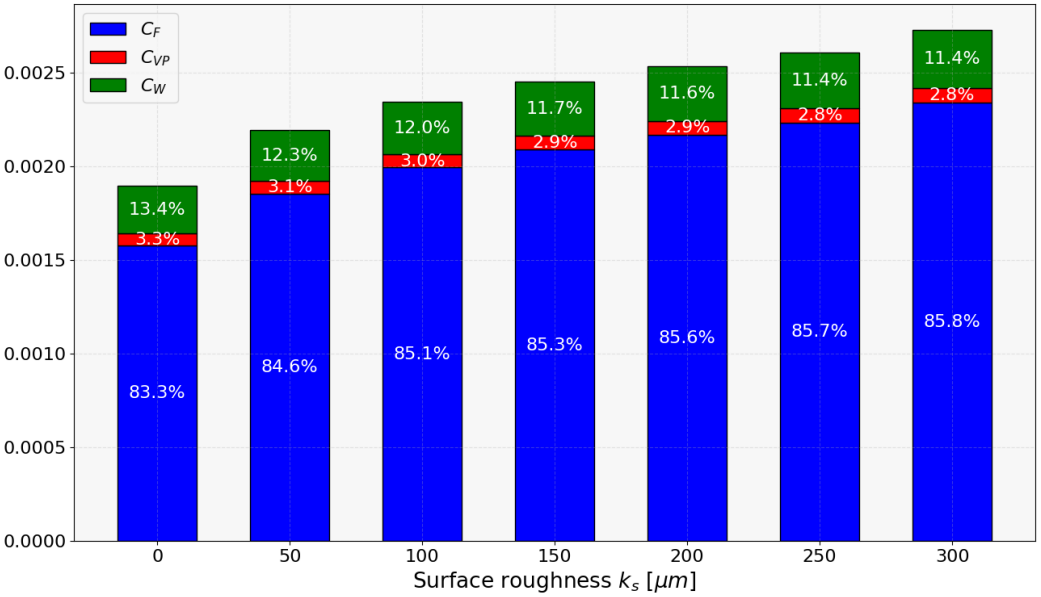

Figure 5.23: Percentage bar diagram of the resistance components at $14\ kn$

The figures confirm the trend observed for the frictional resistance. The increase is indeed steeper when passing from smooth hull to lightly fouled $k_s = 50\ \mu m$. The variations are then progressively smaller as the biofilm continues to develop, especially for $V = 7\ kn$. Overall, the relevance of C_F increase from 79.7% to 84.6% for the lower speed, and from 83.3%, up to 85.8% at $14\ kn$. The most relevant information is the behaviour of the residuary resistance ($C_{VP} + C_W$). It appears that C_R decreases as the level of hull fouling increases, at least as far as the biofilm range is concerned. A maximum variation of 2.5% is observed for $14\ kn$, with the resistance portions going from 17.7% of the total resistance in smooth condition, to 14.2% for $k_s = 300\ \mu m$. According to Figure 5.22, the maximum variation amounts to 4.7% at $7\ kn$ of inflow speed. Even though C_R is less relevant at low velocities, it results more comparatively important for $7\ kn$ than $14\ kn$. This can be implied to the bulbous bow. Considering the design speed is $V = 20.5\ kn$, the bulb is fit to generate a wave train able to lower resistance at such velocities. This is confirmed in Figure D.16, where the wave-breaking resistance covers importance in the order of 23%. Comparing the Froude numbers in Table 3.16 with Figure 2.11, C_W is relatively more important at the lower speeds. Residuary resistance for low V may therefore be more heavily affected by soft fouling, if the operational conditions do not correspond with the design scenario. These fundamental results allow to answer the research question relative to the influence of roughness on residuary resistance.

A complete overview of how residuary and frictional resistance coefficients vary with k_s is given in Figure 5.24. The non-dimensional coefficients are obtained through division by speed and wetted area S, influenced by trim and sinkage. Such characteristics are reported in Table 5.4. S is assumed as constant for different fouling conditions, since the variations in wave pattern are proven to be negligible. The value for the complete ship is indicated, even though the simulations were run for only half hull. Initial trim and sinkage were input after a first simulation where the dynamic components were implemented. Using the same values for two speeds does not generate differences in the results, as it only influences the number of iterations needed to reach convergence of the solution. The trends confirm what previously observed. It is however interesting to notice how C_R for the low speed initially decreases from smooth to $k_s = 50\ \mu m$. Then, it steadily increases up to a value of $4.95 \cdot 10^{-4}$. The same does not occur at $V = 14\ kn$.

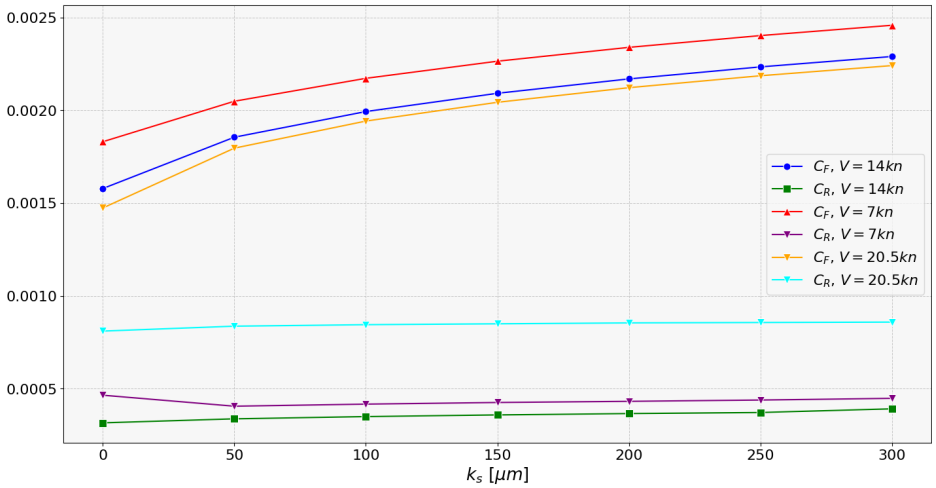

Figure 5.24: Influence of roughness on frictional and residuary resistance

Table 5.4: Wetted surface, initial trim and sinkage

Variable	$V = 7\ kn$	$V = 14\ kn$	$V = 20.5\ kn$
Wetted surface $S\ [m^2]$	5932	5870	6099
Initial trim $[°]$	0.002	0.002	0.005
Initial sinkage $[m]$	-0.176	-0.176	-0.397

5.3.4. Containership - Influence on propeller performance

The above-illustrated wake-field flow modifications are expected to also generate variations in the propeller performance. These can be quantified by analysing the normalised axial velocity V_x, given as a portion of the inflow speed V. Figure 5.25 shows the local V_x distribution at the propeller disk, for smooth and rough $k_s = 300\ \mu m$ conditions at 14 knots. The differences are not particularly relevant: the outer portions are not influenced by biofouling due to the lesser disturbances of the hull on the flow, keeping a value of $0.93V$. Small modifications are however present in the upper part of the propeller disk, where the area characterised by $V_x = 0.56$ is more extended for the rough hull. The non-negligible differences due to surface roughness are present close to the propeller hub. Here, $V_x = 0.56$ extends deeper in the radial direction, and the transition to higher speeds is achieved only further away from the object. Some variations are also present in the lower part of the mentioned area.

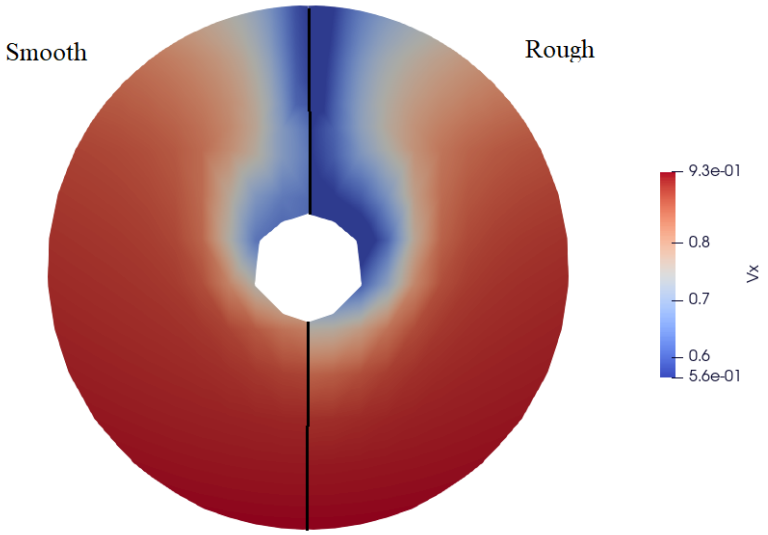

Figure 5.25: Local axial velocity V_x at $x = 0$ for $V = 14\ kn$

From the distribution of the axial velocities, the wake fraction w can be evaluated through Equation 5.8. This considers the dimensional axial velocity V_{mean}, obtained by the sum of local $V_{x,i}$. This results for the smooth hull in $V_{mean} = 5.772\ m/s$ and $w = 0.198$, and $V_{mean} = 5.488\ m/s$, $w = 0.238$ for the fouled case. Surface roughness for the soft fouling limit therefore generates $\Delta w = 0.04$, corresponding to an increase of 20% of the initial value. This does not imply a higher η_H: the added frictional resistance causes the propeller to work at higher loads, thus increasing the pressure induced on the stern and the thrust deduction factor t.

$$V_{mean} = \frac{1}{N}\sum_{i=1}^{N} V_{x,i} \qquad w = \frac{V - V_{mean}}{V} \tag{5.8}$$

5.4. Combination of the Results

The previous sections presented the results for added frictional resistance ΔC_F from data processing, growth model, and numerical simulations. It is now possible to connect them together to understand whether the predicted trend accurately represents the real behavior or not. To do so, the dates of the growth model corresponding to the CFD input k_s values are gathered (see Figure 5.7). These are then associated with the ΔC_F values in Table 5.3. The combined results are illustrated in Table 5.5 for clarity.

Table 5.5: Combined results for CFD and growth model

Date	k_s $[\mu m]$	$\Delta C_F \cdot 10^{-4}$
17/02/2013	50	2.76
04/08/2013	100	4.15
03/12/2013	150	5.13
19/04/2014	200	5.91
31/07/2014	250	6.55
25/10/2014	300	7.11

The points are then plotted in Figure 5.3 for direct comparison with the resistance trend. The values of growth + CFD are profoundly different from the ones indicated by the rolling average. There are a few reasons for this. First of all, the growth model starts on December 1^{st} 2012, which corresponds to the left boundary of the monitored period. At that time, $\Delta C_F \approx 1.36 \cdot 10^{-3}$ from data processing, suggesting that the ship is likely covered beyond the simple soft fouling condition. This implies an inherent difference in the initial state between the two methods. However, no information on the hull's condition was available at any point in time to ensure a consistent start across both approaches. Furthermore, the last point (October 25^{th} 2014) corresponds almost perfectly with the value indicated by data processing. This is however only given by the sudden drop in the rolling average. As previously mentioned in Section 5.1, such decrease may represent either a in-water hull cleaning, or a change in operational conditions. Since there is no evidence in the ship documentation, nor in the GPS position, it was disregarded. The point has thus a lower significance in terms of comparison between trends.

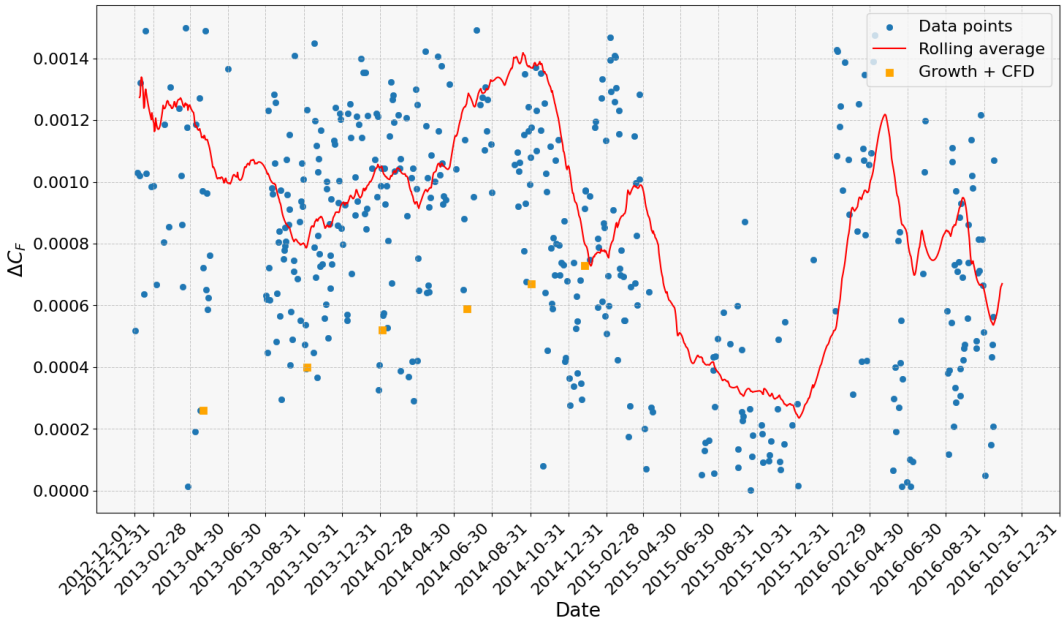

Figure 5.26: ΔC_F from data processing and growth model + CFD

The differences in intensity between ΔC_F values from data monitoring and growth + CFD were expected, because of the multiple assumptions carried out in the latter. It is still possible to compare the trends of the two approaches. Doing so can provide insights on whether the growth rate predictions are accurate or not. Figure 5.27 shows the isolated data points from the figure above, as well as the connected trend lines. The uncertainty bands for the methods are also illustrated. For the data monitoring trend, uncertainty is derived from the standard deviation of the added resistance distribution, $\sigma_{\Delta C_F} = 3.6 \cdot 10^{-4}$, calculated for the dataset processed and filtered using a 5 minutes averaged window. This helps obtaining a total of 31432 points, which significantly enhances the precision of the standard deviation estimate. Only the portion of the dataset included between the two dates indicated in the figure is however considered to evaluate $\sigma_{\Delta C_F}$. The uncertainty of the growth model derives from the sensitivity study in Section 5.2.3, and in particular the curves in Figure 5.10 with fastest and slowest growths. For the same dates reported in Table 5.5, the correspondent k_s values are gathered and used as input for ΔC_F through Figure 5.16 and the resultant blue curve. The expansion of the uncertainty box is given by the relation between k_s, FR_{tot} and μ. The main imprecisions for the growth model are given by the choice of the constants c_i in the growth rate. This implies that such uncertainty enlarges because $k_s \propto FR_{tot}^2 \propto \mu^2$. This can be seen more directly in Figure 5.10, by the greater temporal distance between the limit curves as time progresses. The uncertainty as of November 30^{th} 2014 amounts to $4.98 \cdot 10^{-4}$ for the upper limit, and $7.38 \cdot 10^{-4}$ for the lower.

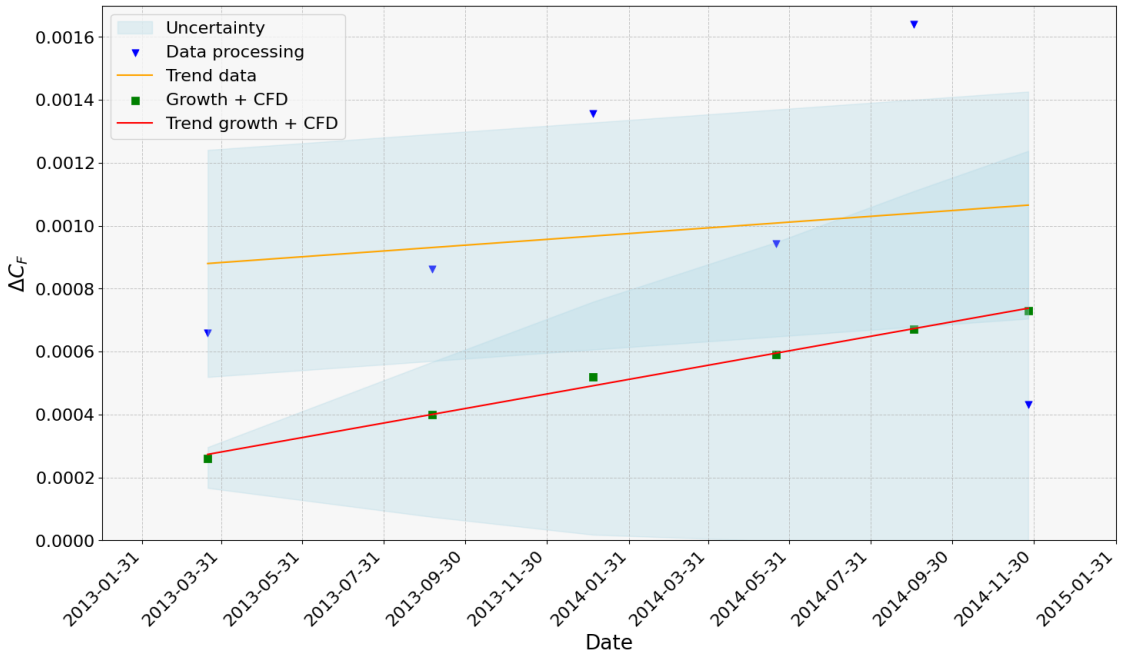

Figure 5.27: ΔC_F trends comparison and related uncertainty

As already discussed, the growth model underestimates ΔC_F, as the two trends present an average difference of $4.65 \cdot 10^{-4}$. Provided that the uncertainties of the growth model are quite relevant, and the heavy number of assumptions carried out throughout the procedure, it is possible to conclude that the two trends are sufficiently similar. The novel analytical model is thus able to represent with enough accuracy the increase rate of ΔC_F, at least for fouling conditions of $k_s > 50\ \mu m$. The added resistance however rapidly increases as the surface deviates from the smooth condition. For the reasons already explained, it was not possible to evaluate both methods from the same starting point. It is therefore not clear if the growth is accurately predicted also at $k_s < 50\ \mu m$ or not.

6

Discussion

6.1. Uncertainties in the data processing trend

As mentioned throughout the methodology and results chapters, a number of assumptions and simplifications have been carried out. These are inherent to the nature of either the exploited variables or procedures, and imply an inaccuracy in the obtained trend.

First of all, the dataset used consists in non-existing values for 19.5% of the total period considered. The moving average around the dates indicated in Table 3.5, depending on the choice of window, presents unexpected drops and trends that do not reflect the real behaviour of the variable. This effect is amplified by considering only data points associated with measurements speeds of $14 \pm 0.5\ kn$. Additional uncertainties derive from the draft values. These were rarely present in the original dataset, and are implemented in the model through noon reports. The information on such documents is gathered by the Master once per day. A double inaccuracy is here present: one given by the daily value, and the other deriving from the approximate number filled in by the Master. The noon reports are only available until July 2015. For lack of any other information on the matter, a draft equivalent to T_{des} is assumed after such time-frame.

As far as the methodology is concerned, the main assumptions are related to the evaluation of the propulsive coefficients through the BSRA regression series. The results of self propulsion tests of the model ship are only available for speeds comprised in the range $16 \div 20\ kn$. An alternative method for their calculation was thus necessary. Table 6.1 shows the values for $t,\ w$ and η_R from tests and regressions, as well as the percentage error for the above mentioned speed range. This helps understanding the entity of uncertainty to be expected for other V values. While the method is sufficiently accurate for t and η_R, the errors are in the order of 24% for the wake fraction. The uncertainty extends to the hull η_H and open water η_O efficiencies. The former does not consider the effect of biofouling: t and w should increase because of respectively higher propeller load, and reduced axial velocity at the propeller. The open water efficiency is available from the corresponding test results for the same speed range. Other values are obtained through the advance ratio J as input. This is also dependent on the wake fraction, meaning that the same errors indicated in Table 6.1 apply. Furthermore, the Holtrop & Mennen method is one of the best tools to date for providing a first indication of the resistance profile of a ship. Its application however entails an unknown degree of uncertainty if the vessel analysed is not part of the statistical series. This is even though the applicability conditions of the methods are checked and satisfied. The implementation of wind and waves effects on resistance likely holds the greatest uncertainty of the whole procedure. The paper does not consider the influence of such variables on resistance, since the predictions reflect ideal trial conditions. No reliable approach with high resolution for specific ship geometry is also present in the literature. The environmental forces are enriched from an archive based on weather hindcasts, and are therefore dependent on its accuracy.

Table 6.1: Propulsive coefficients comparison for scantling draft

V	t_{BSRA}	t_{test}	Error %t	w_{BSRA}	w_{test}	Error %w	$\eta_{R\,BSRA}$	$\eta_{R\,test}$	Error %η_R
16	0.198	0.169	14.6	0.325	0.245	24.6	1.033	1.000	3.19
17	0.198	0.166	16.1	0.321	0.241	24.9	1.032	1.001	3.00
18	0.198	0.171	13.6	0.318	0.242	23.9	1.031	1.002	2.81
19	0.197	0.177	10.1	0.315	0.243	22.8	1.030	1.002	2.71
20	0.197	0.174	11.6	0.313	0.239	23.6	1.029	1.003	25.3

6.2. Limits of the growth model

The nature of the theories used for the production of the growth model should be discussed to understand where possible limits lie. Namely, the equation by Steele [45] for light intensity is fitted to phytoplankton in the North Sea and in a sea loch on the west of Scotland. Because of the high latitudes of such locations, the equation may be more suitable to use for areas where grater seasonal changes in light availability occur. This means that the growth on the days when the ship was navigating around the south-most part of Africa may be more accurately represented than those in the Persian Gulf. The optimum light intensity I_{opt} for diatomic species endemic to specific locations is also different from others. A certain degree of approximation is present in considering the optimum light as a constant value. The ship will in fact encounter different phytoplankton species throughout its operative life. As far as nutrients are concerned, the freshwater microalga *Scenedesmus obliquus* is the species analysed to fit Equation 3.24. The choice of a formulation produced with a freshwater organism stems from the possibility to include the inhibition effect due to too high phosphorous dissolved in the water. Despite the generally lower P concentration in seawater in comparison to freshwater, the possibility to reach inhibition is acknowledged by the values adopted for K_i and K_P, relative to a salt water diatom. The last of the equations that should be discussed is the one by Bernard et al. [44] for SST, used to predict microalgal growth. Even though diatoms are not the original aim of the study, the dependency of the equation on specie-specific temperatures only allows to adapt the formulation to the project.

Some discrepancies are present in the measurement units of the individual growth rates. In Equation 3.13, μ is given by a linear superposition of the models that consider the single environmental variables. Since no systematic study on field experiments has been carried out at any moment in the project, the growth rate has been associated with a unit of $1/day$. This constitutes its most general definition, and allows for flexibility in case the present work needs to be expanded in the future. To understand whether such assumption is feasible for the model or not, a check of how the used equations were derived is carried out. The growth rate due to light intensity is measured in the original formulation through oxygen concentration in the water, and carbon fixation activity. This term refers to the conversion of inorganic carbon into organic substances. It is related to the photosynthetic process occurring in diatoms and phytoplankton. A daily variation in oxygen concentration can then be related to a modification in biofouling organisms density. This implies that using $1/day$ as a measure for growth rate is appropriate and does not involve heavy approximations. Similar considerations apply to Martinez's equation for the growth rate due to phosphorous concentration. This is measured in the original methodology by evaluating the water cell density. In conclusion, temperature's influence on growth from Equation 2.13 is fitted on experimental data measuring biomass concentration. Also in this case, time variations of such variable can be associated with daily developments in fouling presence.

Beside inaccuracies of the used formulations, multiple assumptions have been made throughout the development of the model. This can be visualized in Figure 5.7, where the time it takes for a single point on the hull to reach the soft fouling limit for k_s is extremely high. Firstly, only a few of the environmental and operational variables that in reality influence the biofilm development have been considered: minor, but yet important factors such as salinity, antifouling coating parameters and surface energy were neglected. This was done to simplify the overall procedure, which presents partially novel concepts

that would have otherwise been excessively problematic to implement. Furthermore, diatoms are the only species considered. It follows that integrating the combined effect on roughness of different organisms would have significantly decreased the time when the maximum k_s would have been reached. In addition to this, no information on the likelihood of attachment is included: surface energy has been disregarded and ship speed is incorporated only in terms of a reduction in growth rate. The model is thus based on considering the diatoms concentration in the hull biofilm, as equivalent to that in a point immediately close to the surface. Local foulers detachment could also cause a reduction in k_s that cannot be included in the model. This is becuase no theory on how to correlate growth with the shear forces that may cause detachment is available. A possible manner to include such effect is to carry out steady CFD simulations (no free-surface) for each speed of the containership operational range. The resultant shear stress can then be correlated with the maximum force bearable by the biofilm.

Modelling soft fouling through k_s implies considering the biofilm as a solid element. This does not allow to include deformation, nor porosity altering the flow that occurs next to it. Implementing such characteristics would help quantify the additional loss in ship performance. The choice of k_s stems from the lack of models that accounts for the otherwise mentioned variables. Furthermore, the equivalent sand-grain roughness height allowed to directly compare the results between methodologies, according to the procedure indicated in Section 5.4. That is because CFD simulations used k_s as the only variable describing surface roughness.

From the combination of the results in Section 5.4, it was clear that the growth model is able to predict the rapidity of growth with enough accuracy. However, no information is available on whether such precision also extends to $k_s < 50\ \mu m$, where added resistance increases steeply. It is expected that this is not the case, because of the assumptions above stated. These may imply a slower predicted growth than in reality. Moreover, the data trend for the considered period consists in ΔC_F values associated with hard fouling growing on top of the biofilm. The produced growth model is not meant to reproduce the behaviour of such phenomena. A comparison with more suitable data should thus be carried out if possible. In conclusion, data processing and growth model do not share the same starting status of the hull. This implies that the similarity between trends may be due to the sudden unjustified decrease of March 2013 in Figure 5.26. This matter should be further investigated by developing the analytical approach from a point in time when the condition of the hull is known.

6.3. Numerical simulations

The numerical setup for the full-scale containership should also be discussed. Based on the results, it is possible to understand whether the chosen settings are suitable or should be changed in future projects. As already mentioned, the boundary conditions and size of the domain accurately represent the physical phenomena, while the grid is sufficiently fine to capture it. This means that a good compromise between computational effort and convergence of the results was reached. The choice of the speeds was done to provide an overview of the influence of roughness for different operational conditions. It is however noted that more inflow velocities should be included to evaluate C_F and C_W for a range of Reynolds numbers. Choosing the most frequent speeds at which the ship has sailed may have however helped implementing the validation procedure.

Appendix D shows the k^+ distribution throughout the hull. This provides an indication on which kind of regime is occurring in each region. The subdivision is analogous between Nikuradse and the chosen Apsley model (see Section 2.1.2). The results show that k_s and V mostly generate flow in the transitional regime, exception made for Figures D.7 and D.9. Since Apsley's roughness function is mostly indicated for such fully rough regime, then its choice is not the most suitable for the project. Instead, Grigson model may be implemented. A more clear separation of viscous-pressure and wave-breaking resistance should have been carried out. However, obtaining the form factor k through double body simulations was unfeasible for time management reasons.

7

Conclusions

Biofouling species were analyzed, revealing their impact on increased costs and GHG emissions. A fluid dynamics analysis showed that marine growth alters the hull's boundary layer, raising resistance and power demand. The referenced literature indicated that equivalent sand-grain roughness height k_s is still a useful approximation to evaluate surface roughness, even though biofilm porous characteristics are not included. The scarce availability of comprehensive growth models was then brought to attention, and CFD techniques for biofouling were presented.

The monitored data was filtered, processed and enriched with environmental conditions. The dataset was used to calculate the added frictional resistance coefficient over five years through Holtrop & Mennen methodology. A maximum $\Delta C_F = 1.4 \cdot 10^{-3}$, and two possible drydocking periods were identified. While the data shows a meaningful trend for ΔC_F, uncertainties prevent precise values. The effect of speed on detachment wasn't directly proven, though small trend oscillations may suggest it.

Based on the findings from literature, a novel growth model able to include light intensity, sea surface temperature and phosphorous concentration in water was proposed. The total growth rate μ was then correlated to k_s through Uzun et al. [42] equation, showing that soft fouling limit is reached on an average of 16 months. This implies for the containership an increase in frictional resistance up to $62\ kN$, though only diatoms were considered. If multiple species were to be accounted for simultaneously, then the trend would become much steeper. Because of this, the potential benefits of hull cleaning (both environmental and monetary) are not evident as explained in Section 6.2. A sensitivity study showed how temperature is generally the most important variable among the considered ones, followed by nutrients and light intensity. This also confirmed that the choice of the constant values c_i does not affect in a significant manner the time in which the soft fouling limit is reached.

Numerical simulations of a completely submerged flat plate and full-scale containership were carried out. Both confirm how soft fouling k_s values generate steep increases in frictional resistance. These are in the order of 85% for the flat plate. For the ship, the increments are of 34.3% ($7\ kn$) and 45% ($14\ kn$). These cover respectively an increase of the total resistance from the smooth condition of 27.6% and 31.3%. As far as residuary resistance is concerned, the real effect on viscous pressure could not be proven without double-body simulations. Wave-breaking resistance is affected, at least for the range of soft fouling roughness, to a very limited extent: decreases of 2.5% and 4.7% in C_W were observed respectively for 7 and 14 knots of speed. These are visible in terms of changes in the pressure distribution on the underwater hull and in the wave pattern height of the wake field, especially in the areas after the transom. The total resistance increase is of 40.8% at 14 knots. It was proven that soft fouling increases the wake fraction w of 20% at such speed because of a difference in axial velocity distribution.

Finally, a comparison between the results from data processing and growth model + CFD was performed. This showed that the values in the period from Figure 5.27 present an average difference in ΔC_F of $4.65 \cdot 10^{-4}$. The trend steepness predicted with the growth model resembles that of the data processing. The developed methodology is thus suitable to represent growth in the range $50 \leq k_s \leq 300$.

8

Recommendations

Based on the assumptions, procedure and results obtained from the project, several recommendations for future works can be provided:

- **Improvement of employed dataset**: as widely explained in Section 3.1, the dataset obtained from monitoring contains a great amount of unavailable and not measured variables throughout the considered time period. The aftermath of this consists in a certain degree of uncertainty for both the growth model and added frictional resistance trend. It is suggested for future work to either implement a wider array of data processing and enrichment techniques, or to obtain a more complete dataset through direct cooperation with shipowners. This would increase the overall robustness of the methodology;

- **Expansion of the growth model to consider soft-mean fluid dynamics**: despite being composed of soft organisms, the biofilm was considered as a solid, non-porous material. No study on the fluid behaviour of soft-mean was carried out, implying that a portion of possible additional turbulence and energy losses occurring inside the biofilm are not included at any point of the project. Future works should therefore implement such phenomenon into the growth rate model;

- **Different kinds of biofouling species combined together in the model**: the growth model developed in this research considers diatoms as the only specie contributing towards the formation of the biofilm. The combined effect of multiple species should then be implemented. The predominance of one specie above another would have a great influence over the thickness and distribution of fouling. Further expanding from this point, hard fouling can be combined with soft species to reproduce a scenario which is closer to reality;

- **Inclusion of biofouling detachment and thickness study**: as mentioned in Section 6.2, a possible step forward in the development of growth models could be the implementation of shear stress results from steady CFD simulations. Combining such distribution with a model that connects growth and biofilm thickness may help modelling foulant detachments throughout the ship, thus improving the accuracy of the equivalent sand-grain roughness height trend;

- **Implementation of propeller in CFD**: implementing a strategy to evaluate effective influence of biofouling on the propeller for the full-scale containership simulations would help to visualize and quantify its performance loss. In such a way, the benefits of antifouling strategies to minimize surface roughness would be even more evident;

- **Resistance evaluation method**: the Holtrop & Mennen method, combined with BSRA regression series have been used. Despite having checked the applicability conditions, a certain degree of uncertainty still exist, as they are not proper to the containership in study. More accurate final results can be obtained if the ship directly derives from a systematic series, for which analytical regressions are known.

References

[1] European Commission. “Reducing emissions from the shipping sector.” (2023), [Online]. Available: https://climate.ec.europa.eu/eu-action/transport/reducing-emissions-shipping-sector_en (visited on 05/02/2024).

[2] International Maritime Organization. “Implementing the ballast water management convention.” (), [Online]. Available: https://www.imo.org/en/MediaCentre/HotTopics/Pages/Implementing-the-BWM-Convention.aspx.

[3] C. Bressy and M. Lejars, “Marine fouling: An overview,” *The Journal of Ocean Technology*, vol. 9, no. 4, pp. 20–28, 2014.

[4] S. Cao, J. Wang, H. Chen, and D. Chen, “Progress of marine biofouling and antifouling technologies,” *Chinese Science Bulletin*, vol. 56, pp. 598–612, 2011.

[5] W. H. O. Instituion, “Marine fouling and its prevention,” *Annapolis: United States Naval Institute*, p. 388, 1952.

[6] M. Salta *et al.*, “Marine fouling organisms and their use in antifouling bioassays,” in *Proc. EUROCORR*, 2009.

[7] J. Andrewartha *et al.*, “Drag force and surface roughness measurements on freshwater biofouled surfaces,” *Biofouling*, vol. 26, no. 4, pp. 487–496, 2010.

[8] J. W. Costerton, G. G. Geesey, and K.-J. Cheng, “How bacteria stick,” *Scientific American*, vol. 238, no. 1, pp. 86–95, 1978.

[9] L. Melo and T. Bott, “Biofouling in water systems,” *Experimental thermal and fluid science*, vol. 14, no. 4, pp. 375–381, 1997.

[10] M. J. Romeu and F. Mergulhão, “Development of antifouling strategies for marine applications,” *Microorganisms*, vol. 11, no. 6, 2023, ISSN: 2076-2607. DOI: 10.3390/microorganisms11061568. [Online]. Available: https://www.mdpi.com/2076-2607/11/6/1568.

[11] S. Abarzua and S. Jakubowski, “Biotechnological investigation for the prevention of biofouling. i. biological and biochemical principles for the prevention of biofouling,” *Marine Ecology Progress Series*, vol. 123, pp. 301–312, 1995.

[12] K. B. Schimanski *et al.*, “Factors influencing the en route survivorship and post-voyage growth of a common ship biofouling organism, bugula neritina,” *Biofouling*, vol. 32, no. 8, pp. 969–978, 2016.

[13] Y. K. Demirel, M. Khorasanchi, O. Turan, and A. Incecik, “On the importance of antifouling coatings regarding ship resistance and powering,” in *3rd International Conference on Technologies, Operations, Logistics and Modelling for Low Carbon Shipping*, 2013.

[14] M. Candries, M. Atlar, and C. Anderson, “Considering the use of alternative antifoulings: The advantages of foul-release systems,” *Proceedings ENSUS*, pp. 88–95, 2000.

[15] International Maritime Organization. “International convention on the control of harmful antifouling systems on ships.” (), [Online]. Available: https://www.imo.org/en/About/Conventions/Pages/International-Convention-on-the-Control-of-Harmful-Anti-fouling-Systems-on-Ships-(AFS).aspx.

[16] B. P. Pedersen and J. Larsen, “Prediction of full-scale propulsion power using artificial neural networks,” in *Proceedings of the 8th international conference on computer and IT applications in the maritime industries (COMPIT’09), Budapest, Hungary May*, 2009, pp. 10–12.

[17] M. P. Schultz, J. Bendick, E. Holm, and W. Hertel, “Economic impact of biofouling on a naval surface ship,” *Biofouling*, vol. 27, no. 1, pp. 87–98, 2011.

[18] International Maritime Organization. “Transparent and reliable hull and propeller performance standard.” (), [Online]. Available: https://bellona.no/assets/sites/3/2015/06/fil_MEPC_63-4-8_-_A_transparent_and_reliable_hull_and_propeller_performance_standard_CSC1.pdf.

[19] A. Farkas, N. Degiuli, I. Martić, and M. Vujanović, “Greenhouse gas emissions reduction potential by using antifouling coatings in a maritime transport industry,” *Journal of Cleaner Production*, vol. 295, p. 126 428, 2021.

[20] D. Owen, Y. K. Demirel, E. Oguz, T. Tezdogan, and A. Incecik, “Investigating the effect of biofouling on propeller characteristics using cfd,” *Ocean Engineering*, vol. 159, pp. 505–516, 2018.

[21] Registro Italiano Navale. “Marpol.” (), [Online]. Available: https://www.rina.org/en/marpol (visited on 08/02/2024).

[22] International Maritime Organization. “International convention for the prevention of pollution from ships (marpol).” (), [Online]. Available: https://www.imo.org/en/about/Conventions/Pages/International-Convention-for-the-Prevention-of-Pollution-from-Ships-(MARPOL).aspx (visited on 08/02/2024).

[23] M. Candries, “Drag, boundary-layer and roughness characteristics of marine surfaces coated with antifoulings [phd thesis],” *Newcastle, UK: University of Newcastle-upon Tyne*, 2001.

[24] M. van Gils, “From disk to ship - drag characterization and prediction of full scale frictional resistance coefficient of arbitrarily rough surfaces on rotating disk,”

[25] H. Schlichting, *Experimental investigation of the problem of surface roughness*. National Advisory Commitee for Aeronautics, 1937.

[26] Cortana. “Description of drag.” ().

[27] D. Chung, N. Hutchins, M. P. Schultz, and K. A. Flack, “Predicting the drag of rough surfaces,” *Annual Review of Fluid Mechanics*, vol. 53, pp. 439–471, 2021.

[28] F. H. Clauser, “Turbulent boundary layers in adverse pressure gradients,” *Journal of the Aeronautical Sciences*, vol. 21, no. 2, pp. 91–108, 1954.

[29] M. Candries, M. Atlar, and C. Anderson, “Estimating the impact of new-generation antifoulings on ship performance: The presence of slime,” *Journal of Marine Engineering & Technology*, vol. 2, no. 1, pp. 13–22, 2003.

[30] MARIN, “Biofouling literature report,” 2023.

[31] M. P. Schultz, “Effects of coating roughness and biofouling on ship resistance and powering,” *Biofouling*, vol. 23, no. 5, pp. 331–341, 2007.

[32] O. Usta and E. Korkut, “A study for the effect of surface roughness on resistance characteristics of flat plates,” *Marine Coatings: London, UK*, 2013.

[33] R. Townsin, “The correlation of added drag with surface roughness parameters,” in *Recent Developments in Turbulence Management*, Springer, 1991, pp. 181–191.

[34] Y. K. Demirel, D. Uzun, Y. Zhang, H.-C. Fang, A. H. Day, and O. Turan, “Effect of barnacle fouling on ship resistance and powering,” *Biofouling*, vol. 33, no. 10, pp. 819–834, 2017.

[35] A. Lindholdt, K. Dam-Johansen, S. Olsen, D. M. Yebra, and S. Kiil, “Effects of biofouling development on drag forces of hull coatings for ocean-going ships: A review,” *Journal of Coatings Technology and Research*, vol. 12, pp. 415–444, 2015.

[36] M. Salta *et al.*, “Designing biomimetic antifouling surfaces,” *Philosophical Transactions of the Royal Society A: Mathematical, Physical and Engineering Sciences*, vol. 368, no. 1929, pp. 4729–4754, 2010.

[37] J. Holtrop, G. Mennen, *et al.*, “An approximate power prediction method,” *International Shipbuilding Progress*, vol. 29, no. 335, pp. 166–170, 1982.

[38] B. Bowden and N. Davison, *Resistance increments due to hull roughness associated with form factor extrapolation methods*. NPL, 1974.

[39] M. Schultz and G. Swain, “The effect of biofilms on turbulent boundary layers,” 1999.

[40] G. W. Swain, B. Kovach, A. Touzot, F. Casse, and C. J. Kavanagh, “Measuring the performance of today’s antifouling coatings,” *Journal of Ship Production*, vol. 23, no. 03, pp. 164–170, 2007.

[41] P. Darvehei, P. A. Bahri, and N. R. Moheimani, “Model development for the growth of microalgae: A review,” *Renewable and Sustainable Energy Reviews*, vol. 97, pp. 233–258, 2018.

[42] D. Uzun, Y. K. Demirel, A. Coraddu, and O. Turan, “Time-dependent biofouling growth model for predicting the effects of biofouling on ship resistance and powering,” *Ocean Engineering*, vol. 191, p. 106 432, 2019.

[43] P. K. Bijl, S. Schouten, A. Sluijs, G.-J. Reichart, J. C. Zachos, and H. Brinkhuis, “Early palaeogene temperature evolution of the southwest pacific ocean,” *Nature*, vol. 461, no. 7265, pp. 776–779, 2009.

[44] O. Bernard and B. Rémond, “Validation of a simple model accounting for light and temperature effect on microalgal growth,” *Bioresource technology*, vol. 123, pp. 520–527, 2012.

[45] J. H. Steele, “Environmental control of photosynthesis in the sea,” *Limnology and oceanography*, vol. 7, no. 2, pp. 137–150, 1962.

[46] M. Martinez, J. Jiménez, and F. El Yousfi, “Influence of phosphorus concentration and temperature on growth and phosphorus uptake by the microalga scenedesmus obliquus,” *Bioresource technology*, vol. 67, no. 3, pp. 233–240, 1999.

[47] S. Dobretsov, R. M. Abed, and C. R. Voolstra, “The effect of surface colour on the formation of marine micro and macrofouling communities,” *Biofouling*, vol. 29, no. 6, pp. 617–627, 2013.

[48] G. Swain, S. Herpe, E. Ralston, and M. Tribou, “Short-term testing of antifouling surfaces: The importance of colour,” *Biofouling*, vol. 22, no. 6, pp. 425–429, 2006.

[49] K. Abdel Salam and A. Abdel Halim, “Influence of colour of substratum on the marine fouling communities at the eastern harbour (alexandria, egypt),” *Egyptian Journal of Aquatic Research*, vol. 34, no. 1, pp. 126–143, 2008.

[50] D. Uzun, R. Ozyurt, Y. Demirel, and O. Turan, “Time based ship added resistance prediction model for biofouling,” in *Marine Design XIII, Volume 2*, CRC Press, 2018, pp. 971–979.

[51] F. L. dos Santos, L. Botero, C. Venner, and L. D. de Santana, “On the turbulence distortion effects for airfoil leading-edge noise prediction,” in *28th AIAA/CEAS aeroacoustics 2022 conference*, 2022, p. 3045.

[52] G. Dekkers, “Turbulence: Clarity amidst chaos,” 2023.

[53] Y. K. Demirel, O. Turan, and A. Incecik, “Predicting the effect of biofouling on ship resistance using cfd,” *Applied ocean research*, vol. 62, pp. 100–118, 2017.

[54] Y. K. Demirel, M. Khorasanchi, O. Turan, A. Incecik, and M. P. Schultz, “A cfd model for the frictional resistance prediction of antifouling coatings,” *Ocean Engineering*, vol. 89, pp. 21–31, 2014.

[55] C. Grigson, “Drag losses of new ships caused by hull finish,” *Journal of Ship Research*, vol. 36, no. 02, pp. 182–196, 1992.

[56] D. Apsley, “Cfd calculation of turbulent flow with arbitrary wall roughness,” *Flow, Turbulence and combustion*, vol. 78, pp. 153–175, 2007.

[57] S. Song, Y. K. Demirel, and M. Atlar, “An investigation into the effect of biofouling on the ship hydrodynamic characteristics using cfd,” *Ocean Engineering*, vol. 175, pp. 122–137, 2019.

[58] S. Song, Y. K. Demirel, and M. Atlar, “An investigation into the effect of biofouling on full-scale propeller performance using cfd,” in *International Conference on Offshore Mechanics and Arctic Engineering*, American Society of Mechanical Engineers, vol. 58776, 2019, V002T08A036.

[59] A. Farkas, N. Degiuli, and I. Martić, “An investigation into the effect of hard fouling on the ship resistance using cfd,” *Applied Ocean Research*, vol. 100, p. 102 205, 2020.

[60] A. Farkas, N. Degiuli, and I. Martić, “Towards the prediction of the effect of biofilm on the ship resistance using cfd,” *Ocean engineering*, vol. 167, pp. 169–186, 2018.

[61] Y. Zou, X. Zhou, L. Chen, and X. Xi, “Impacts of different characteristics of marine biofouling on ship resistance,” *Ocean Engineering*, vol. 278, p. 114 415, 2023.

[62] S. Sezen, D. Uzun, R. Ozyurt, O. Turan, and M. Atlar, “Effect of biofouling roughness on a marine propeller’s performance including cavitation and underwater radiated noise (urn),” *Applied Ocean Research*, vol. 107, p. 102 491, 2021.

[63] M. G. Ducamp, “Application of federated learning,” 2024.

[64] ERA5 hourly data on single levels from 1940 to present. “Copernicus.” (), [Online]. Available: https://cds.climate.copernicus.eu/cdsapp#!/home (visited on 01/07/2024).

[65] Copernicus Marine MyOcean Viewer. “Copernicus marine data store.” (), [Online]. Available: https://data.marine.copernicus.eu/viewer/.

[66] W. C. Forsythe, E. J. Rykiel Jr, R. S. Stahl, H.-i. Wu, and R. M. Schoolfield, “A model comparison for daylength as a function of latitude and day of year,” *Ecological Modelling*, vol. 80, no. 1, pp. 87–95, 1995.

[67] Visual Crossing. “Weather data & api.” (), [Online]. Available: https://www.visualcrossing.com (visited on 05/15/2024).

[68] J. Kirk, “Attenuation of light in natural waters,” *Marine and Freshwater Research*, vol. 28, no. 4, pp. 497–508, 1977.

[69] S. Manakov, “Nonlinear fraunhofer diffraction,” *Zh. Eksp. Teor. Fiz*, vol. 65, no. 4, p. 10, 1973.

[70] S. A. Fatemi and A. Kuh, “Solar radiation forecasting using zenith angle,” in *2013 IEEE Global Conference on Signal and Information Processing*, IEEE, 2013, pp. 523–526.

[71] M. P. Schultz, “Frictional resistance of antifouling coating systems,” *J. Fluids Eng.*, vol. 126, no. 6, pp. 1039–1047, 2004.

[72] MARIN. “Versatile solver, tailored for maritime challenges.” (), [Online]. Available: https://www.marin.nl/en/about/facilities-and-tools/software/refresco.

[73] S. Patankar, *Numerical heat transfer and fluid flow*. CRC press, 2018.

[74] T. Miller and F. Schmidt, “Use of a pressure-weighted interpolation method for the solution of the incompressible navier-stokes equations on a nonstaggered grid system,” *Numerical Heat Transfer, Part A: Applications*, vol. 14, no. 2, pp. 213–233, 1988.

[75] Ulisboa. “Flow over a flat plate.” (), [Online]. Available: https://web.tecnico.ulisboa.pt/ist12278/Workshop_AVT_313_2D_cases/html_files/Flat_Plate.htm (visited on 08/03/2024).

[76] Cadence. “Fidelity hexpress.” (), [Online]. Available: https://community.cadence.com/cadence_technology_forums/computational-fluid-dynamics/f/automesh/58122/structured-vs-unstructured-mesh.

[77] F. R. Menter, M. Kuntz, R. Langtry, *et al.*, “Ten years of industrial experience with the sst turbulence model,” *Turbulence, heat and mass transfer*, vol. 4, no. 1, pp. 625–632, 2003.

[78] E. Pozzi, “The mystery of the green passenger,” 2024.

[79] L. Eça, A. Starke, M. Kerkvliet, and H. Raven, “On the contribution of roughness effects to the scaling of ship resistance,” *Journal of Ocean Engineering and Marine Energy*, vol. 8, no. 4, pp. 539–551, 2022.

A

Enriched Data Plots

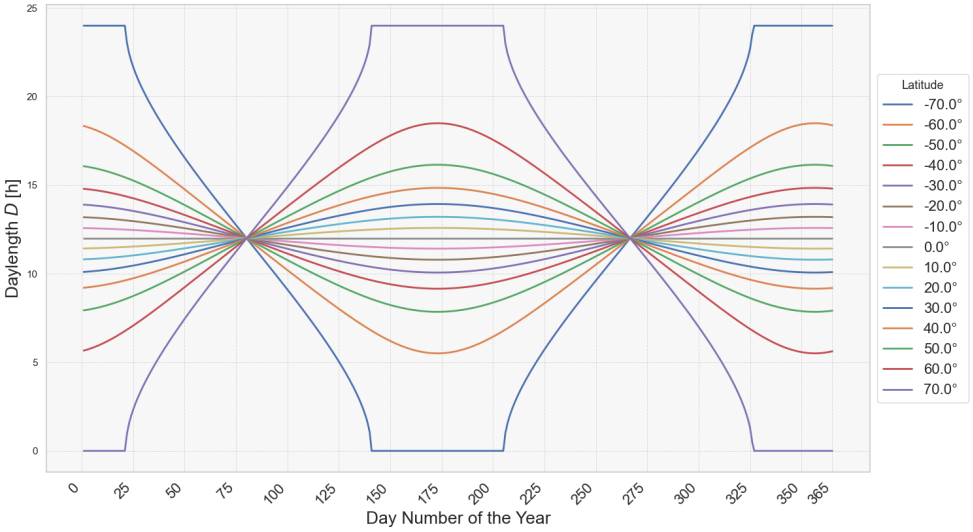

Figure A.1: Daylength per latitude, according to Forsythe [66]

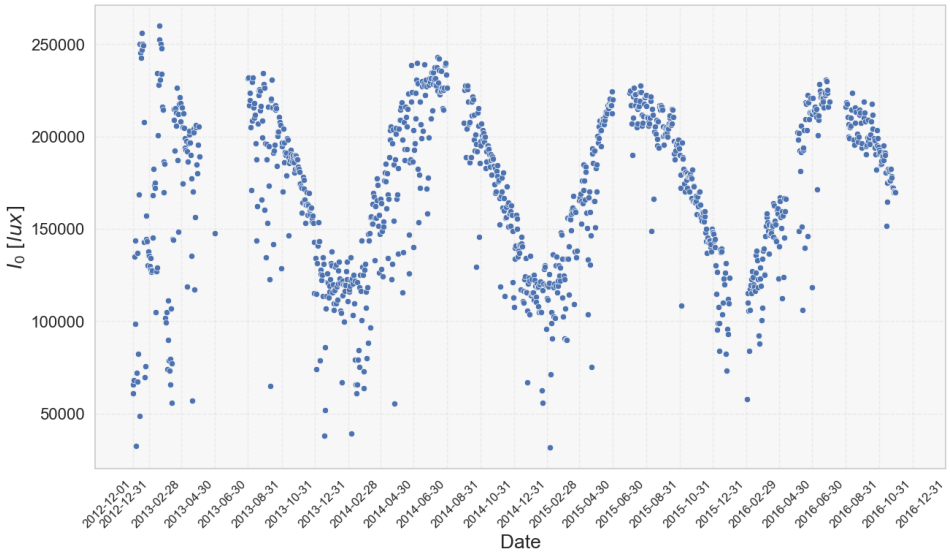

Figure A.2: Light intensity I_0 from History Forecast Data [67] archives

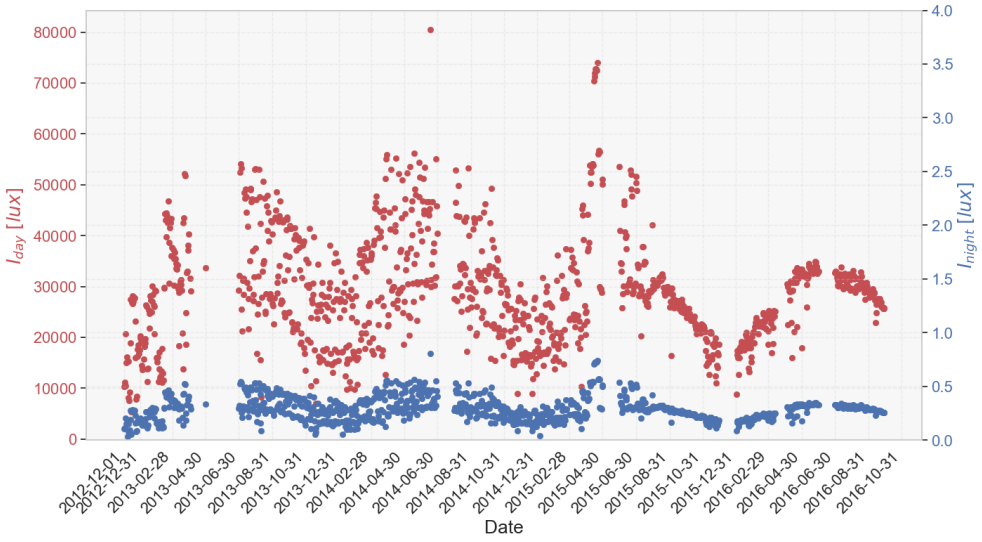

Figure A.3: Day and night light intensities time evolution

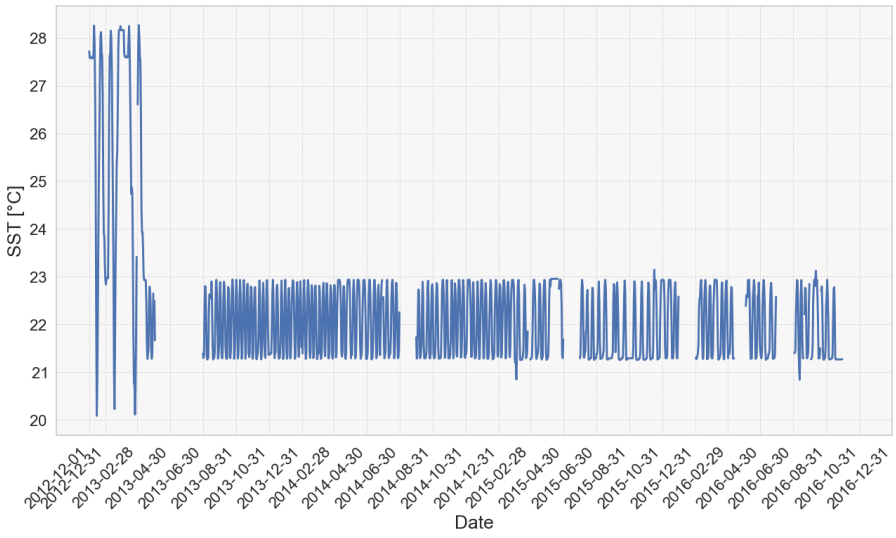

Figure A.4: Sea Surface Temperature time evolution at ship's latitude

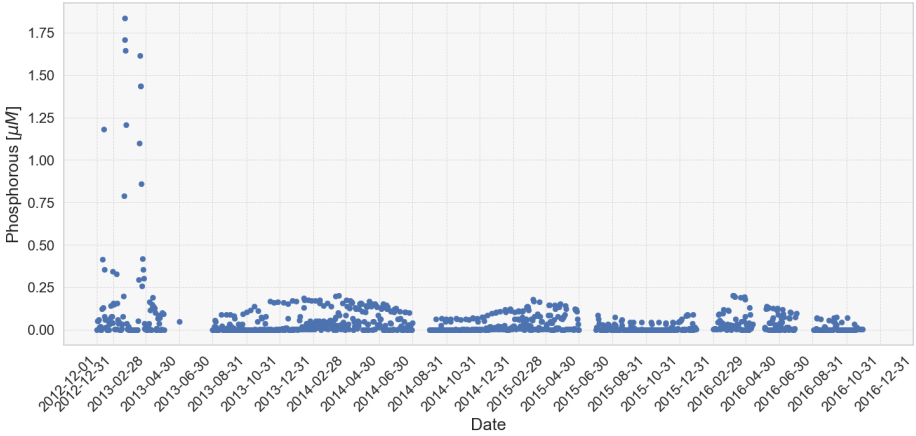

Figure A.5: Phosphorous concentration in seawater at ship's location

B

Surface Colour Plots

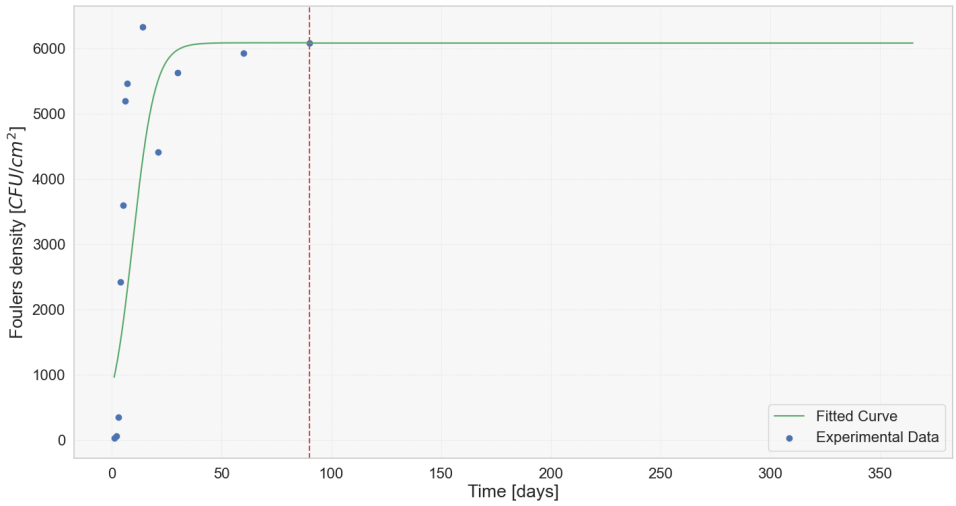

Figure B.1: Fouling density for red surface

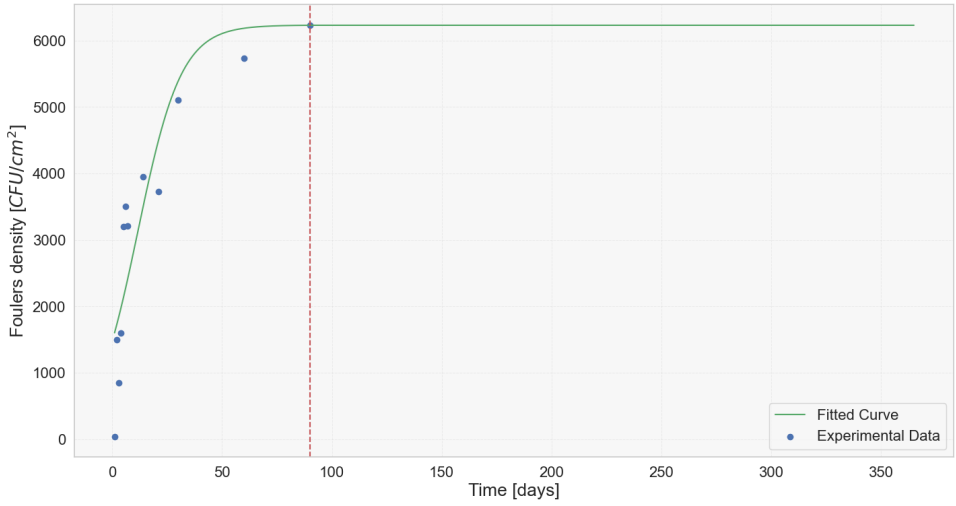

Figure B.2: Fouling density for yellow surface

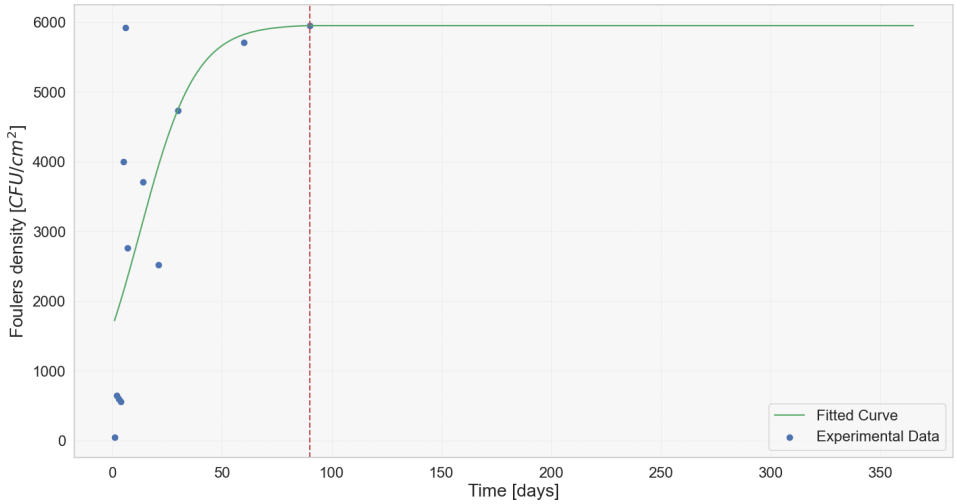

Figure B.3: Fouling density for light-blue surface

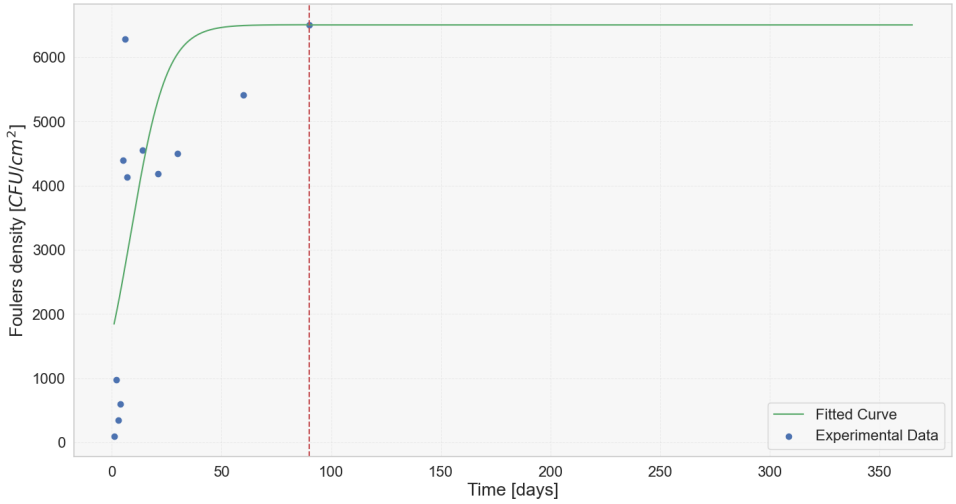

Figure B.4: Fouling density for dark-green surface

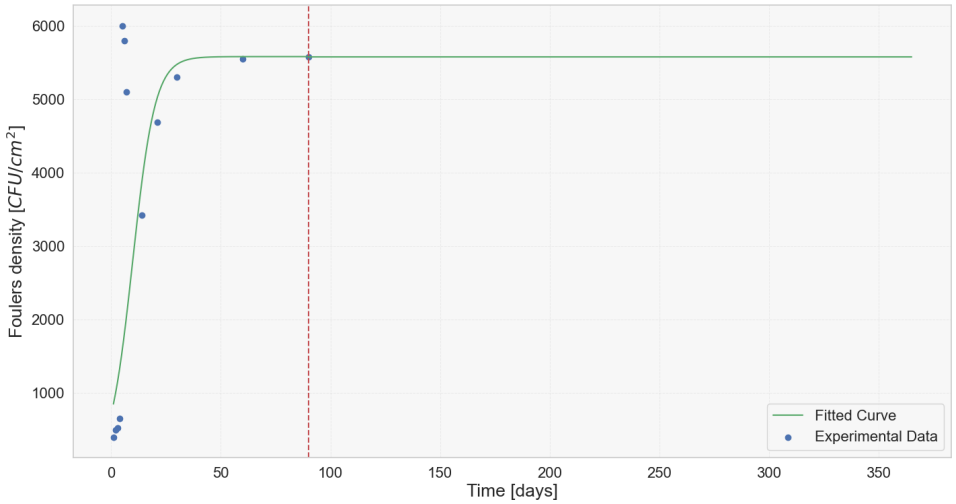

Figure B.5: Fouling density for black surface

C

Holtrop & Mennen Method [37]

The method is based on the regression analysis of displacement type model tests and trial data. To it be considered applicable, the containership in object needs to respect the following conditions:

- the cross sectional area of the bulb must be less than 20% of the midship area A_x;
- $3.5 \leq L_{wl}/B \leq 9.5$;
- the longitudinal position of the centre of buoyancy LCB, forward of $L/2$ and as a percentage of L, should be included in the range ± 5%;
- prismatic coefficient $0.4 \leq C_P \leq 0.93$, and midship coefficient $0.5 \leq C_X \leq 1.0$;
- the half angle of waterline entrance at the bow i_E is maximum $70°$;

The formulas presented in this appendix serve as a comprehensive reference for the method's framework. Each equation of the methodology is derived from experimental data, and validated through practical applications. Unlike what explained in Section 3.2, the original formulation considers the dimensional resistance components (instead of Newton numbers), and the model-ship correlation resistance. Equation C.1 shows the complete total resistance R_T and its main components, as proposed by the authors. Both the appendix and model-ship correlation resistance, respectively R_{APP} and R_A, will not be included in the dissertation.

$$R_T = R_F(1 + k_1) + R_{APP} + R_W + R_B + R_{TR} + R_A \tag{C.1}$$

Frictional and form

The ITTC-57 friction formula in Equation C.2 is used for C_F, while the form factor k_1 describing the viscous resistance of the hull form is obtained by Equation C.3.

$$C_F = \frac{0.0075}{(log(Re) - 2)^2} \tag{C.2}$$

$$k_1 = 0.93 + 0.487118 \left(\frac{B}{L_{wl}}\right)^{1.06806} \left(\frac{T}{L_{wl}}\right)^{0.46106} \left(\frac{L_{wl}}{L_R}\right)^{0.121563} \left(\frac{L_{wl}^3}{\nabla}\right)^{0.36486} (1 - C_P)^{-0.604247} \tag{C.3}$$

where L_R is a constant, dependent on the prismatic coefficient C_P and LCB.

$$L_R = L_{wl}\left(1 - C_P + \frac{0.06 C_P\ LCB}{4C_P - 1}\right) \tag{C.4}$$

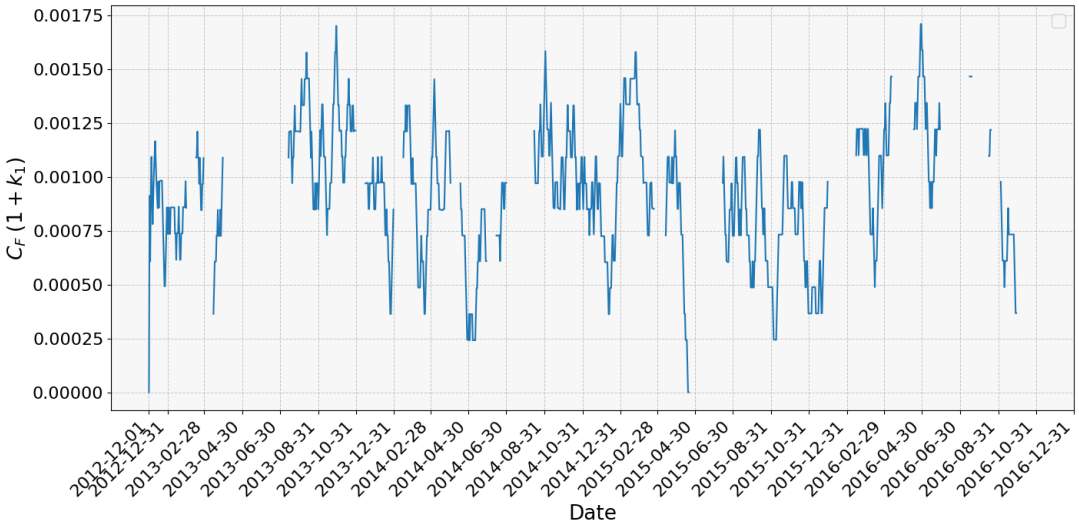

Figure C.1: Frictional and form resistance $C_F(1+k_1)$ for moving average (15 points)

Bulb & Transom

Given the transverse bulb area A_{BT} and its corresponding vertical position of centre of gravity at a forward draft T_F, the additional resistance due to bulbous bow R_B near the surface is determined through Equation C.5. This can then be made non-dimensional in C_{bulb}.

$$R_B = \frac{0.11 e^{-3P_B^{-2}} F_{ni}^3 A_{BT}^{1.5} \rho_w g}{1 + F_{ni}^2} \qquad C_{bulb} = \frac{R_B}{\frac{1}{2}\rho_w S_w V^2} \tag{C.5}$$

P_B is a measure of the emergence of the bow (Equation C.6), and F_{ni} is the Froude number based on the immersion (Equation C.7).

$$P_B = 0.56 \frac{\sqrt{A_{BT}}}{T_F - 1.5 h_B} \tag{C.6}$$

$$F_{ni} = \frac{V}{\sqrt{g(T_F - h_B - 0.25\sqrt{A_{BT}}) + 0.15V^2}} \tag{C.7}$$

Similarly, the additional pressure resistance due to immersed transom can be calculated as in Equation C.8. This implies that the non-dimensional coefficient $C_{transom} \equiv c_6$ in Equation C.9, indirectly dependent on the waterplane coefficient C_{WP} through F_{nT}.

$$R_{TR} = \frac{1}{2}\rho_w \, V^2 \, A_{TR} \, c_6 \tag{C.8}$$

$$c_6 = \begin{cases} 0.2(1 - 0.2F_{nT}) & F_{nT} < 5 \\ 0 & F_{nT} \geq 5 \end{cases} \qquad F_{nT} = \frac{V}{\sqrt{\frac{2g \, A_{TR}}{B + B \, C_{WP}}}} \tag{C.9}$$

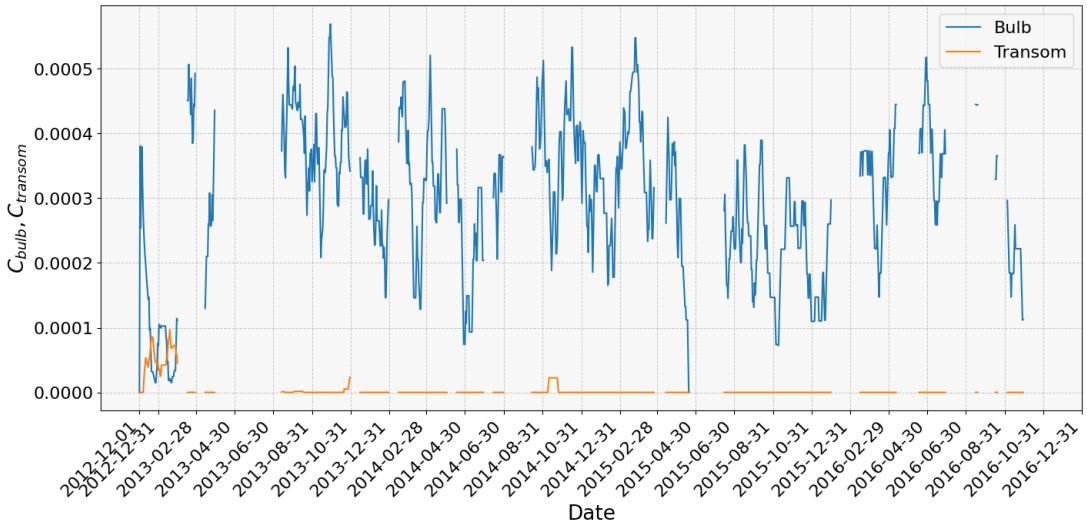

Figure C.2: Bulb and transom non-dimensional resistance coefficient moving average (8 points)

Wave-making and wave-breaking

The wave resistance R_W in Equation C.10 consists of multiple contributes. For example, it takes into account the resistance reduction due to the bulbous bow c_2 (through c_3 in Equation C.12), or the influence of the transom with c_5 in Equation C.11.

$$R_W = c_1 c_2 c_5 \nabla \rho_w g e^{m_1 Fr^{-0.9} + m_4 cos(\lambda Fr^{-2})} \qquad C_W = \frac{R_W}{\frac{1}{2}\rho_w V^2 S_w} \tag{C.10}$$

$$c_2 = e^{-1.89\sqrt{c_3}} \qquad c_5 = 1 - \frac{0.8 A_{TR}}{B\ T\ C_X} \tag{C.11}$$

$$c_3 = 0.56 \frac{A_{TR}^{1.5}}{B\ T(0.31\sqrt{A_{TR}} + T_F - h_B)} \tag{C.12}$$

The coefficient c_1 considers the half angle of entrance i_E expressed in Equation C.14, and c_7, dependent on the value of the ratio between breadth and waterline length (Equation C.15).

$$c_1 = 2223105 c_7^{3.78613} \left(\frac{T}{B}\right)^{1.07961} (90 - i_E)^{-1.37565} \tag{C.13}$$

$$i_E = 1 + 89 e^{-\left(\frac{L_{wl}}{B}\right)^{0.80856} (1 - C_{WP})^{0.30484} (1 - C_P - 0.0225 LCB)^{0.6367} \left(\frac{L_R}{B}\right)^{0.34574} \left(\frac{100\nabla}{L_{wl}^3}\right)^{0.16302}} \tag{C.14}$$

$$c_7 = \begin{cases} 0.229577 \left(\frac{B}{L_{wl}}\right)^{0.33333} & \frac{B}{L_{wl}} \leq 0.11 \\ \frac{B}{L_{wl}} & 0.11 < \frac{B}{L_{wl}} \leq 0.25 \\ 0.5 - 0.0625 \frac{L_{wl}}{B} & \frac{B}{L_{wl}} > 0.25 \end{cases} \tag{C.15}$$

$$\lambda = \begin{cases} 1.446C_P - 0.03\frac{L_{wl}}{B} & \frac{Lwl}{B} < 12 \\ 1.446C_P - 0.36 & \frac{L_{wl}}{B} \geq 12 \end{cases} \tag{C.16}$$

The weight factors m_1 and m_4, respectively in Equation C.17 and C.18, have a dependency on the ratio between waterline length and wetted volume ∇, and on the prismatic coefficient C_P through the constants appearing inside their formulation.

$$m_1 = 0.0140407\frac{L_{wl}}{T} - 1.75254\frac{\nabla^{1/3}}{L_{wl}} - 4.79323\frac{B}{L_{wl}} - c_{16} \tag{C.17}$$

$$m_4 = 0.4c_{15}e^{-0.034\ Fr^{-3.29}} \tag{C.18}$$

$$c_{15} = \begin{cases} -1.69385 & \frac{L_{wl}}{\nabla} < 512 \\ -1.69385 + \frac{L_{wl}^3/\nabla - 8}{2.36} & 512 \leq \frac{L_{wl}}{\nabla} \leq 1727 \\ 0 & \frac{L_{wl}}{\nabla} > 1727 \end{cases} \tag{C.19}$$

$$c_{16} = \begin{cases} 8.07981C_P - 13.8673C_P^2 + 6.984388C_P^3 & C_P \leq 0.8 \\ 1.73014 - 0.7067C_P & C_P > 0.8 \end{cases} \tag{C.20}$$

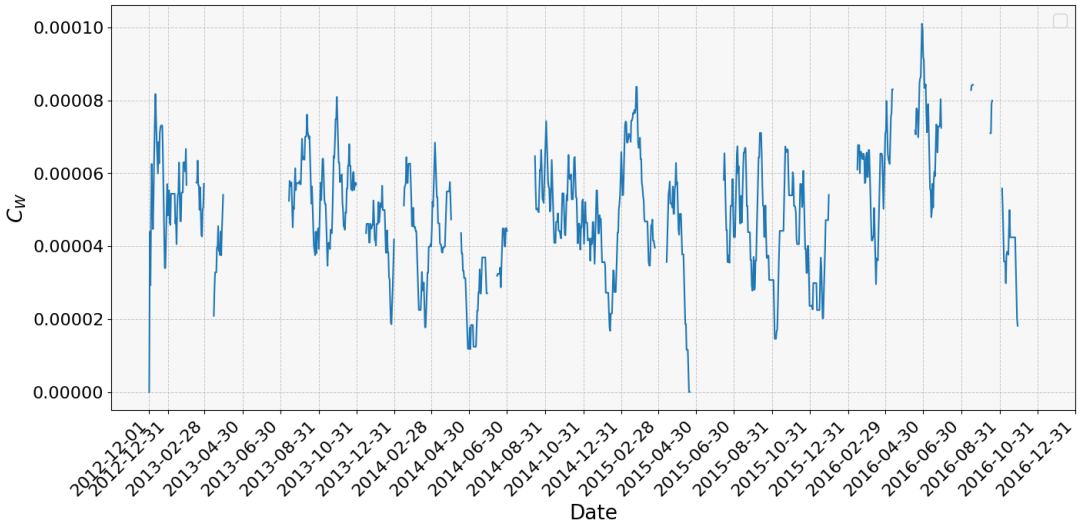

Figure C.3: Wave-making resistance C_W for moving average (15 points) for containership

D

Complementary Numerical Results

D.1. Transom condition

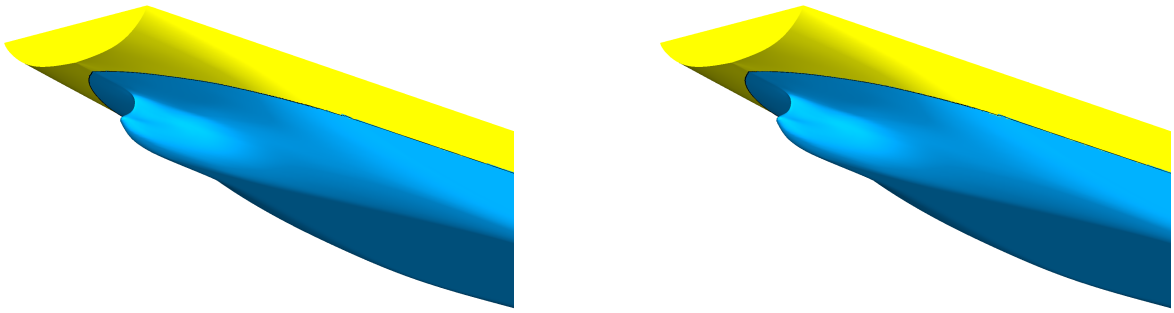

(a) (b)

Figure D.1: Transom condition check at $7\ kn$ for (a) smooth and (b) fouled $k_s = 300\ \mu m$

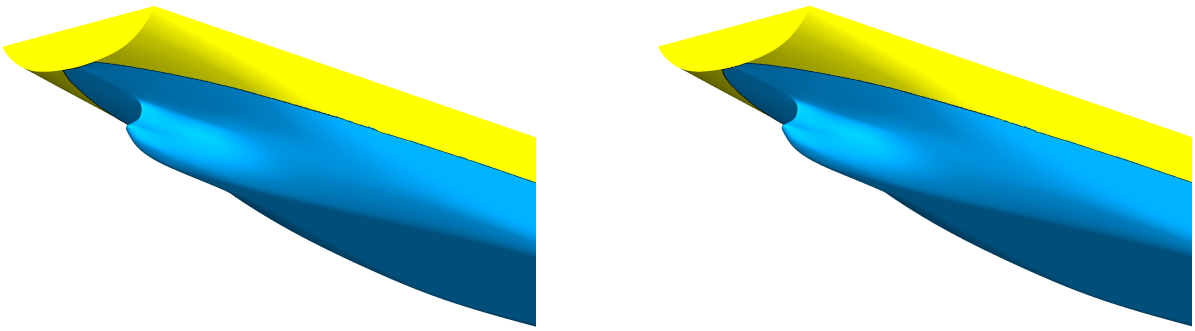

(a) (b)

Figure D.2: Transom condition check at $14\ kn$ for (a) smooth and (b) fouled $k_s = 300\ \mu m$

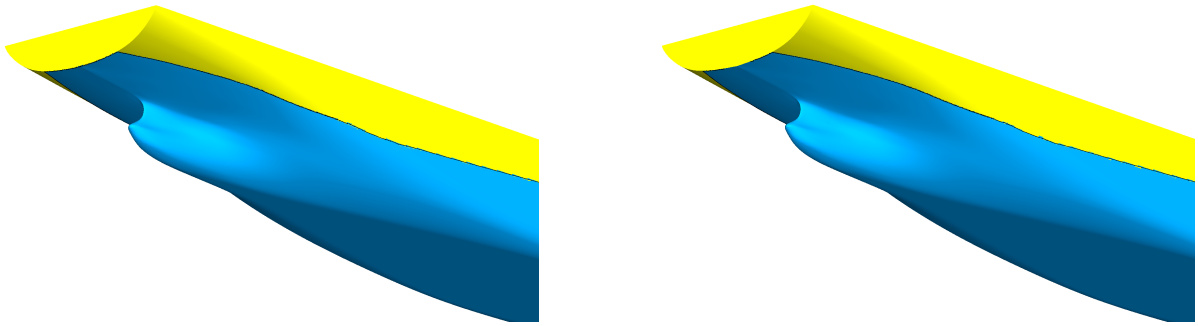

(a) (b)

Figure D.3: Transom condition check at $20.5\ kn$ for (a) smooth and (b) fouled $k_s = 300\ \mu m$

Table D.1: Transom contribution on total resistance

Speed	$\%C_R,\ k = 0$	$\%C_R,\ k = 300\ \mu m$	$\%C_F,\ k = 0$	$\%C_F,\ k = 300\ \mu m$
$V = 7\ kn$	1.20	0.10	0	0
$V = 14\ kn$	0.40	0.20	0	0
$V = 20.5\ kn$	1.00	0.90	0	0

D.2. Flow regime on the hull

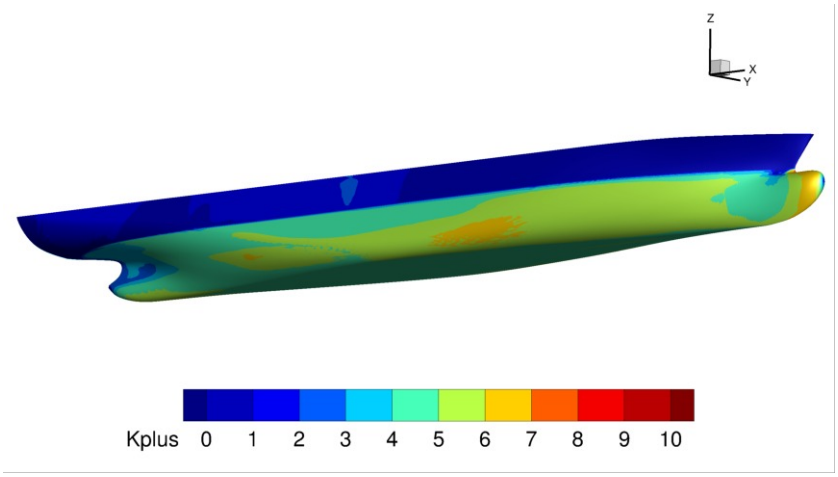

Figure D.4: k^+ distribution on the hull for $k_s = 50\ \mu m$ at $V = 7\ kn$

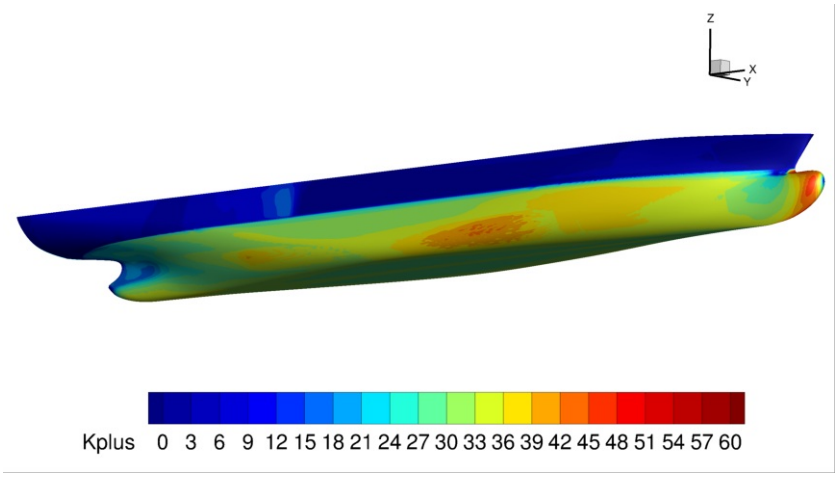

Figure D.5: k^+ distribution on the hull for $k_s = 300\ \mu m$ at $V = 7\ kn$

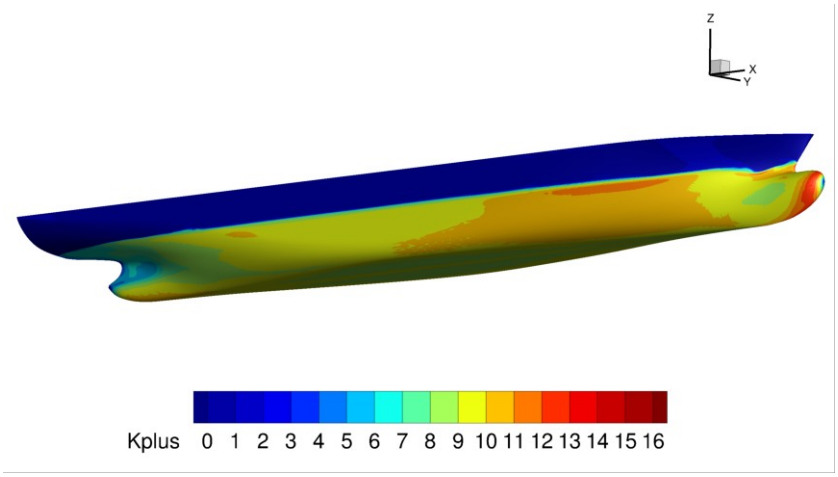

Figure D.6: k^+ distribution on the hull for $k_s = 50\ \mu m$ at $V = 14\ kn$

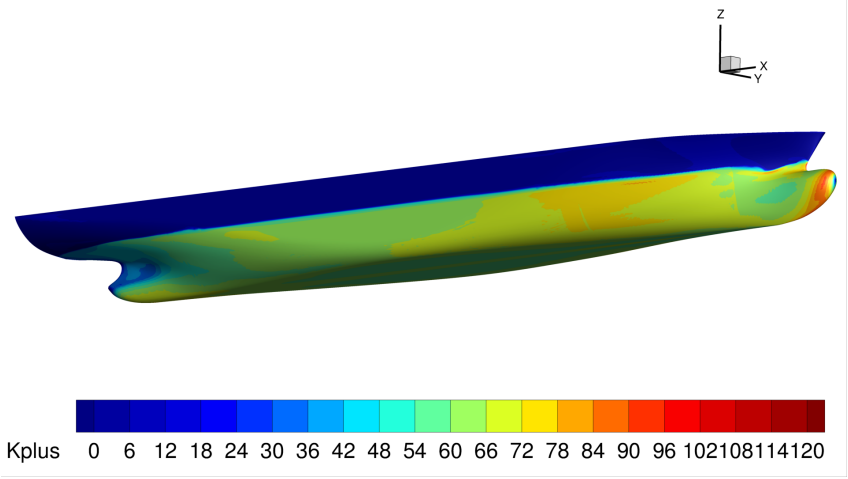

Figure D.7: k^+ distribution on the hull for $k_s = 300\ \mu m$ at $V = 14\ kn$

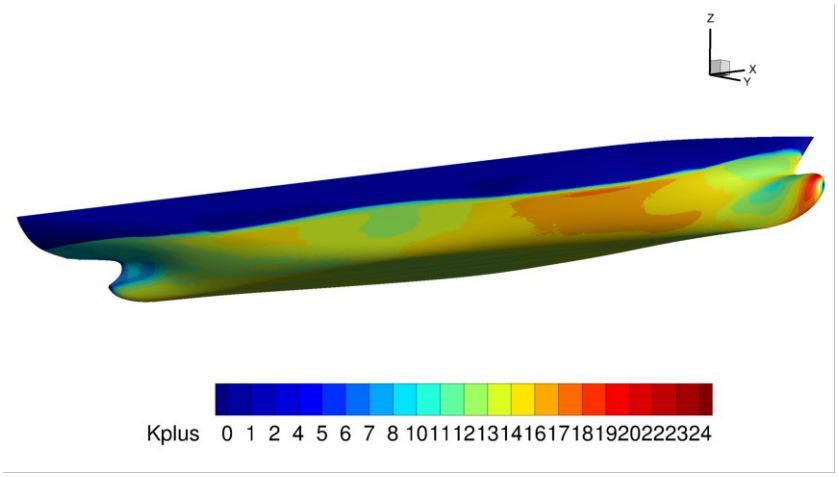

Figure D.8: k^+ distribution on the hull for $k_s = 50\ \mu m$ at $V = 20.5\ kn$

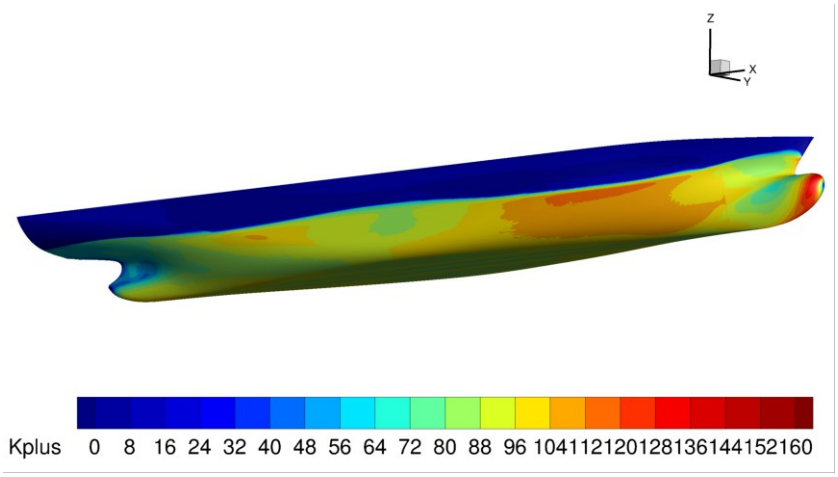

Figure D.9: k^+ distribution on the hull for $k_s = 300\ \mu m$ at $V = 20.5\ kn$

D.3. Frictional resistance $7\ kn$ and $20.5\ kn$

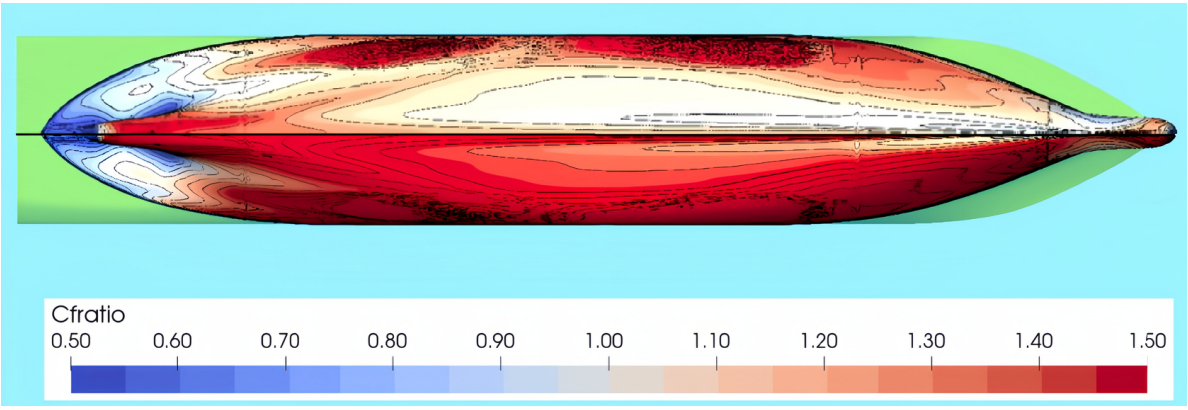

Figure D.10: $C_{f,ratio}$ comparison for smooth and rough $k_s = 300\ \mu m$ surface for $V = 7\ kn$ (bottom view)

Table D.2: Containership frictional resistance and percentage increase to smooth condition for $7\ kn$

$k_s\ [\mu m]$	C_F	$\%\Delta C_F/C_{F,S}$
0	$1.831 \cdot 10^{-3}$	–
50	$2.185 \cdot 10^{-3}$	11.9
100	$2.172 \cdot 10^{-3}$	18.6
150	$2.264 \cdot 10^{-3}$	23.7
200	$2.339 \cdot 10^{-3}$	27.8
250	$2.403 \cdot 10^{-3}$	31.2
300	$2.458 \cdot 10^{-3}$	34.3

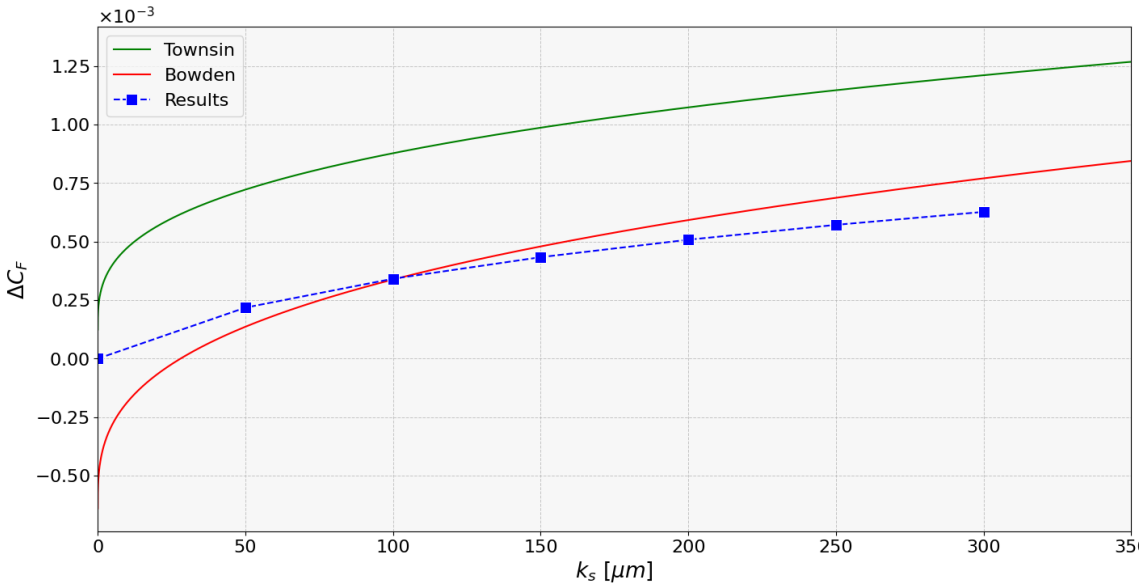

Figure D.11: Added frictional resistance for $V = 7\ kn$

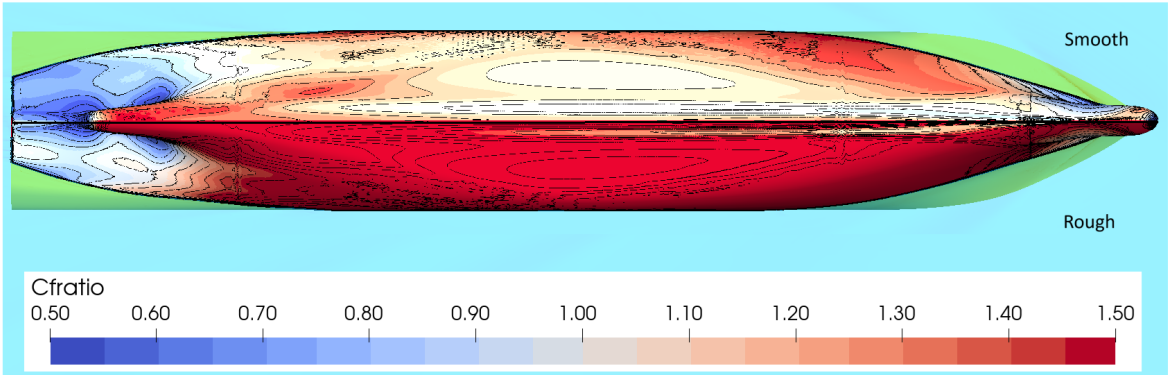

Figure D.12: $C_{f,ratio}$ comparison for smooth and rough $k_s = 300\ \mu m$ surface for $V = 20.5\ kn$ (bottom view)

Table D.3: Containership frictional resistance and percentage increase to smooth condition for $20.5\ kn$

$k_s\ [\mu m]$	C_F	$\%\Delta C_F/C_{F,S}$
0	$1.474 \cdot 10^{-3}$	–
50	$1.796 \cdot 10^{-3}$	21.8
100	$1.942 \cdot 10^{-3}$	31.7
150	$2.043 \cdot 10^{-3}$	38.6
200	$2.122 \cdot 10^{-3}$	43.9
250	$2.186 \cdot 10^{-3}$	48.3
300	$2.241 \cdot 10^{-3}$	52.0

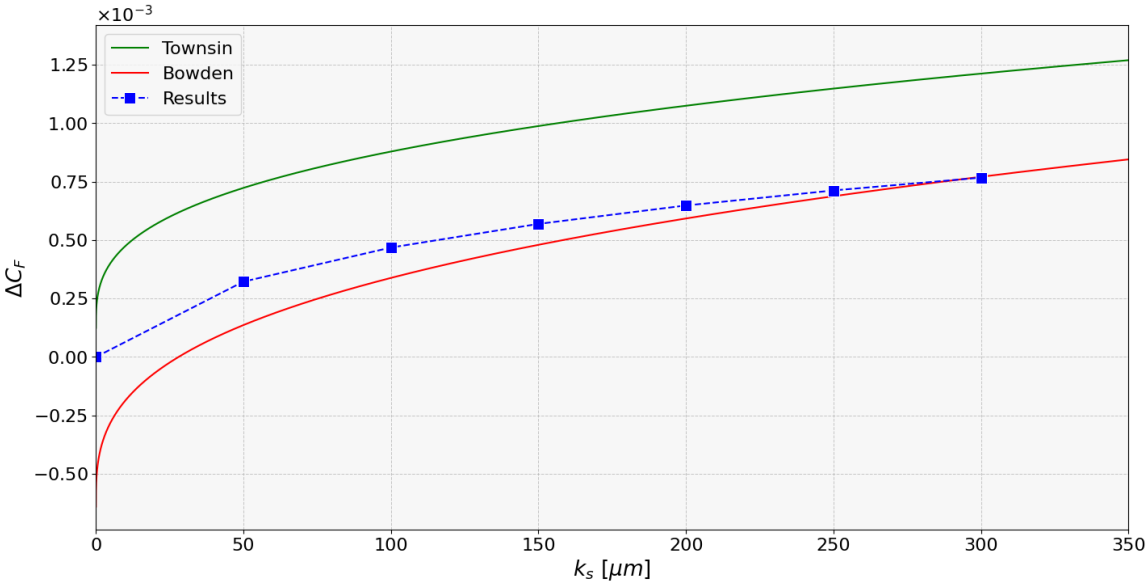

Figure D.13: Added frictional resistance for $V = 20.5\ kn$

D.4. Residuary resistance $V = 7\ kn$ and $V = 20.5\ kn$

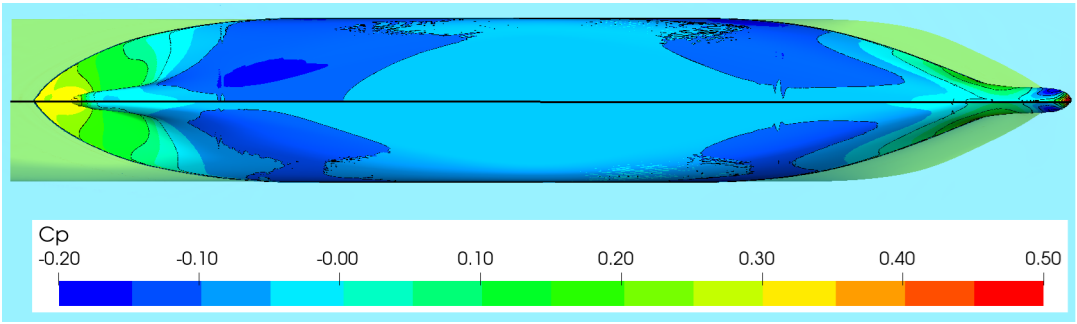

Figure D.14: C_p comparison at $7\ kn$ between $k_s = 300\ \mu m$ and $k_s = 0$ (bottom view)

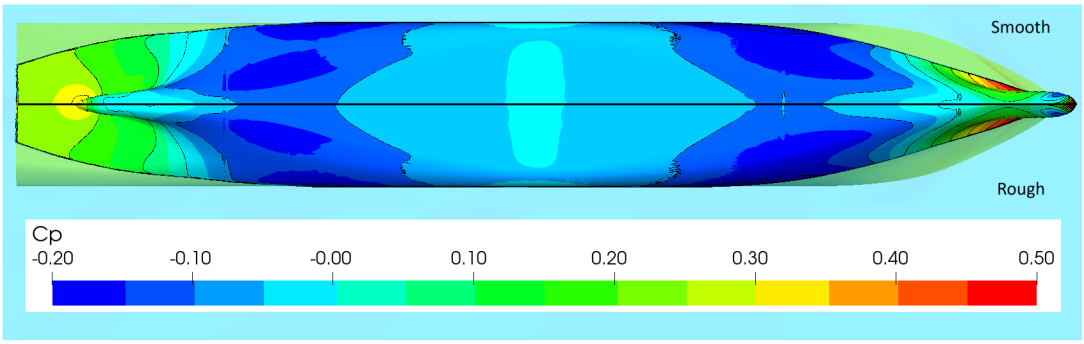

Figure D.15: C_p comparison at $20.5\ kn$ between $k_s = 300\ \mu m$ and $k_s = 0$ (bottom view)

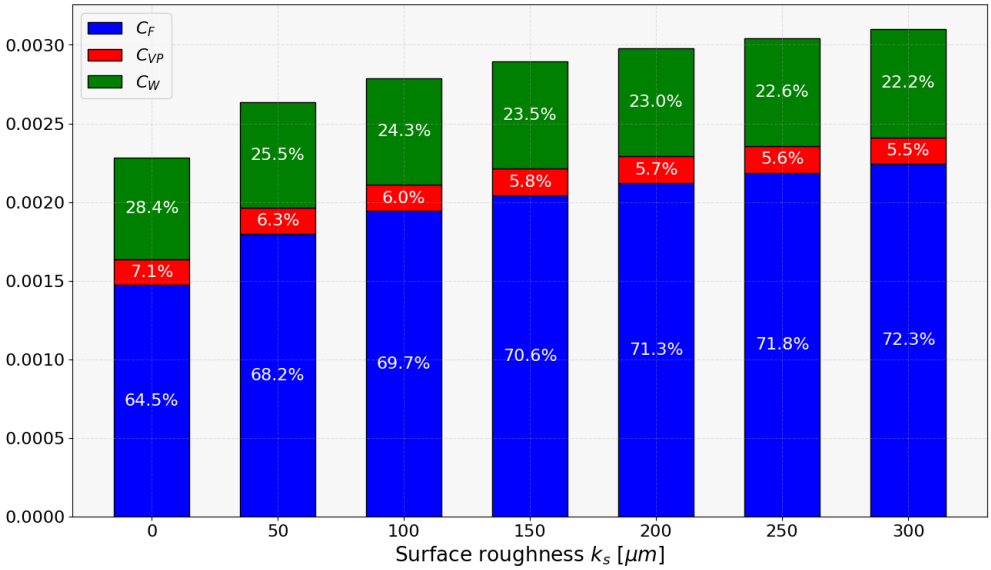

Figure D.16: Percentage bar diagram of the resistance components at $20.5\ kn$